Study on Supercritical Fluids in an Intermediate Heat Exchanger for an SCWR Hydrogen Cogeneration System

By

Juan Carlos Jouvin

A Thesis Submitted in Partial Fulfillment of the

Requirements for the Degree of

Master of Applied Science

In

Nuclear Engineering

The Faculty of Energy Systems and Nuclear Science

University of Ontario Institute of Technology

December, 2015

Abstract

SuperCritical Water-cooled Reactors (SCWRs) are one of six Generation-IV nuclear reactor concepts under development worldwide. SCWRs benefit from an increase in thermal efficiency due to the reactor coolant operating above the critical point of water. They are currently being designed to work at pressures of 25 MPa with outlet temperatures up to 625°C. These operating conditions make them a suitable candidate for thermochemical hydrogen cogeneration.

This work investigates the use of SCWR process heat for the thermochemical production of hydrogen. A thermochemical cycle currently being studied for this purpose is the 4-step Copper-Chlorine (Cu-Cl) cycle. This is due to its relatively low temperature requirements when compared to other existing thermochemical cycles. To achieve this, an intermediate Heat eXchanger (HX) linking a SuperCritical Water (SCW) Nuclear Power Plant (NPP) and a hydrogen production facility is considered. The objective of this work is to assess the performance of supercritical fluids in an intermediate HX to be used for the cogeneration of hydrogen.

The thermal energy requirement for the 4-step Cu-Cl cycle is identified and a numerical model is developed in MATLAB. Reference cases for an SCW-to-SCW HX and an SCW-to-supercritical CO_2 HX are developed. A heat transfer analysis is conducted on each of these reference cases as well as on subsequent test cases. In these test cases, various sensitivity analyses are performed to determine the effect that mass flux, pressure and piping dimensions will have on the overall system. Ultimately, this will give an indication as to what combination of parameters should be used to optimize the design of the HX in terms of overall heat transfer surface area.

Acknowledgements

I am sincerely grateful to my supervisor, Dr. Igor Pioro, for all of his support and encouragement throughout the completion of this thesis. I am sincerely grateful for all of the wisdom he bestowed upon me. I would like to thank him for his patience and guidance during my research.

I would like to thank my colleagues Amjad Farah, Jeffrey Samuel, Adam Lipchitz, Eugene Saltanov, Kelvin Seto and Khalil Sidawi for their valuable insights and discussions. I am especially thankful to Amjad Farah and Jeffrey Samuel. I have genuinely appreciated their advice and their friendship. Their knowledgeable input was immensely valuable to my research and to writing of this thesis.

I am thankful to my friends Vatsal Trivedi, Russell Wilson, Ryan Parcels and Enzo Carletti for their camaraderie and support. I am thankful to my family, especially my parents, Juan Carlos and Aida Jouvin, as well as my grandmother Juana Aspiazu for their amazing emotional and material support.

Finally, I would like to thank my fiancé, Joanne Casarella for her unwavering support and for her optimism during times of adversity. I am eternally grateful for her endless encouragement throughout my entire academic career.

Table of Contents

List of Tables

List of Figures

Nomenclature

A_c	Cross-sectional area, m^2
A_s	Surface area, m^2
C	Heat capacity rate, W/K
C_p	Specific heat (by property tables), $J/kg \cdot K$
$\overline{C_p}$	Average specific heat $\left(\text{by } \frac{H_w - H_b}{T_w - T_b}\right)$, $J/kg \cdot K$
D, d	Diameter, m
G	Mass flux, $kg/m^2 \cdot s$
H	Specific Enthalpy, J/kg
HTC	Heat transfer coefficient, $W/m^2 \cdot K$
k	Thermal conductivity, $W/m \cdot K$
$\dot{m}$	Mass flowrate, kg/s
P	Pressure, Pa
P_{th}	Thermal power, W
p	Perimeter, m
$\dot{Q}$	Heat transfer rate, W
R	Thermal resistance, $K \cdot m^2/W$
S	Tensile Strength, MPa
T	Temperature, °C
U	Overall heat transfer coefficient, $W/m^2 \cdot K$

Greek Letters

Δ	Difference
μ	Dynamic viscosity, $Pa \cdot s$
ρ	Density, kg/m^3
δ	Wall thickness, m

Dimensionless numbers

Nu	Nusselt number $\left(\frac{HTC \cdot D_{hy}}{k}\right)$
Pr	Prandtl number $\left(\frac{\mu \cdot C_p}{k}\right)$
$\overline{\mathbf{Pr}}$	Average Prandtl number $\left(\frac{\mu \cdot \overline{C_p}}{k}\right)$
Re	Reynolds number $\left(\frac{G \cdot D_{hy}}{\mu}\right)$

Subscripts

avg	average
aq	aqueous
b	bulk
cr	critical
cs	cold side
el	electric
g	gas
hs	hot side
hy	hydraulic equivalent
in	inlet
i	inner
l	liquid
lm	log mean
m	medium
out	outlet
o	outer
pc	pseudocritical
s	solid
su	surface
th	thermal

Acronyms

ASME	American Society of Mechanical Engineers
BWR	Boiling Water Reactor
Cu-Cl	Copper-Chlorine
ELSY	European Lead-cooled SYstem
GFR	Gas-cooled Fast Reactor
GIF	Generation-IV International Forum
HP	High pressure
HX	Heat eXchanger
IAEA	International Atomic Energy Agency
IP	Intermediate Pressure
LFR	Lead-cooled Fast Reactor
LMTD	Log Mean Temperature Difference
MSR	Molten Salt Reactor
NIST	National Institute of Standards and Technology

NPP	Nuclear Power Plant
PT	Pressure Tube
PV	Pressure Vessel
PWR	Pressurized Water Reactor
REFPROP	REFerence fluid thermodynamic and transport PROPerties
SCW	Super Critical Water
SCWR	SuperCritical Water-cooled Reactor
SS	Stainless Steel
SI	Sulfure-Iodine
SFR	Sodium-cooled Fast Reactor
SSTAR	Small Secure Transportable Autonomous Reactor
UTS	Ultimate Tensile Strength
VHTR	Very-High-Temperature Reactor

Chapter 1. Introduction

The demand for energy and electricity continues to grow. As per the Organisation for Economic Co-operation and Development's (OECD's) International Energy Agency (IEA), the total world primary energy demand grew by 26% from 2000 to 2010. Growth to 2035 is expected to be 45% under current policies and 33% with more stringent policies in place. The demand for electricity has also experienced a dramatic increase with the demand doubling between 1990 and 2011; this demand is projected to grow by 81% between 2011 and 2035, that is, from 19,004 TWh to 34,454 TWh [1]. It is also predicted that the world population will increase from 6.7 billion in 2011 to 8.7 billion in 2035 [2]. As a result, it is imperative that new solutions are developed in order to alleviate the world's energy crisis.

Currently, nuclear power is an established contributor to the world's electricity mix supplying 11% of the world electricity of 22,752 TWh in 2012. Other contributors included resources such as coal, natural gas, and hydro, with coal providing almost 50% of the world's electricity. Figure 1-1 presents a breakdown of the electricity mix [2]. Figure 1-1 shows that coal and natural gas combine for approximately 62% of the world's electricity. Coal is still very abundant and is typically located near where it may be used, however, one of its major drawbacks is that it is the greatest contributor to greenhouse gases of any fossil fuel. Unlike coal, natural gas reserves are located in geopolitically uncertain areas, where transport becomes a major concern; it should also be noted that moving it as liquefied natural gas consumes up to 30% of it [1]. Renewable energy sources also have significant drawbacks with one of more the pressing issues being that they alone cannot meet the demand. Apart from hydro, the cost and intermittent nature of renewables limit their potential. This makes it difficult to consider renewables as the sole source of continuous base-load

power. It is for this reason that there is a need for cleaner alternatives that can meet the ever-growing energy demand.

Nuclear power is suitable for large-scale, continuous electricity demand due to its reliability, as such it could continue to play a pivotal role in providing base-load electricity in the future, especially with the move towards cleaner energy sources.

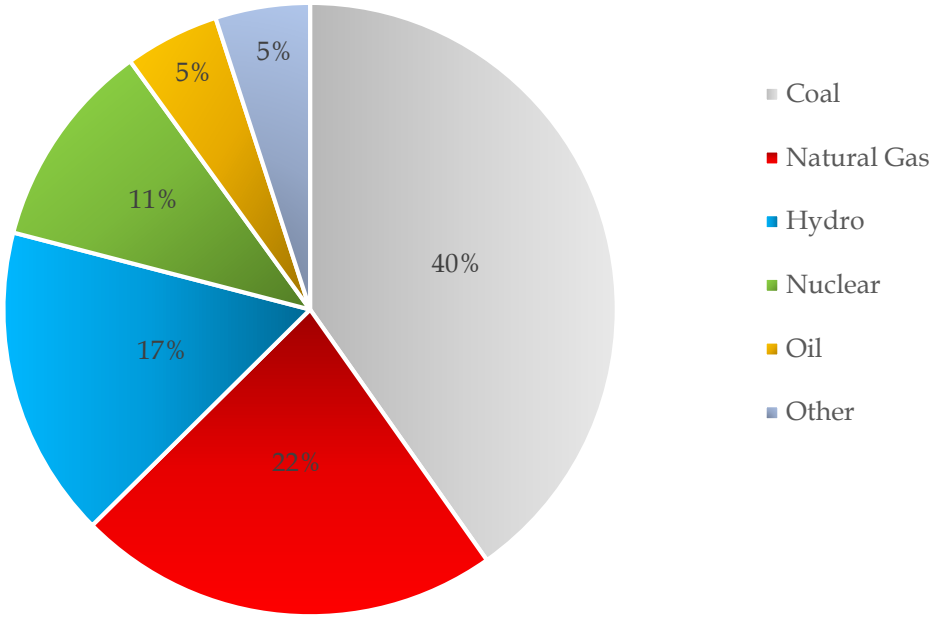

Figure 1-1. Worldwide electricity mix 2012 [2]

The first commercial nuclear power stations began operation in the 1950s. Today, there are over 435 commercial nuclear reactors operating in 31 countries, having a total capacity of over 375,000 MW_{el} [3]. As shown in Figure 1-1, they provide approximately 11% of the world's electricity as a continuous and reliable source for base-load power. While a nuclear reactor does have Carbon Dioxide (CO_2) emissions during its life cycle, there are no CO_2 emissions during normal operation. There are 16 countries that depend on nuclear power for at least a quarter of their electricity, with France receiving three quarters of its power from nuclear [3]. In Canada, nuclear energy accounts for approximately 15% of electricity production; this number increases to 55% in the province of Ontario. Canada has 22 reactors, 18 of which are

currently in service. The industry also provides a significant amount of jobs in Canada as the industry employs over 20,000 employees directly and 10,000 indirectly [4].

There is considerable interest in nuclear energy around the world, there are about 70 nuclear reactors currently under construction while there are over 160 firmly planned; this is equivalent to half of present capacity [3]. As the power industry continues to further itself from fossil fuels in an attempt to reduce CO_2 and greenhouse gas emissions, the nuclear industry is expected to grow. As previously mentioned nuclear energy is currently the only viable alternative that can effectively replace fossil fuel power plants. As a result, there is significant international effort to research and develop the new generation of reactors.

The Generation IV (Gen IV) International Forum (GIF) was established in 2001 to identify and develop Gen-IV nuclear energy systems that will improve upon the current fleet of nuclear reactors. Through this vision six nuclear reactor concepts have selected for further development: (1) Very-High Temperature Reactor (VHTR), (2) Sodium-cooled Fast Reactor (SFR), (3) SuperCritical Water-cooled Reactor (SCWR), (4) Gas-cooled Fast Reactor (GFR), (5) Lead-cooled Fast Reactor (LFR), (6) Molten Salt Reactor (MSR) [5]. Of these six concepts, Canada selected the SCWR for further research.

1.1 SuperCritical Water-cooled Reactors

The use of supercritical fluids is not new. Nature has been processing minerals in aqueous solutions near or above the critical point of water for billions of years [6, 7]. Analyzing heat transfer at supercritical pressures started as early as the 1930s. Schmidt et al. [8] investigated free-convection heat transfer of fluids at a near-critical state and they had found that the Heat Transfer Coefficient (HTC) was actually quite

high; this advantage was later applied in single-phase thermosyphons with the immediate working fluid being at the near critical point [9].

In the 1950s, the potential for supercritical water to increase the total thermal efficiency of coal-fired power plants became an attractive option leading to the investigation of SuperCritical Water (SCW) use in nuclear reactors at the beginning of the 1960s. This idea was then abandoned, likely due to material constraints [6]. Interest was regained in the 1990s after being abandoned for 30 years due to the successful deployment of Light Water Reactors (LWR).

As the name suggests, SCWRs are light-water-cooled reactors that operate above the critical point of water (22.064 MPa and 373.95°C) [10]. One of the main advantages of an SCWR is the economic improvement of the reactor due to a higher thermodynamic efficiency as well as the potential for plant simplification; thermodynamic efficiency is expected to increase to 45-50%. Improvements in other areas such as safety, sustainability, proliferation resistance and physical protection are also possible. Such improvements are being considered with various design options, including thermal and fast spectra and the use of advanced fuel cycles.

In general, there are currently two SCWR conceptual designs: (1) Pressure-Vessel (PV) and (2) Pressure-Tube (PT). Canada has adopted the PT concept as such it is generically called the Canadian SCWR. The Canadian SCWR is being designed to operate at pressures of 25 MPa with a reactor outlet temperature of 625°C [11, 12]. These operating conditions make the SCWR suitable candidates to support the cogeneration of hydrogen through the use of thermochemical cycles.

A general concept for an SCW NPP is shown in Figure 1-2. In this figure multiple products are shown and described as a key aspect towards the development of sustainable future and competitive designs. One such product shown is hydrogen through the use of reactor process heat.

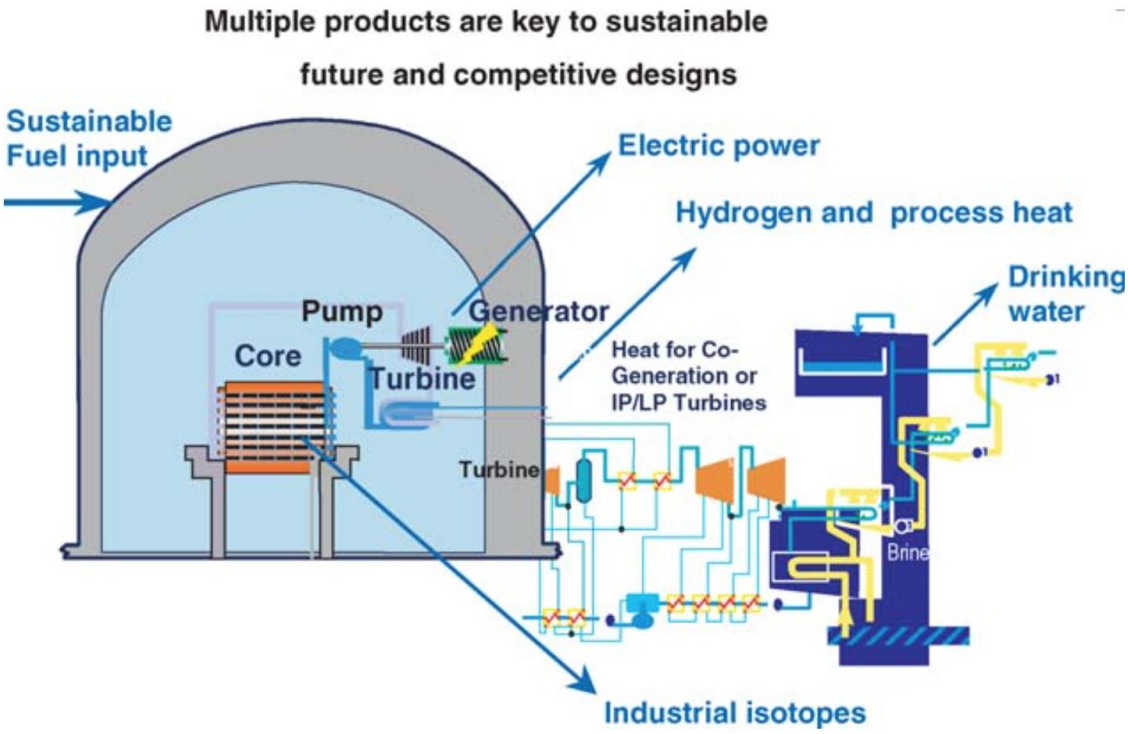

Figure 1-2. General concept of an SCW NPP [6]

It is clear that in order for the power industry to move towards cleaner electricity generation, the use of renewable sources such as hydro, wind, solar and nuclear power will be needed. Nuclear reactors cannot operate in transients to follow the peaks and drops in energy consumption during a typical day and should operate at full capacity. Therefore, in order to keep reactors operating at full power during off-peak hours, it would be very beneficial to use the process heat from the reactor for the cogeneration of hydrogen.

1.2 Hydrogen as an Energy Carrier

As discussed earlier in this chapter, fossil fuels currently dominate the energy landscape. While nuclear energy is seen as a viable replacement in the power industry, the significance of fossil fuels' role as an energy carrier extends to fields outside of power production; however, environmental impacts and depleting resources make it unlikely that these efforts can be sustained. Therefore, it is

important to identify possible alternatives that cannot only meet the growing energy demand, but as well as conform to the increasingly stringent restrictions on carbon emissions.

Hydrogen is needed in large quantities by many industrial sectors, such as the Canadian oil sands (bitumen upgrading), agricultural (ammonia for fertilizers) and petroleum product industries. In the transportation sector, hydrogen is widely expected to become the dominant energy carrier. The use of hydrogen as fuel for vehicles has the potential to greatly reduce pollution in urban city centres and greenhouse gas emissions [13]. While, the current trend has shown movement towards electric vehicles, limitations including battery recharge times, cold weather performance, and a relatively short range have hampered their growth.

Although hydrogen is considered to be a clean energy source, the current production techniques used to obtain hydrogen also generate CO_2. Approximately 97% of the world's hydrogen is currently derived from fossil fuels using a type of reforming process [13]. Significant effort has been made to develop sustainable hydrogen production techniques that will eliminate the use of fossil fuels, that is, a carbon free source of hydrogen.

Thermochemical cycles are being investigated as one potential method for the large-scale production of hydrogen. Through the use of immediate compounds, a series of physical and chemical reactions decompose water into oxygen and hydrogen. The process is completed without any emission of air pollutants with the intermediate compounds continuously being recycled in a closed loop [13]. Various sources of thermal energy can be integrated with thermochemical cycles in order to supply the heat necessary for the cycle's reactions; one such source is an SCW NPP. By using an SCW NPP for the external thermal energy, the heat requirement can be met without the use of fossil fuels.

One potential means for accomplishing this is to use an intermediate Heat eXchanger (HX) between a NPP and a hydrogen production facility. One thermochemical cycle currently being studied for this purpose is the Copper-Chlorine (Cu-Cl) cycle, which looks to be a suitable candidate due to its energy requirement [13].

Ultimately, the goal is to link an SCW NPP with a hydrogen production facility but because both of these facilities can be considered dangerous, they must be separated. In addition, the reactor coolant cannot be transferred outside of the containment boundary due to safety concerns. Therefore, an intermediate loop and working fluid is required to transfer heat efficiently from the high temperature reactor coolant to another medium at a hydrogen production facility.

It is known that SCW is an efficient heat transfer medium due to high HTCs [6]. As a result, SCW will be considered in the selection of intermediate working fluids. Furthermore, it may be safer to keep the intermediate working fluid at pressures slightly above 25 MPa of the reactor coolant. This is because in the event of a leak in the system, the reactor coolant will not flow into the intermediate loop and remain within the containment boundary. Additionally, on the other side of the loop, where another HX is to be used to transfer the heat from the intermediate working fluid to the internal loop of the hydrogen production facility, it may be beneficial to limit this pressure difference. Consequently, it is also important to investigate a supercritical CO_2 due to its significantly lower critical point, which is 7.3773 MPa and 30.98°C [10].

1.3 Objective

The objective of this thesis is to:

> Assess the performance of supercritical fluids in a conceptual design of an intermediate HX, which will link a Canadian SCWR to a hydrogen production facility.

The purpose of the HX is to use the process heat generated by a Canadian SCWR to produce hydrogen, using the thermochemical Cu-Cl cycle. This assessment aims to identify the potential benefits and limitations in the use of supercritical fluids in a hydrogen cogeneration system. These contributions will aid the development of hydrogen cogeneration technologies, as well as highlighting an additional product of the SCWR in its bid as a competitive design. In order to meet the stated objective, the following tasks will need to be completed:

1. Identify the thermal energy requirement for the 4-step Cu-Cl cycle.
2. Develop a preliminary HX design to be used for the application of hydrogen production.
3. Complete a heat transfer analysis on the intermediate HX that will be used to link a Canadian SCW NPP with a hydrogen production facility.
4. Compare the impact of different supercritical working fluids on the size of the HX.

Chapter 1 presents an introduction and states the objective of this thesis. Chapter 2 presents a review of surveyed literature. This includes an overview of hydrogen production technologies as well as information on Gen IV technologies with an emphasis on Canadian SCWRs. Thermophysical properties and empirical correlations of supercritical fluids are also discussed. Lastly, two different types of HXs are briefly described.

The methodology used to carry out the analysis in this thesis is presented in Chapter 3. This chapter contains design considerations used when developing the HX, including: several design requirements, the minimum thermal energy requirement that the HX needed to meet as well as considerations for piping material and dimensions. This chapter also describes the equations that were modelled to conduct the heat transfer analysis. The numerical model used to carry out these calculations is also described in this chapter. The results and analysis are presented in Chapter 4, including the results from two reference cases and several test cases conducted as a part of a sensitivity analysis. Concluding remarks and future work are described in Chapters 5 and 6, respectively.

Chapter 2. Literature Review

2.1 Overview of Hydrogen Production Technologies

As discussed in the opening chapter, 97% of hydrogen is currently produced through steam methane reforming or a gasification process using non-renewable resources such as fossil fuels [13]. These methods create additional challenges with the mitigation of greenhouse gas emissions. Gasifiers are used commercially to react a carbon-containing material with water (or steam) and oxygen, under reducing conditions (shortage of oxygen). They are widely used in the petrochemical industry to process heavy oil by-products in hydrogen [14]. For steam methane reforming, methane will react with steam in the presence of a catalyst to produce hydrogen, carbon monoxide and a relatively low amount of carbon dioxide [15].

While these processes are proven, new technologies may emerge that significantly increase hydrogen consumption and increase the demand for hydrogen as an energy carrier. This makes it important to develop sustainable hydrogen production methods. The benchmark method for producing hydrogen using only water as an input has been water electrolysis; however, this method is costly and also has a relatively low efficiency. Alternatives to water electrolysis using a variety of thermochemical cycles have been proposed since the early 1970s [16].

Water splitting through the use of thermochemical cycles is a promising technology that can be used for the sustainable and large scale production of hydrogen. Through the use of immediate compounds, a series of physical and chemical reactions will decompose water into oxygen and hydrogen [13]. The process is completed without the emission of any air pollutants as the only output products are water and hydrogen, while all other intermediate compounds are continuously recycled internally within a closed loop [16].

While over 200 thermochemical cycles have been identified, only a small percentage of them have progressed into operating experimental demonstrations that establish the practical and scientific feasibility of these cycles [13, 17, 18]. Consideration of the following factors led to identification of the seven most promising thermochemical cycles by the Hydrogen Initiative: availability, abundance of materials, simplicity, chemical viability, thermodynamic feasibility, as well as control and issues relating to safety [13, 18]. Two of the prominent cycles currently under development worldwide are the Sulfure-Iodine (S-I) and Cu-Cl cycles [19, 20, 21].

There are a number of distinct advantages for the Cu-Cl cycle, which include lower demands on materials of construction, common chemical agents and reactions going to full completion. In addition, one of the more significant advantages is the lower operating temperatures [19]. While many thermochemical cycles, including the S-I cycle, require process heat above 800^{o}C, the maximum temperature requirement for the Cu-Cl cycle is approximately 530^{o}C [19, 13].

It is because of this relatively lower temperature requirements that the Cu-Cl cycle is considered to be a promising alternative that could be eventually linked with a Gen IV SCWR. In this case, a fraction of the reactors coolant would be diverted to an intermediate HX, where it would exchange heat with an intermediate fluid. As a result, the reactor process heat can be used to facilitate the thermochemical production of hydrogen [19].

The efficiency of thermochemical hydrogen production with the Cu-Cl cycle is greater than that of electrolysis via thermal power plants. In the case of the Cu-Cl cycle, heat can be used directly to produce hydrogen. For electrolysis, the heat would be used indirectly as electricity would first need to be generated, after which hydrogen could then be produced. Using a Gen IV SCWR, the net efficiency of electrolysis for hydrogen production would be approximately 30% [13]. Aspen Plus simulations for the Cu-Cl have shown an efficiency of about 43% to be realistic [22].

There are several variations of the Cu-Cl cycle, including 3-step, 4-step and 5-step cycles. Recent focus has shifted to the 4-step option due to its advantages in thermal efficiency and practical viability [13]. The 4-step cycle removes complexity from the 5-step cycle as the combination of steps eliminates the need to handle solid cupric chloride particles. The 3-step cycle on the other hand has a maximum temperature requirement of 600°C, which is greater than 530°C temperature requirement for both the 4-step and 5-step variations of the cycle [23].

The 4-step Cu-Cl cycle requires a net heat input of 257 kJ/g of hydrogen with 46 kJ/g available for recycling. Assuming that 50% of the heat generated within the cycle is recoverable, the net thermal energy requirement, Q, is 224 kJ/g of hydrogen produced. Using a commercial scale hydrogen production rate of 1 kg/s, the power requirement becomes 224 MW_{th} [24, 25].

This work is based on the requirements of the 4-step Cu-Cl cycle. Table 2-1 lists the associated temperature requirements with the four main steps involved in the 4-step Cu-Cl cycle; a schematic of the cycle is shown in Figure 2-1, where the maximum input heat requirement is highlighted in red.

Table 2-1. Temperature ranges for chemical reactions in the 4-step Cu-Cl Cycle [19]

Step	Reaction	Temperature Range (°C)
1	$2CuCl_{(aq)} + 2HCL_{(aq)} \rightarrow H_{2(aq)} + 2CuCl2_{(aq)}$	<100
2	$CuCl_{2(aq)} \rightarrow CuCl_{2(s)}$	<100
3	$2CuCl_{2(s)} + H_2O_{(g)} \rightarrow Cu_2OCl_{2(s)} + 2HCL_{(g)}$	400
4	$Cu_2OCl_{2(s)} \rightarrow 2CuCl_{(l)} + ½O_{2(g)}$	500

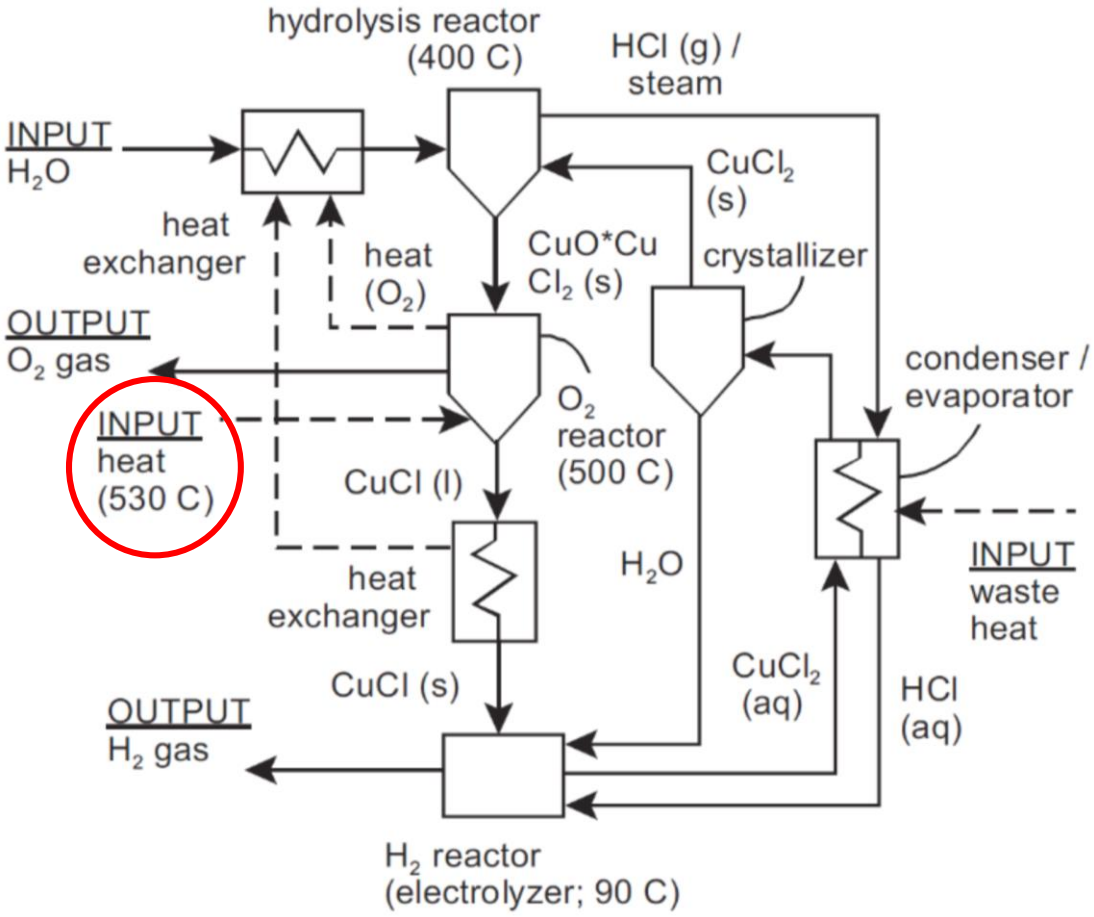

Figure 2-1. Schematic of the Cu-Cl cycle [19]

Using a methodology proposed by Ribando et al. [26], research has previously been conducted by Lukomski et al. [27] on an SCW-to-superheated steam HX for the purpose of hydrogen production using SCWR process heat. It was shown that to achieve the thermal energy requirement associated with a production rate of 1 kg/s would require 3205 pipes at a length of 49.3 m per pipe. The total heat transfer surface area was determined to be 13,140 m^2. Improvements to the overall HTC were recommended to reduce the overall size of the HX. To address this issue, the work presented in this thesis investigates hydrogen production through the use of supercritical fluids. Supercritical fluids are considered as opposed to superheated steam due to potential improvements on heat transfer, which in turn will reduce the size of the HX. Therefore, the performance of different supercritical fluids in this type of application are assessed to determine any benefits or limitations to their use.

2.2 Generation IV Technologies

Nuclear energy is expected to play a large role in meeting the world's growing energy needs; however, there are still challenges that must be met. As such, the advancement of nuclear reactors is vital for the large-scale use of nuclear energy. In 2001, ten countries formed GIF as a collaborative international effort to develop the fourth generation of nuclear reactor systems. Currently, GIF has 13 members including Argentina, Brazil, Canada, Euratom, France, Japan, China, Korea, South Africa, Russia, Switzerland, United Kingdom and the United States [11].

In order to guide the development of the Gen IV reactor systems, GIF created a technology roadmap, where the methodology of roadmapping was used to define and manage the planning and execution of large-scale R&D efforts [28]. As a part of this roadmap, goals for the Gen IV reactors were established. Eight goals were defined in four broad areas of sustainability, economics, safety and reliability, and proliferation resistance and physical protection.

Sustainability goals focuses on fuel utilization and waste management. Goals related to economics aim towards competitive life cycles and energy production costs and financial risk. Safety and reliability goals focus on the safe and reliable operation of the reactors, improved accident management as well as the minimization of consequences. Additional goals in this area also include investment protection and the elimination of the technical need for off-site emergency response. Lastly, proliferation resistance and physical protection goals focus on the control and security of nuclear material and facilities [28].

Using these goals as well as other selection criteria described in the technology roadmap, six Gen IV reactor systems were selected for further R&D [28].

2.2.1 Generation IV Reactor Concepts

The six Gen IV reactor concepts currently undergoing R&D are: (1) Very-High Temperature Reactor (VHTR), (2) Sodium-cooled Fast Reactor (SFR), (3) SuperCritical Water-cooled Reactor (SCWR), (4) Gas-cooled Fast Reactor (GFR), (5) Lead-cooled Fast Reactor (LFR), (6) Molten Salt Reactor (MSR). Each reactor is described briefly in the paragraphs below.

VHTRs are graphite-moderated, helium-cooled reactors that utilize a thermal neutron spectrum. Core outlet temperatures range between 700°C and 950°C, with a potential for more than 1000°C in the future. Currently, there are two major options for the reactor core of the VHTR, which can either be a prismatic-block type such as the Japanese High-Temperature Test Reactor (HTTR) or a pebble-bed type reactor.

SFRs are fast-reactors that use liquid sodium as the reactor coolant. Current plant size options range from small modular reactors (50 to 300 MW_{el}) to larger plants (up to 1500 MW_{el}). Outlet temperatures for these options are in the range of 500-550°C. SFRs are considered to be an attractive option for nations with limited fuel sources looking to manage nuclear waste.

SCWRs are high-temperature, high-pressure water-cooled reactors. There are currently two main categories in which conceptual designs can be grouped, a Pressure Vessel (PV) concept and a Pressure Tube (PT) concept. The reference reactor design has an operating pressure of 25 MPa and a reactor outlet temperature of up to 625°C.

GFR systems are high-temperature helium-cooled reactors that utilizes a fast-spectrum operating on a closed fuel cycle. It combines the advantages of fast-spectrum systems and high-temperature systems, such as waste minimisation and high thermal efficiency. The current reference design for the GFR is a 2400 MW_{el} reactor core with core outlet temperatures up to 850°C.

LFRs utilize a fast-neutron spectrum along with a closed fuel cycle. The current proposed design options for the LFR are two pool-type reactors, the Small Secure Transportable Autonomous Reactor (SSTAR) and the European Lead-cooled SYstem (ELSY). The reference design for the SSTAR is a 20 MW_{el} reactor cooled via natural circulation. The ELSY reference design is a 600 MW_{el} reactor utilizing a molten lead coolant.

MSRs currently have two main subclasses. In the first of these subclasses, fissile material is dissolved into the molten fluoride salt. In the second subclass the molten fluoride salt serves as the coolant to a coated particle fuelled core. The reference design for the MSR is 1000 MW_{el} reactor with reactor outlet temperatures up to 850^{o}C.

2.2.2 SWCR Concepts

SCWR concepts are currently being developed worldwide. As mentioned in the previous section, these concepts can be divided into two main categories: (1) the PV concept and (2) the PT concept. Of these two concepts, Canadian research on the SCWR is being conducted on the PT concept because of experience with pressure tubes from CANada Deuterium Uranium (CANDU) reactors, while the U.S. is researching the PV design as it is comparable to current Pressurized Water Reactor (PWR) designs. This work focuses on the PT design, which will be referred to as the Canadian SCWR from this point forward.

In the current conceptual design for the Canadian SCWR, high temperature and high pressure SuperCritical Water (SCW) is directed from the reactor core into the SCW turbines. Canadian SCWR concepts are being designed to have an operating pressure of 25 MPa with reactor core outlet temperature up to 625^{o}C. It is because of these operating conditions that Canadian SCWRs are being considered for the cogeneration of hydrogen through the use of thermochemical cycles. Through the use

of SCW and a simpler, direct-cycle for the layout of the plant, the thermal efficiency of the reactor can be increased up to 48% [10, 29].

Similar to current CANDU reactors, conceptual Canadian SCWRs have adopted a modular design where the coolant is kept separate from the moderator. Along with the moderation provided during normal operation, separating the moderator from the reactor coolant also has the benefit of increasing the safety of the reactor. The severity of a loss of coolant accident can be reduced due to the passive heat sink that is provided by the moderator, therein by potentially reducing the damage to the core of the reactor [30].

Canadian SCWRs are currently designed to utilize a light water coolant. The current concept features a vertical reactor core containing 336 fuel channels, with each channel housing a 5 m long fuel assembly. Surrounding the fuel channels is the relatively low-pressure and low temperature heavy water moderator which is housed inside of calandria vessel, once again similar to that of a CANDU reactor. This Canadian SCWR concept is currently designed to generate approximately 2540 MW_{th} and approximately 1200 MW_{el} [29].

A schematic for the conceptual design of the Canadian SCWR core is shown in Figure 2-2; major parameters are listed in Table 2-2.

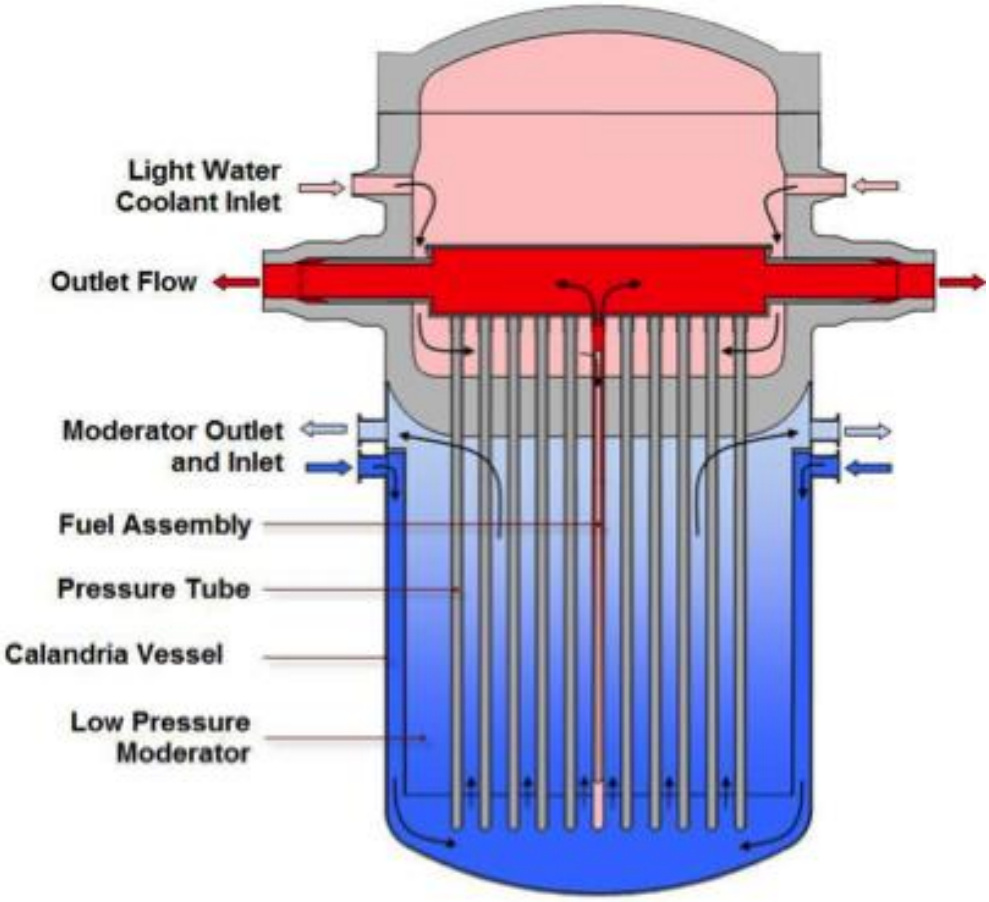

Figure 2-2. Schematic of the Canadian SCWR core concept [12]

Table 2-2. Major parameters of the Canadian SCWR concept [31]

Parameters	**Canadian SCWR**
Thermal power (MW_{th})	2540
Electric power (MW_{el})	1200
Thermal efficiency (%)	~48
Pressure (MPa)	25
Inlet temp. (^{o}C)	350
Outlet temp. (^{o}C)	625
Total Mass Flowrate (kg/s)	1320

2.2.3 SCW NPP Layouts

In the previous section, certain aspects of the current design of the Canadian SCWR were discussed. While there are various design options currently being developed, there are also various NPP cycle layouts that are being considered. Each of these layouts can be applied to either the PV or Canadian designs of the SCWR, however, the focus of the discussion will remain on the Canadian SCWR.

In order to meet the objective of this thesis, a heat transfer analysis on an intermediate HX linking a Canadian SCWR with a hydrogen production facility was performed. As a result, the cycles and layouts discussed in this section are being considered with the intention for hydrogen cogeneration.

There are three cycles that have been considered with Canadian SCWRs. These three cycles are the direct, indirect and dual cycle options. In the direct cycle, the SCW reactor coolant is fed directly from the outlet of the reactor to the supercritical turbines. In doing this, the layout of the plant becomes more simplified as steam generators are removed from the cycle. Along with the simplification of the plant, this also reduces the total cost of the plant. This concept is based on the cycles employed by current Boiling Water Reactor (BWR) NPPs [32].

Indirect cycles make use of steam generators to transfer heat from the coolant of the reactor, to the fluid on the secondary side of the plant. This secondary fluid is then fed to the turbines. This concept is similar to that of the cycles currently being used by PWR and CANDU NPPs. Due to the addition of a steam generator, the thermodynamic efficiency of an indirect cycle is lower than that of a direct cycle. This can be attributed to a reduction in the maximum temperature of the secondary fluid due to the heat transfer process through the steam generators. With this decrease in plant efficiency, there is an added benefit in terms of safety. Since the coolant does not flow directly into the turbine, radioactive particles are maintained within the

primary loop. Dual cycles are used to combine aspects both direct and indirect cycles in order to improve efficiency [32]. As mentioned in the previous section, current Canadian SCWR concepts are based on a direct cycle [29].

Integrating a large-scale hydrogen production facility, based on the 4-step Cu-Cl cycle, with an SCW NPP allows for hydrogen production during off-peak hours using reactor process heat. A percentage of the reactor coolant will be diverted to an intermediate HX, where it will exchange heat with an intermediate working fluid. After leaving the HX, the coolant would then be redirected back to the reactor. Along with the aforementioned cycles, reheating options have also been investigated for SCW NPPs. Two viable reheating options that have been investigated are the single-reheat and no-reheat options. Previous studies have been conducted to determine the ideal heat-extraction points based on the single-reheat and no-reheat options for an SCW NPP.

The single-reheat option introduces steam-reheat channels to the reactor core. The purpose of these channels are to reduce the amount of moisture in the last stages of the turbine. When compared to the no-reheat option, the addition of the reheat channels also improves the efficiency of the cycle due to the extra heat that is added during the reheating stage [33]. While a double-reheat option was investigated, it was determined that such a complicated configuration would dramatically increase the complexity of the design, therein by significantly increasing construction costs. As a result, it was no longer considered of interest [32]. The single-reheat cycle has a direct, regenerative configuration. The SCW from the reactor is expanded in the High Pressure (HP) turbine. At this point, the steam is then sent back into the reactor through the steam reheat channels, where the temperature is raised to superheated conditions. From there, the relatively low-pressure superheated steam is then directed to the Intermediate Pressure (IP) turbine, where it is expanded and then sent to the Low Pressure (LP) turbines. A schematic for a single-reheat cycle of an SCW NPP is shown in Figure 2-3 [32].

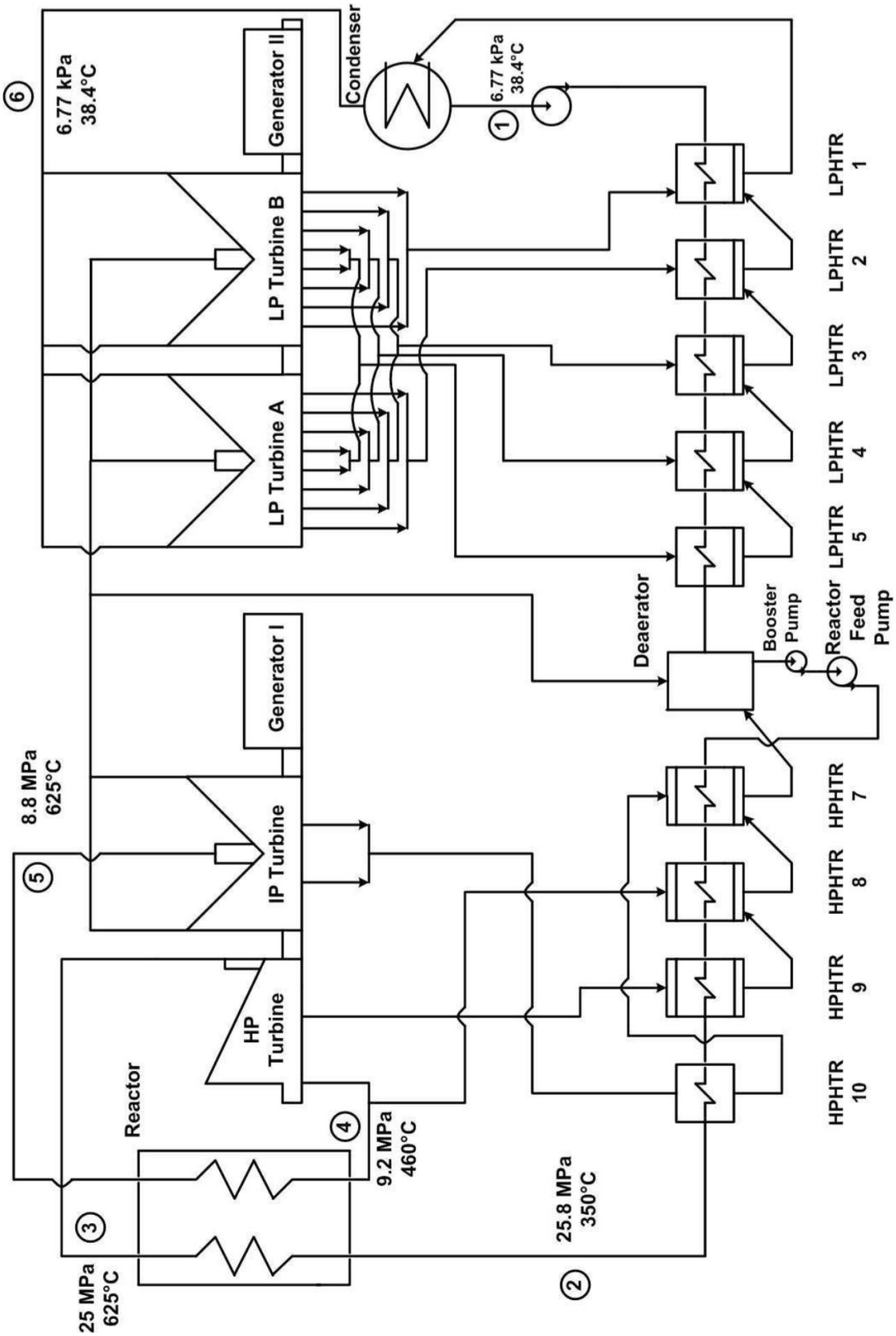

Figure 2-3. Single-reheat cycle for an SCW NPP [32]

For the single-reheat cycle shown in Figure 2-3, two potential heat extraction points for hydrogen cogeneration were identified. These two points are identified in Figure 2-4. At both of these points the reactor coolant is at approximately 625°C, however, the pressure of the coolant at these two points is very different. At the first point, the reactor coolant is in a supercritical state as the pressure is approximately 25 MPa. At the second point, the reactor coolant is superheated steam as the pressure of the fluid is much lower, at approximately 8.8 MPa. At this second point, the coolant is returning from the reactor through steam reheat channels after already being expanded through the HP turbine. Upon returning from the intermediate HX, the coolant would be added to the feedwater heating system at a suitable point of re-entry [32].

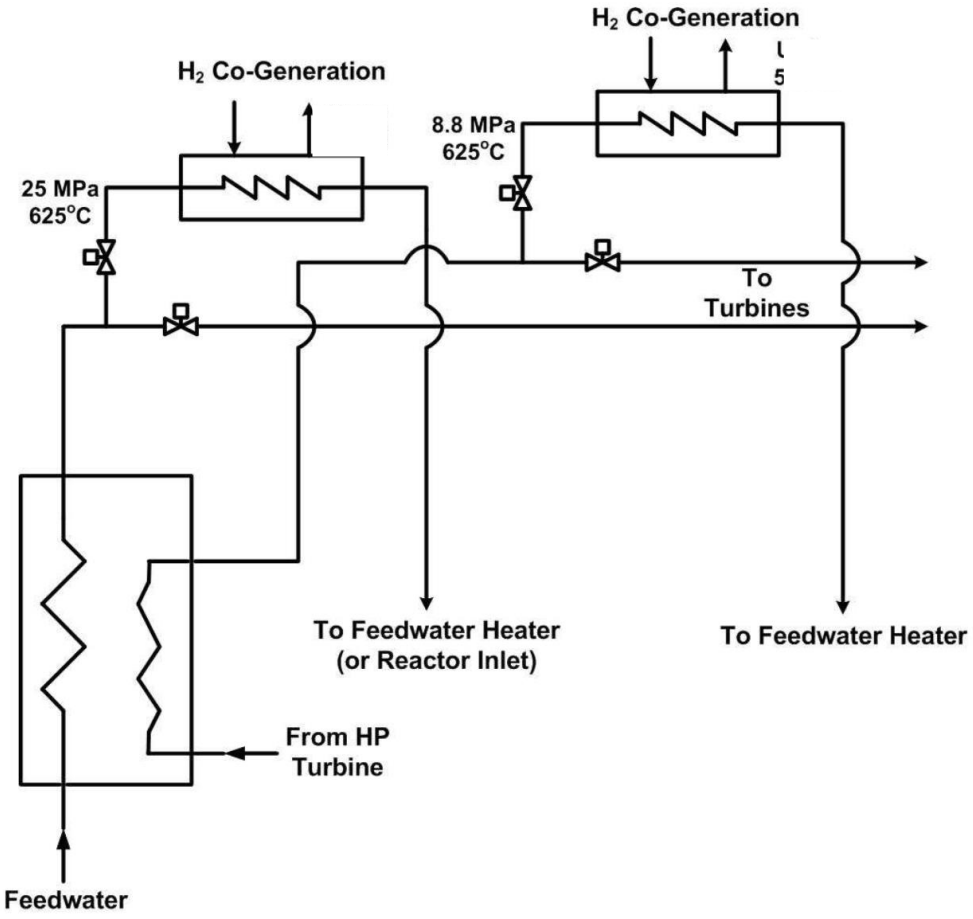

Figure 2-4. Heat-extraction points for H_2 cogeneration with single-reheat SCW NPP [32]

The maximum temperature requirement for the 4-step Cu-Cl is approximately 530°C. Since the temperature of the coolant is greater than this value at both heat extraction points in the single-reheat cycle, the coolant can sufficiently heat the intermediate working fluid using either extraction point. Therefore, the major difference between these two points is the state of the fluid.

The state of the fluid has an impact on the heat transfer characteristics of the fluid. SCW has a greater HTC than superheated steam. This is due to the thermophysical properties of the fluids as explained in Section 2.3.

The single-reheat cycle has been discussed in detail. The single-reheat cycle adds steam-reheat channels to the core of the reactor. While that may improve the efficiency of the cycle, it also increases the complexity of the reactor core. As a result, this increase in complexity could negatively impact current design efforts as well as construction costs in the future. Ultimately, this can prove to play a major role in the decision of whether or not steam reheat channels are used in Canadian SCWRs. Therefore, the no-reheat cycle is also considered candidate for the configuration of an SCW NPP.

The no-reheat cycle also has a direct, regenerative configuration. SCW is directed from the outlet of the reactor to a double-flow HP turbine where it is expanded to superheated conditions. From here the superheated steam is directed to two LP turbines. A schematic for a no-reheat cycle of an SCW NPP is shown in Figure 2-5 [32].

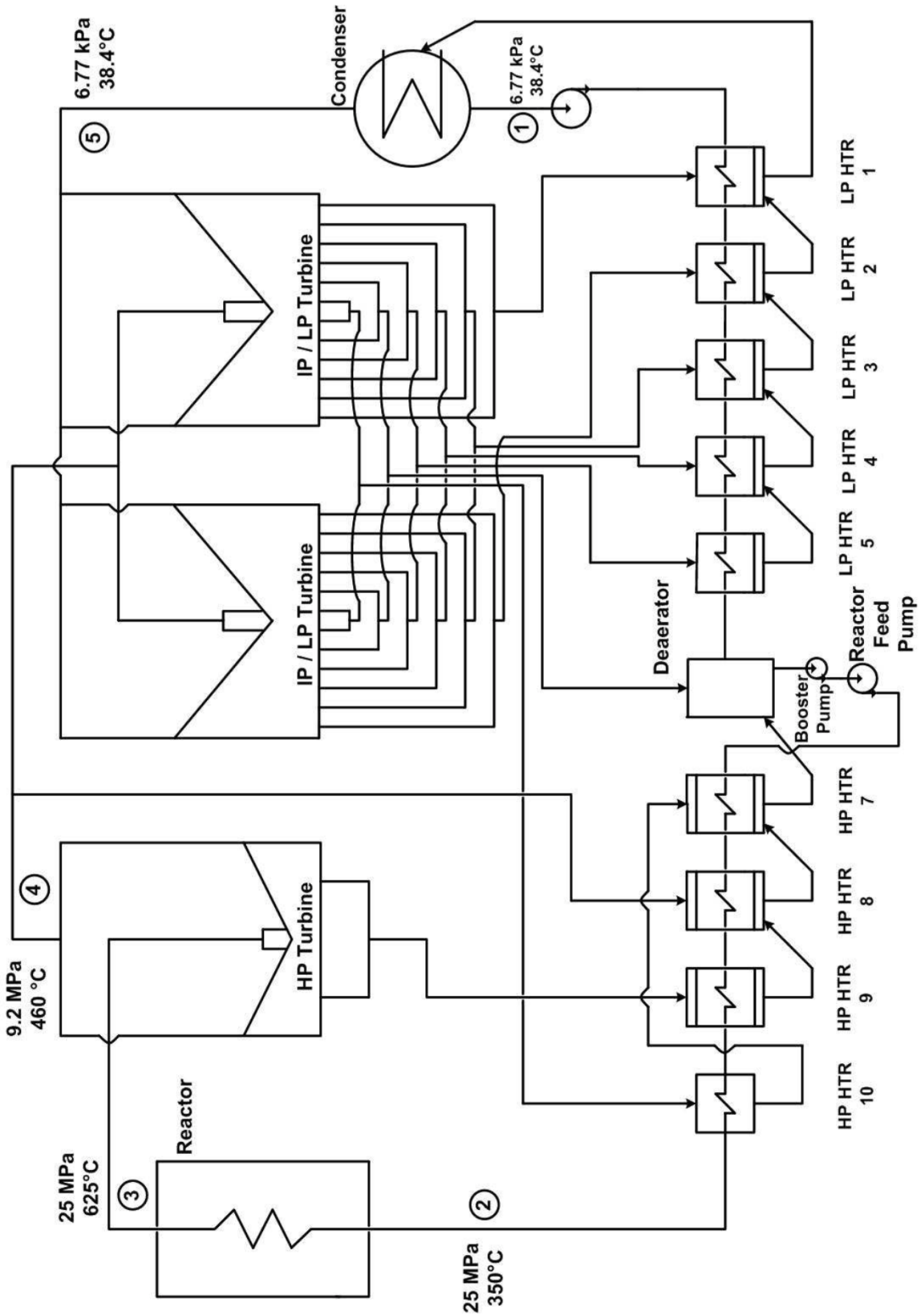

Figure 2-5. No-reheat cycle for an SCW NPP [32]

For the no-reheat cycle shown in Figure 2-5, three potential heat extraction points for hydrogen cogeneration were identified. These points are shown in Figure 2-6 [32]. Based on the extraction points shown in Figure 2-6, it is evident that the ideal heat-extraction point is at the reactor outlet. At this point, highlighted in red, the coolant is leaving the reactor at a pressure of 25 MPa and a temperature of 625°C. At these conditions, the coolant would be able to sufficiently heat the intermediate working fluid of the HX to the required temperature. At the two other extraction points shown, the coolant would be at temperatures of approximately 460°C and 500°C. In each of these two cases, an additional source of heat would be required. As a result, these two points were not assessed further. Similar to the case of the single-reheat layout, the ideal heat extraction point for the no-reheat cycle would be at the outlet of the reactor. Therefore, due to the temperature and pressure of the coolant, the heat extraction point was selected at the reactor outlet of the no-reheat cycle.

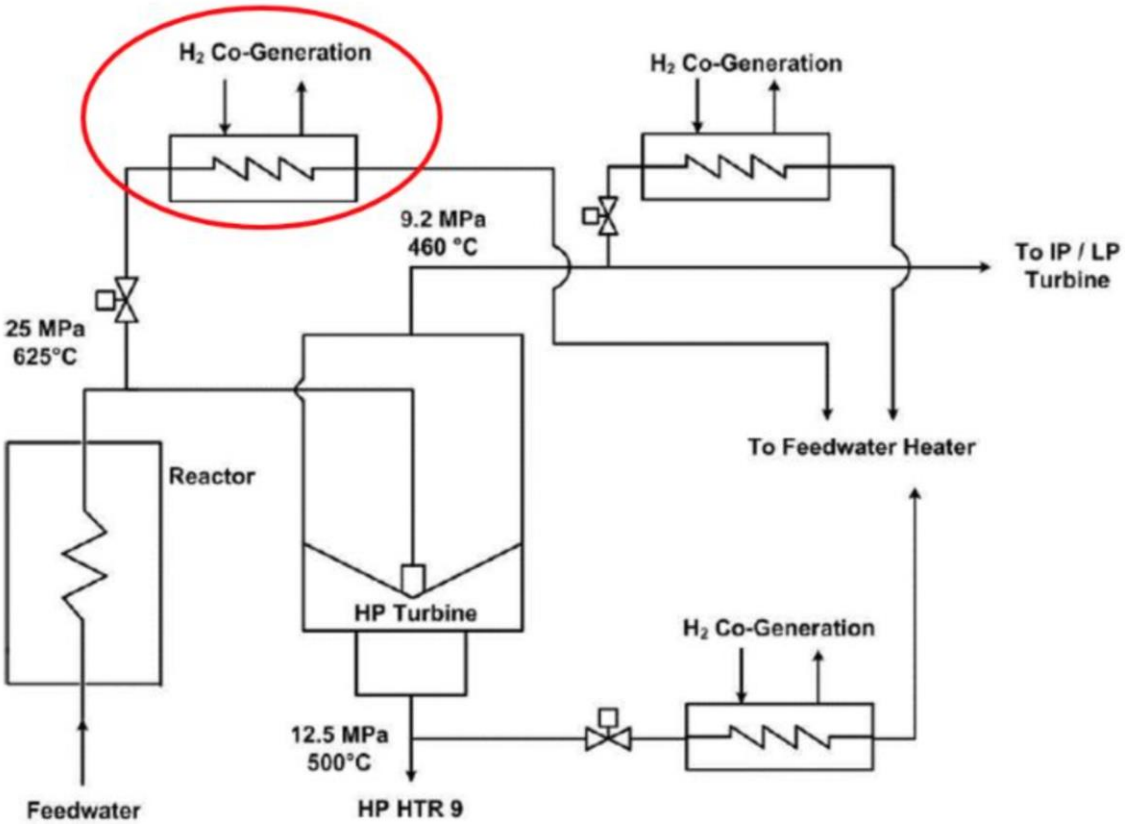

Figure 2-6. Heat-extraction points for H_2 cogeneration with no-reheat SCW NPP [32]

2.3 Thermophysical Properties of Supercritical Fluids

The critical point is the point where the distinction between liquid and gas (vapour) phases disappear. The critical point is characterized by the parameters critical temperature, T_{cr}, and critical pressure, P_{cr}, which are unique for each pure substance. When a fluid is at a temperature and pressure above its critical point, it is considered to be a supercritical fluid [6]. The critical point for water is 22.064 MPa and 373.95°C [10]. A pressure vs. temperature diagram for water is shown in Figure 2-7.

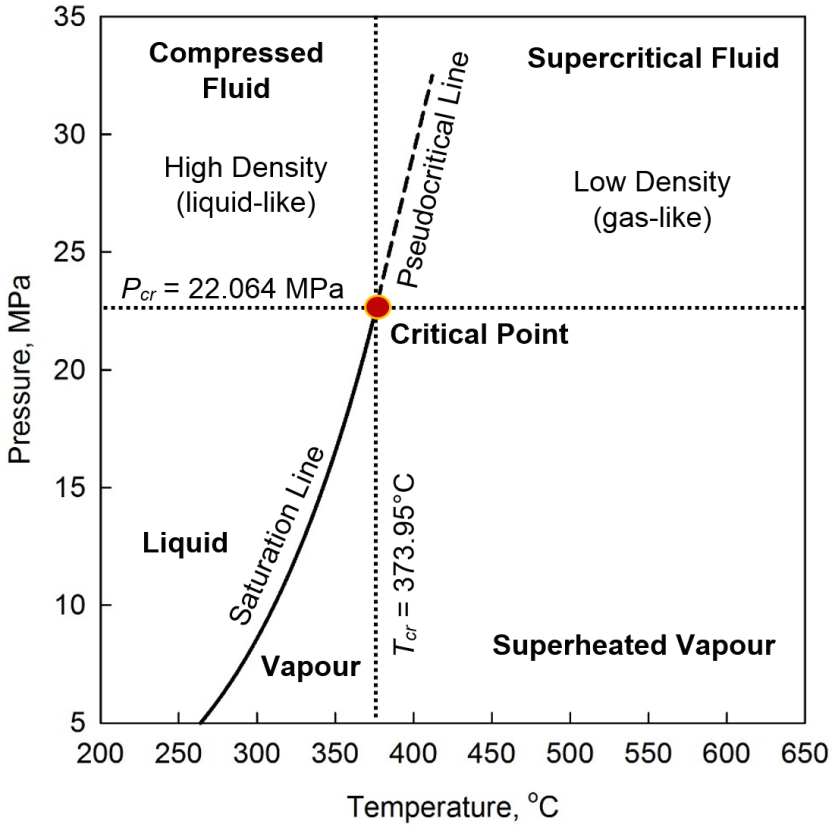

Figure 2-7. Pressure vs. temperature diagram for water

Supercritical fluids behave much differently than fluids in a subcritical state. At the critical and supercritical pressures, a fluid is considered to be a single-phase substance even though the thermophysical properties of supercritical fluid undergo significant variations around the pseudocritical point.

The pseudocritical point is a point at a pressure that is above both the critical pressure and at a temperature corresponding to the maximum value of specific heat at this particular pressure. The region at which these variations take place is known as the pseudocritical region. For water, the pseudocritical region is approximately ±25°C around the pseudocritical point [6]. Variations in thermal conductivity, density, specific heat and dynamic viscosity are shown in Figure 2-8. Properties were obtained from the NIST REFPROP software using increments of 0.5°C.

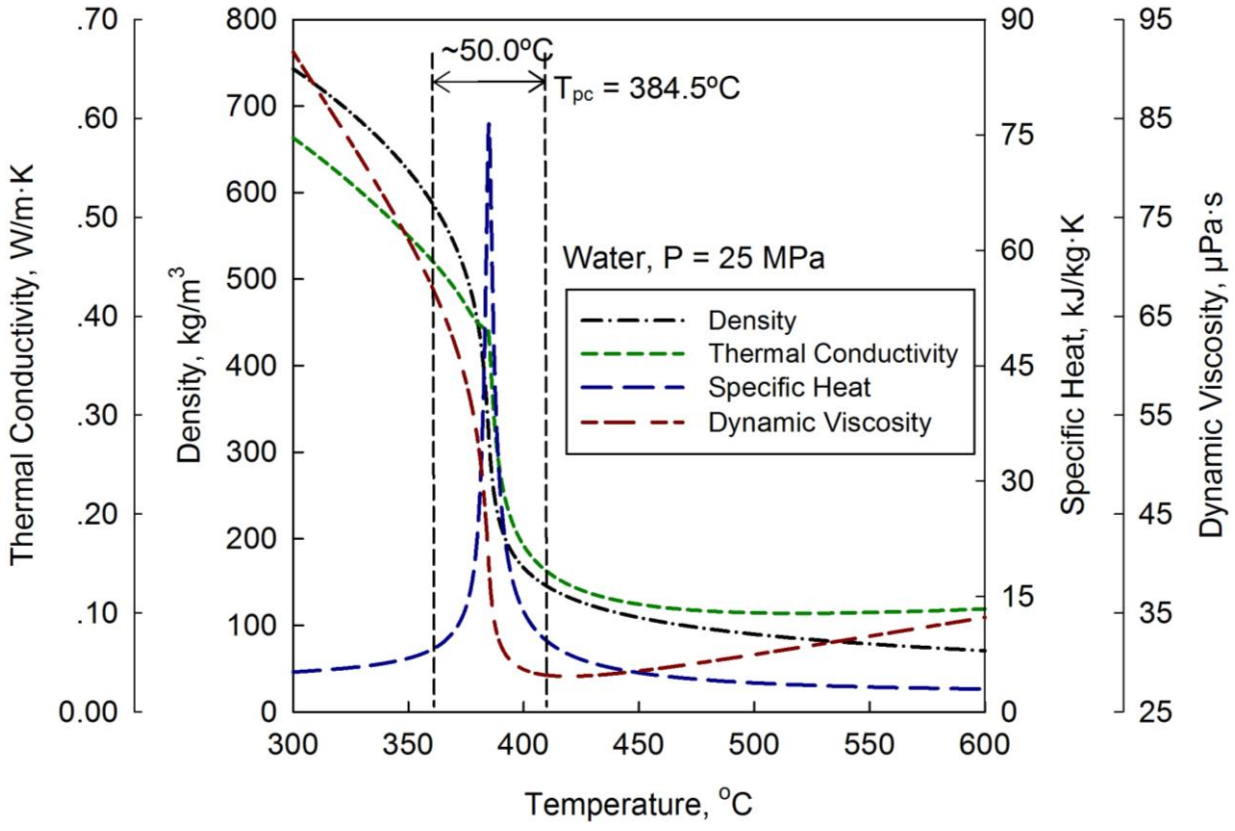

Figure 2-8. Selected thermophysical properties of supercritical water at 25 MPa

As shown in Figure 2-8, the thermophysical properties of a supercritical fluid undergo significant variations in the pseudocritical region. There is a significant decrease in fluid density and dynamic viscosity in the pseudocritical region. Thermal conductivity decreases, experiences a local peak and begins to decrease again. The specific heat of the fluid experiences a peak at the pseudocritical point, which is at approximately 384.5^{o}C, when water is at 25 MPa.

While this variation is evident at all pressures above the supercritical point, the trends show a decrease in severity with an increase in pressure. Figure 2-9 through Figure 2-16 were developed to show how changes in pressure impact the thermophysical properties for water. Data for these figures was obtained from NIST REFPROP software using increments of 0.5^{o}C. As shown in these figures, the variation of properties can be seen at the critical pressure (P_{cr} = 22.064 MPa) as well as two additional supercritical pressures (25 MPa and 28 MPa). The variation in these profiles are most apparent around the critical point and become less apparent as the pressure increases.

Density and dynamic viscosity experience significant drops within a small temperature range; the drop is almost vertical around the critical point (see Figure 2-9 and Figure 2-10). The opposite is shown for specific enthalpy and kinematic viscosity, where the values of these properties increase rapidly around the critical point; once again, this is less pronounced at higher pressures (see Figure 2-11 and Figure 2-12).

The profiles for Prandtl number, specific heat, thermal conductivity and volume expansivity all show peaks around the critical and pseudocritical regions, with the most visible peaks occurring at the critical pressure (see Figure 2-13, Figure 2-14, Figure 2-15 and Figure 2-16). Another aspect worth noting is that the peaks shown in these figures become less pronounced with an increase in pressure showing a smaller height to width ratio.

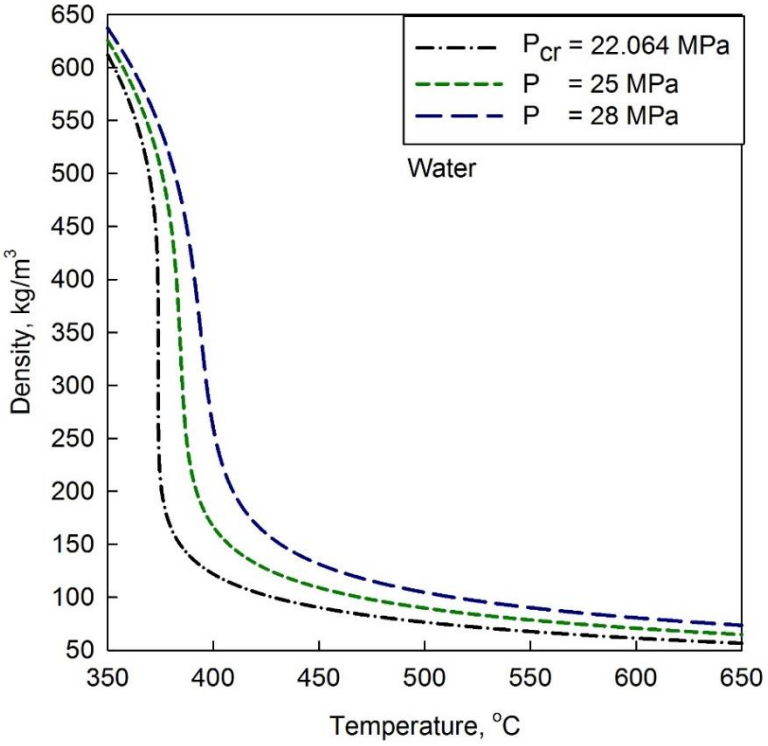

Figure 2-9. Water: Density vs. temperature

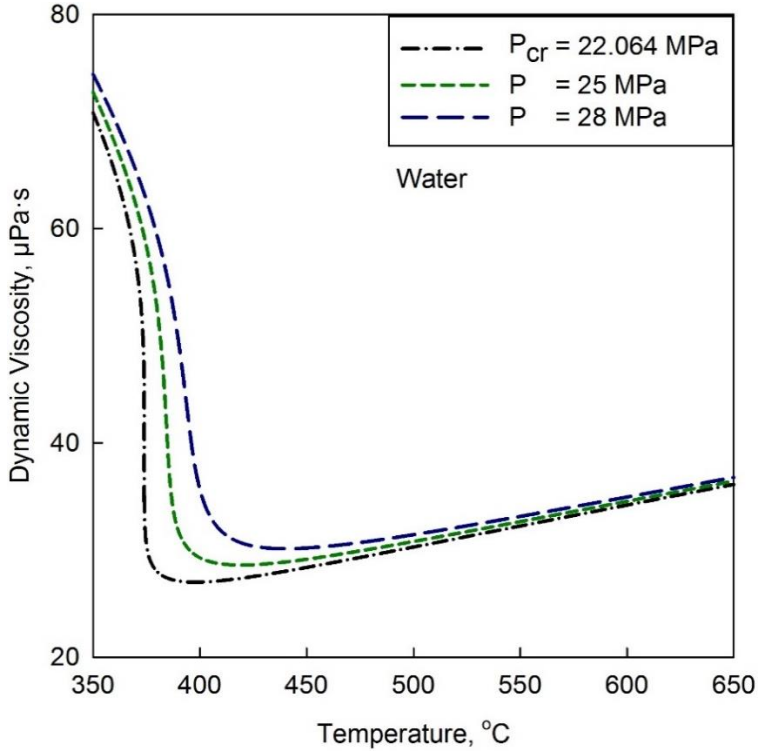

Figure 2-10. Water: Dynamic viscosity vs. temperature

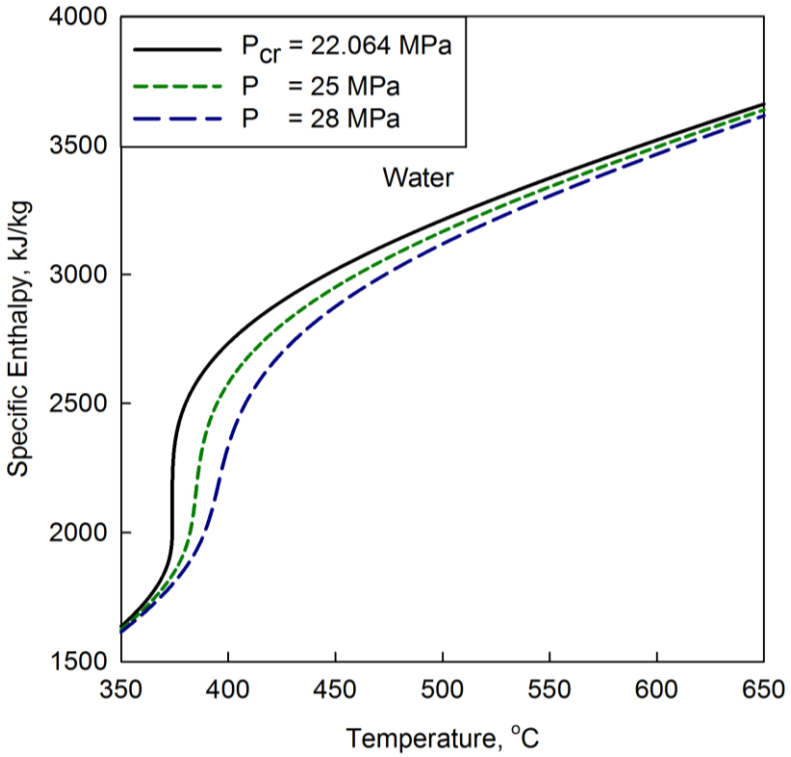

Figure 2-11. Water: Specific enthalpy vs. temperature

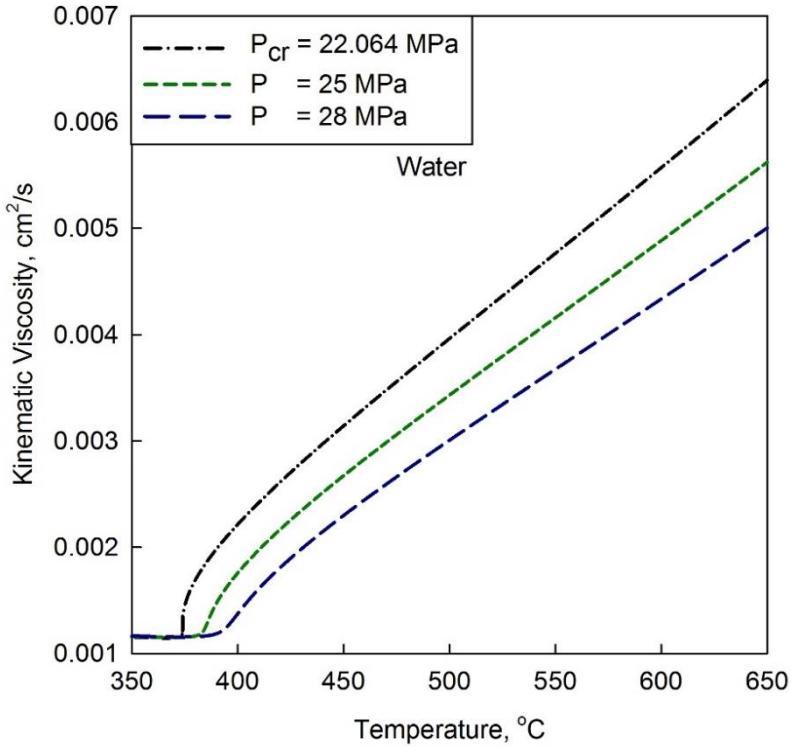

Figure 2-12. Water: Kinematic viscosity vs. temperature

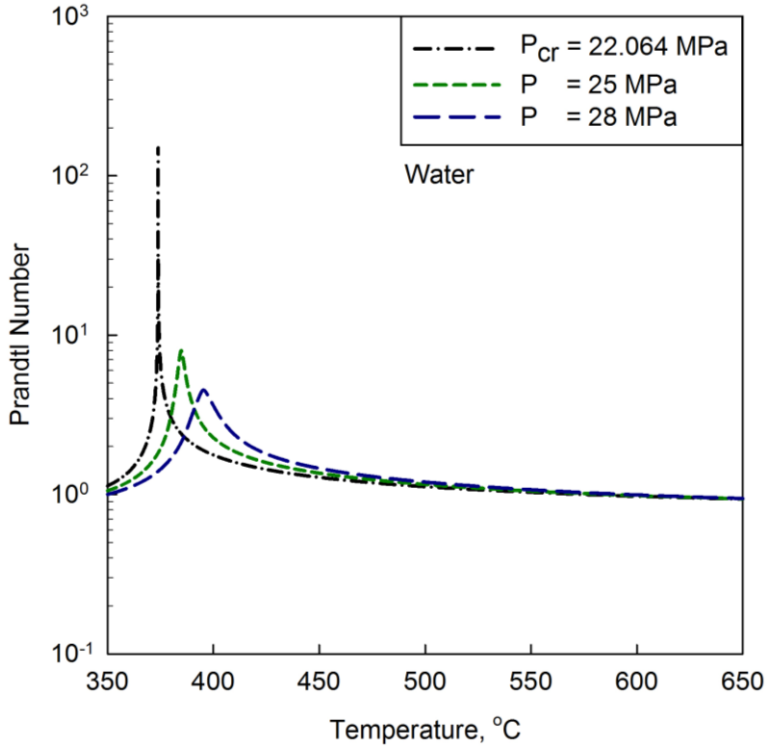

Figure 2-13. Water: Prandtl number vs. temperature

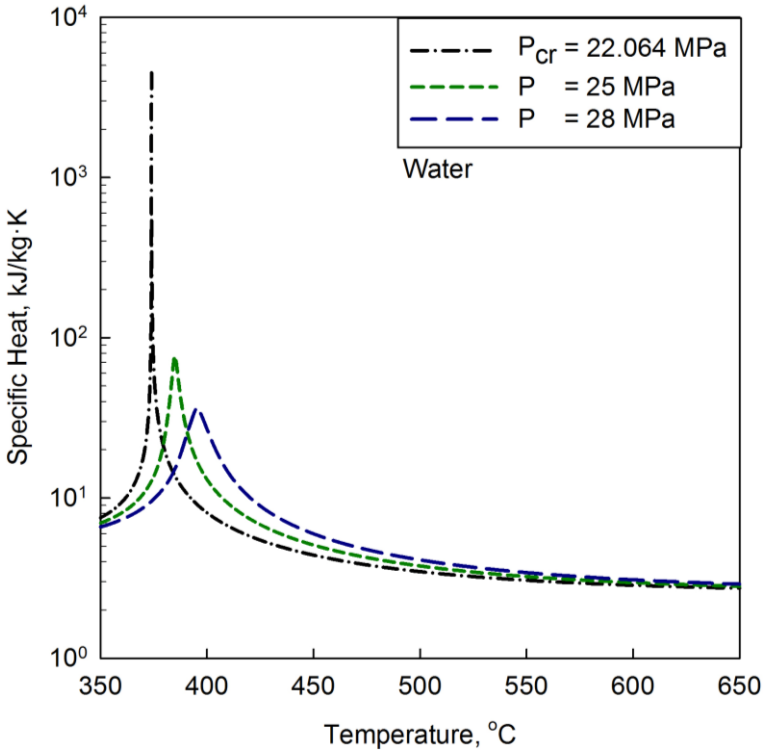

Figure 2-14. Water: Specific heat vs. temperature

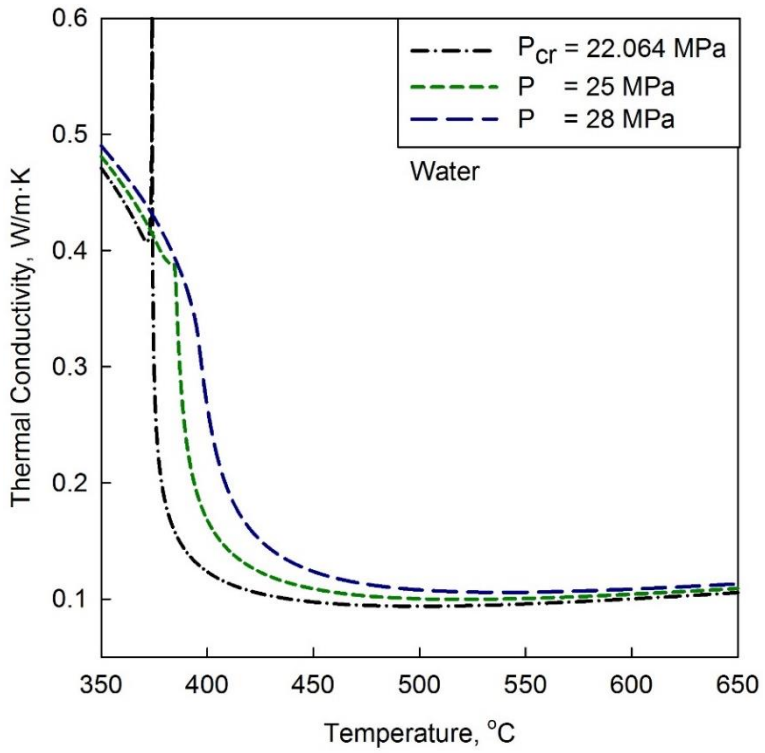

Figure 2-15. Water: Thermal conductivity vs. temperature

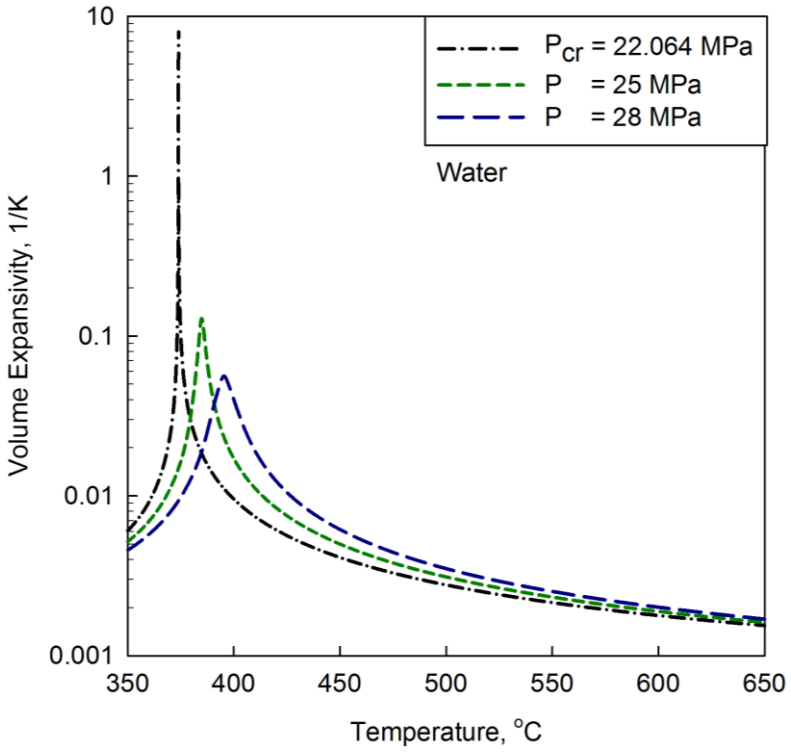

Figure 2-16. Water: Volume expansivity vs. temperature

In general, crossing the pseudocritical line from left to right, as shown in Figure 2-7, is similar to crossing the saturation line from liquid to vapour. The major difference in crossing these lines at supercritical conditions, as opposed to subcritical conditions, is that all the changes in themophysical properties are continuous. In subcritical conditions, there is a discontinuity in properties on the saturation line as shown in Figure 2-17.

The discontinuity shown in Figure 2-17 represents the phase change that the fluid is undergoing as there is one value for vapour and another value for the liquid phase. Therefore, since this discontinuity does not exist in the properties of supercritical fluids, they have been characterized as single-phase substances.

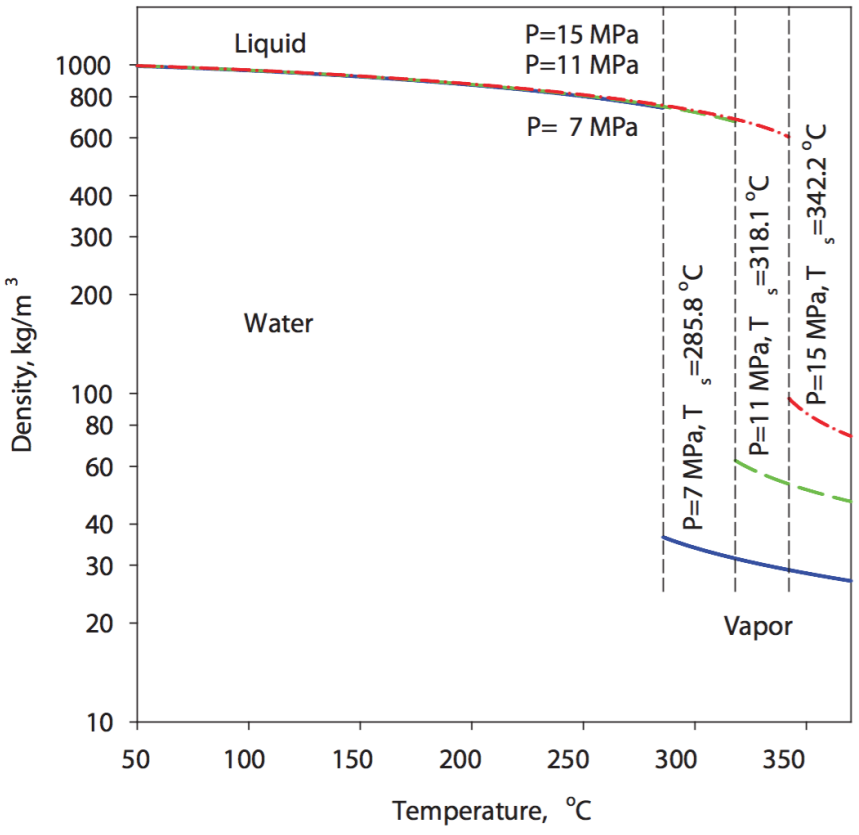

Figure 2-17. Density variations at subcritical pressure for water [34]

Variations in thermophysical properties are not exclusive to supercritical water. These trends are also evident in other supercritical fluids. Supercritical CO_2 is being investigated as a potential working fluid in the power cycles of some Gen IV nuclear reactor concepts such as the SFR, LFR and MSR, as well as some advanced air-conditioning and geothermal systems [35]. One of the benefits of using supercritical CO_2 is that its critical point is much lower than that of water; the critical point for CO_2 is 7.3773 MPa and 30.98°C [10]. A pressure vs. temperature diagram is shown in Figure 2-18.

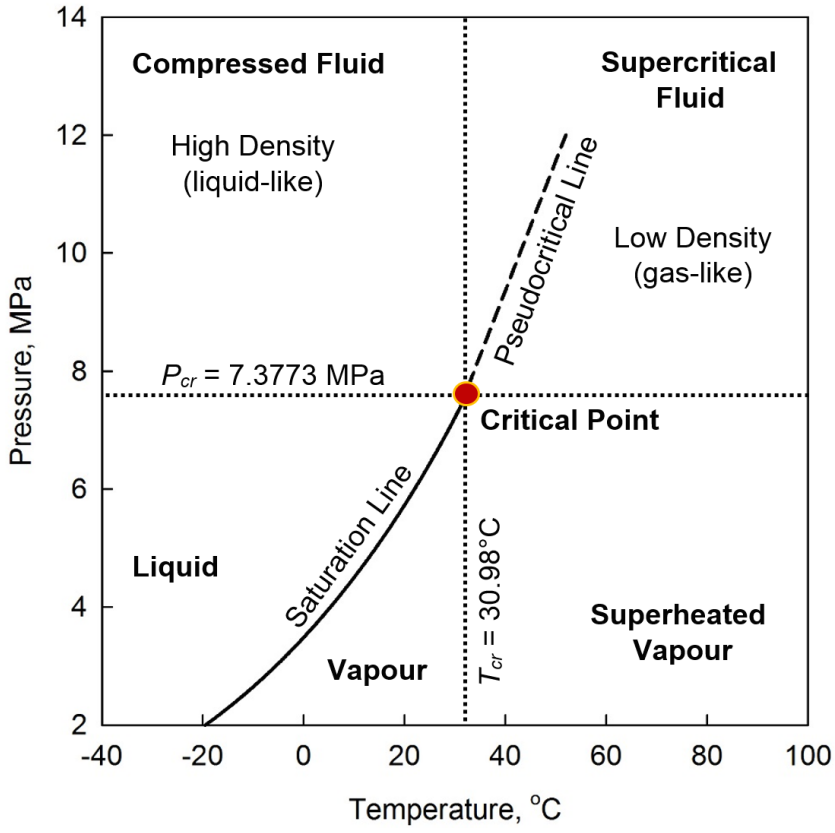

Figure 2-18. Pressure vs. temperature diagram for carbon dioxide

Several thermophysical property profiles for CO_2 have been developed. Similar to what was done for SCW in Figure 2-9 to Figure 2-16, the profiles for supercritical CO_2 were developed at critical pressure as well as two additional supercritical pressures. These two supercritical pressures were scaled down from the pressures shown in Figure 2-9 to Figure 2-16. The scaling technique used is shown in Equation 2-1 [36].

$$\left(\frac{P_b}{P_{cr}}\right)_{CO_2} = \left(\frac{P_b}{P_{cr}}\right)_{H_2O} \quad (2\text{-}1)$$

The thermophysical properties of supercritical CO_2 also experience significant variation within the critical and pseuocritical regions. As with the cases for water, the thermophysical properties for CO_2 were plotted for the critical pressure (P_{cr} = 7.3773 MPa) along with two supercritical pressures (8.36 MPa and 9.36 MPa). The trends shown in Figure 2-19 to Figure 2-26 are analogous to those shown in Figure 2-9 to Figure 2-16. These include significant drops in density and dynamic viscosity, a rapid increase in kinematic viscosity and specific enthalpy, as well as peaks in Prandtl number, specific heat, thermal conductivity and volume expansivity; all of which occur within the critical and pseudocritical regions.

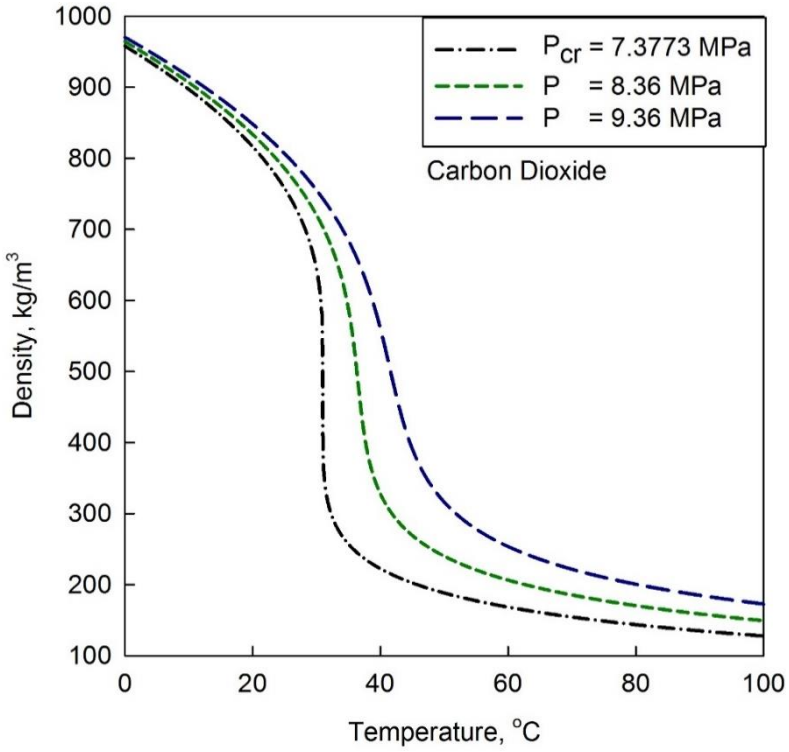

Figure 2-19. Carbon Dioxide: Density vs. temperature

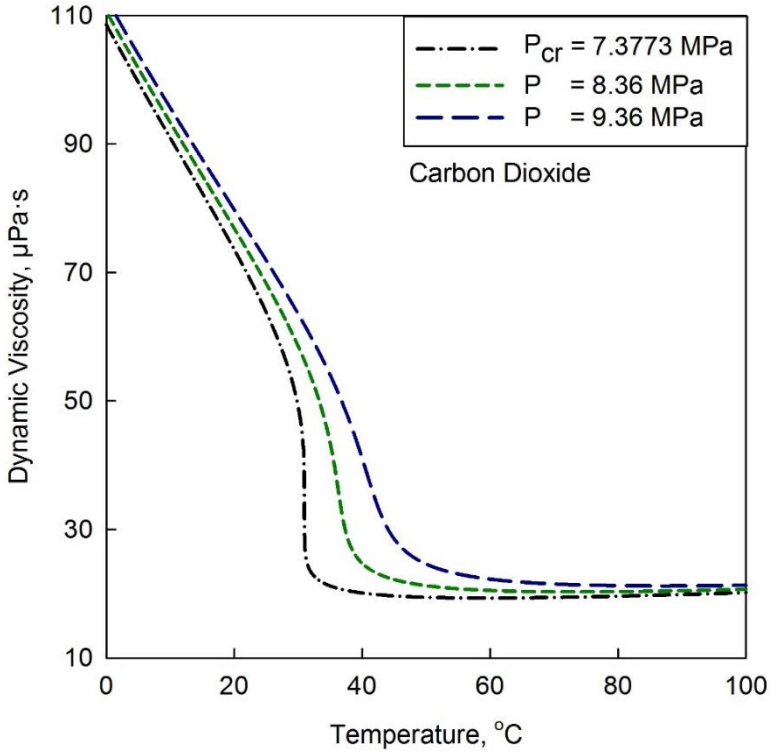

Figure 2-20. Carbon Dioxide: Dynamic viscosity vs. temperature

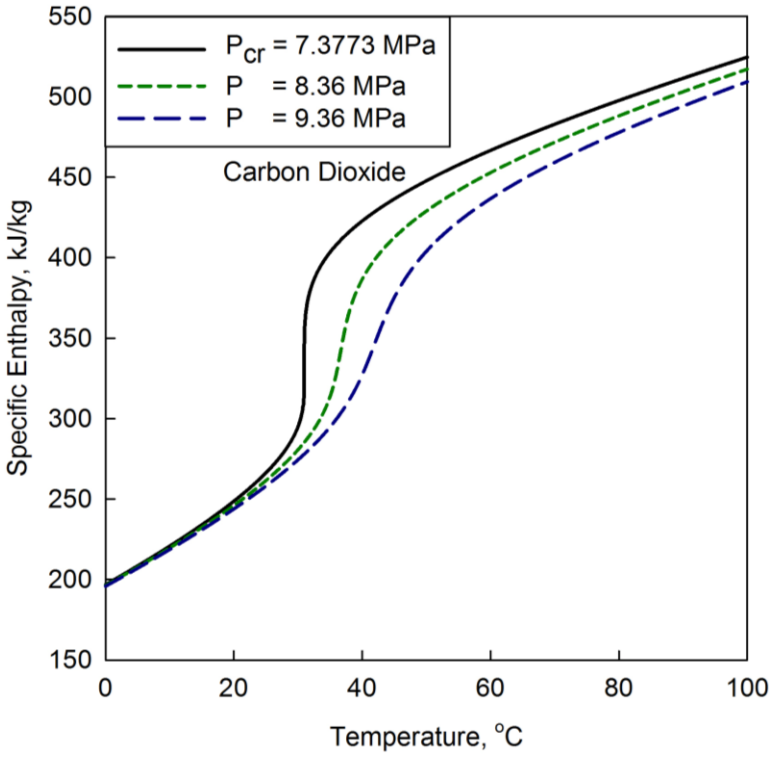

Figure 2-21. Carbon Dioxide: Specific enthalpy vs. temperature

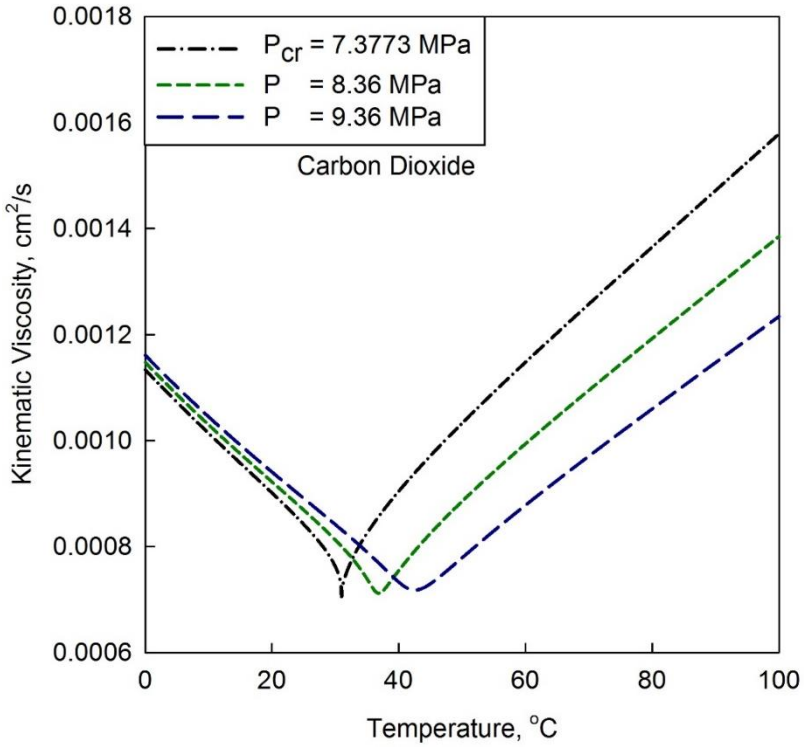

Figure 2-22. Carbon Dioxide: Kinematic viscosity vs. temperature

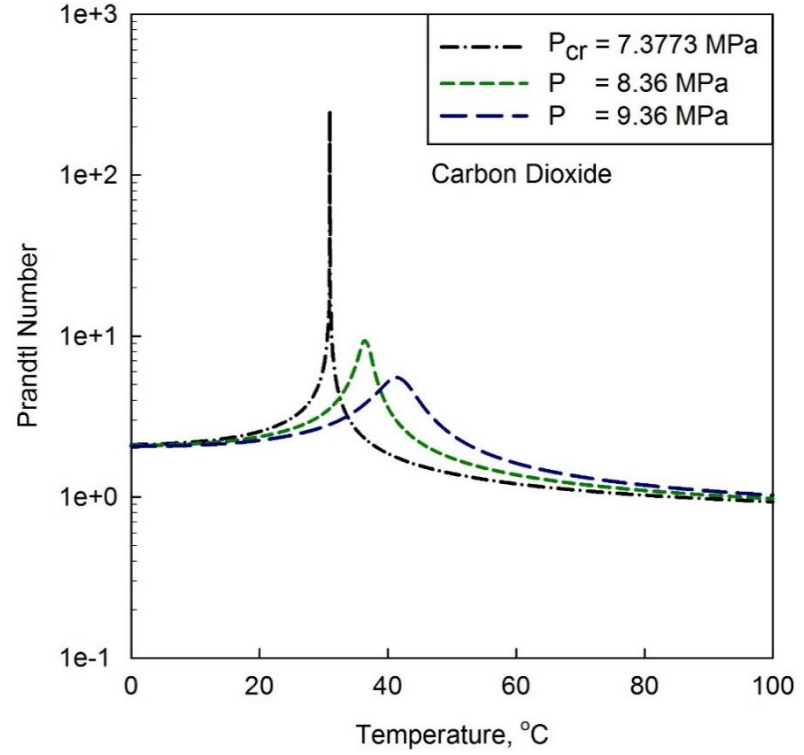

Figure 2-23. Carbon Dioxide: Prandtl number vs. temperature

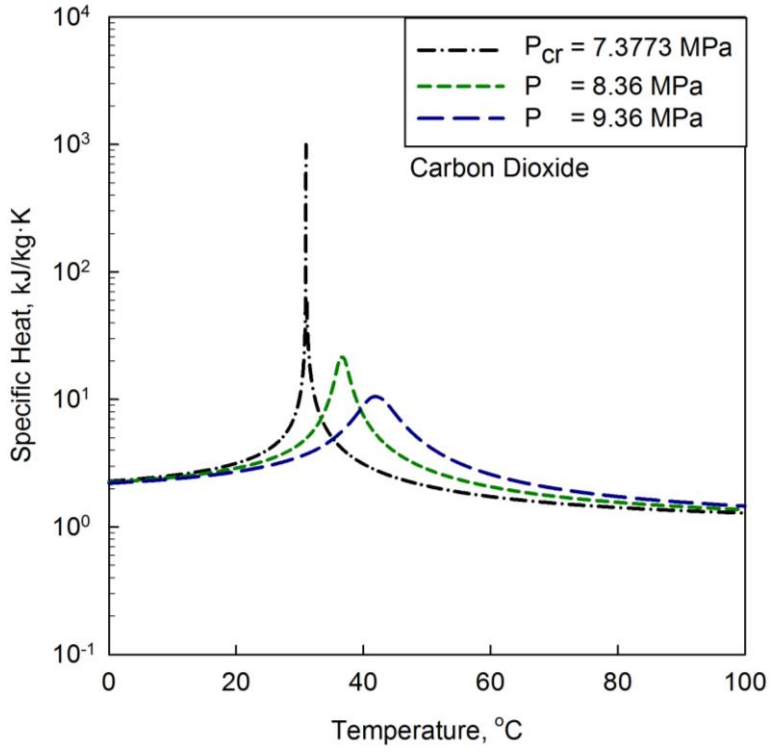

Figure 2-24. Carbon Dioxide: Specific heat vs. temperature

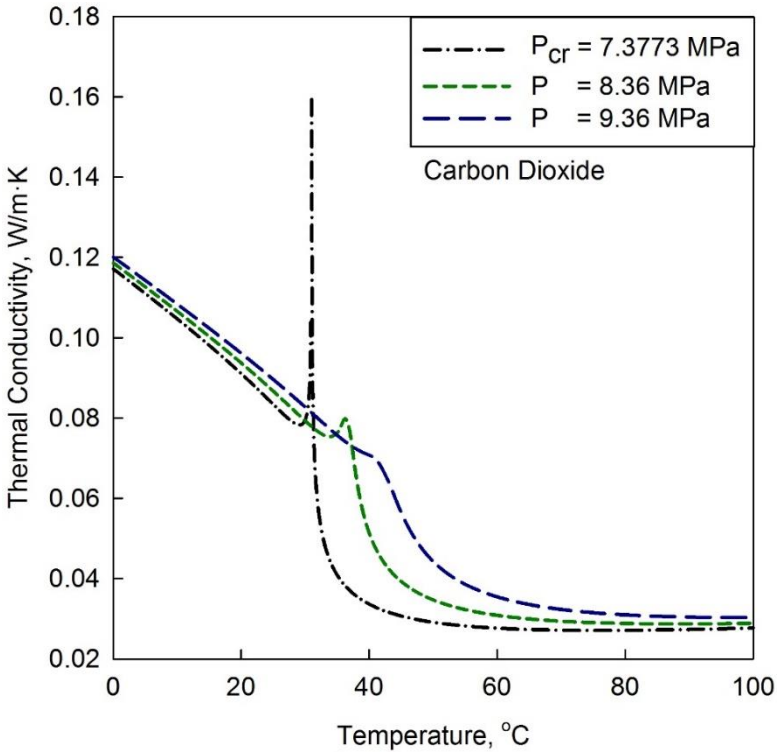

Figure 2-25. Carbon Dioxide: Thermal conductivity vs. temperature

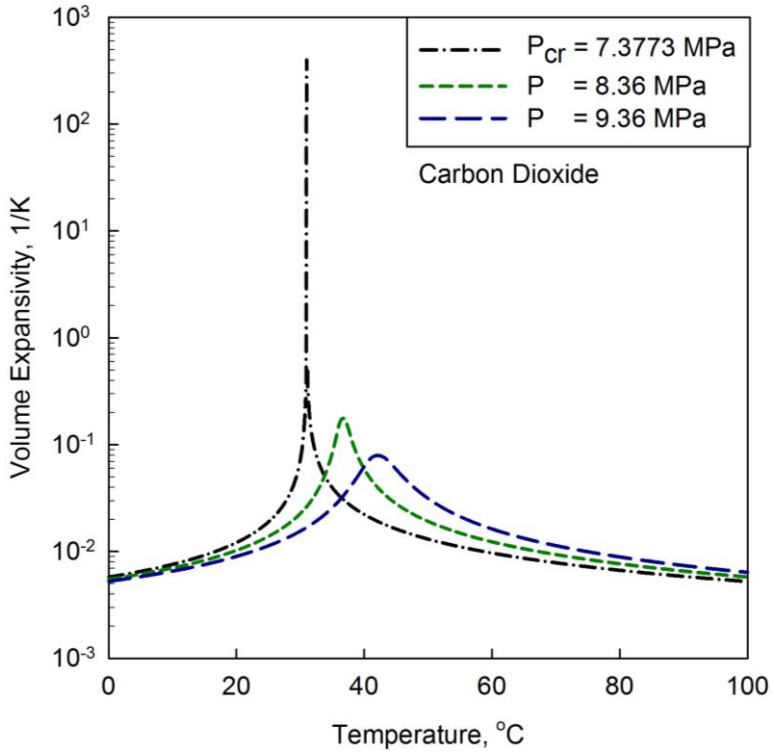

Figure 2-26. Carbon Dioxide: Volume expansivity vs. temperature

In this section the thermophysical properties of supercritical fluids have been reviewed. It is shown that there is a significant variation in these properties along the critical and pseuodcritical regions. Based on the requirements of the Cu-Cl cycle, the HX will need to operate at high temperatures. As a result, the HX designed in this work will incorporate supercritical working fluids. SCW will be directed from the reactor to the HX, where it will exchange heat with a secondary supercritical fluid. Supercritical fluids were selected for their positive impact on heat transfer due to higher HTCs at the near critical and supercritical ranges [6]. Due to their application in power production processes, the two supercritical fluids investigated here, SCW and supercritical CO_2, are under consideration for the HX.

Due to the significant variation in thermophysical properties, researchers have looked to develop several empirical heat transfer correlations in order to try and accurately predict the behaviour of supercritical fluids. These correlations are discussed in the following section.

2.4 Empirical Correlations for Supercritical Fluids

Ultimately, the goal of this work is to assess the performance of supercritical fluids in an intermediate HX that is to be used for the cogeneration of hydrogen. This will be done by performing a heat transfer analysis. In order to achieve this goal, the HTCs of the fluids used in the HX must be determined.

The most commonly used heat transfer correlation for forced convection at subcritical conditions is the Dittus-Boelter correlation, shown in Equation 2-2 [37].

$$\mathbf{Nu}_b = 0.0023\,\mathbf{Re}_b^{0.8}\,\mathbf{Pr}_b^{\mathrm{n}} \tag{2-2}$$

Where n = 0.4 for heating ($T_{su} > T_m$) and 0.3 for cooling ($T_{su} < T_m$). This correlation has been confirmed experimentally for the following conditions: $0.7 \leq \mathbf{Pr} \leq 160$, $\mathbf{Re} \geq 10000$ and $L/D \geq 10$. While, the Dittus-Boelter correlation has been primarily used for heat transfer calculations in a subcritical state, it was shown that this correlation showed good agreement with experimental data for SCW at 31 MPa flowing inside of circular tubes [38].

While the Dittus-Boelter correlation shown in Equation 2-2 can be used for fluids in supercritical conditions, this correlation is mostly used for heat transfer calculations at subcritical conditions. Accordingly, researchers have worked on the development of correlations specifically for supercritical fluids. The following sections will present correlations for SCW and supercritical CO_2.

Several empirical correlations based on experimental data have been developed to predict the HTC of supercritical fluids in forced convection. The correlations presented are based on data obtained from bare-tube experiments. While many of these correlations have been developed under similar conditions, the differences in HTC values obtained from these correlations can differ significantly, up to several hundred percent [6].

2.4.1 Correlations for Supercritical Water

Several correlations have been developed specifically for heat transfer in water at supercritical conditions. One such correlation is the Bishop et al. [39] correlation, shown in Equation 2-3.

$$\mathbf{Nu}_b = 0.0069\,\mathbf{Re}_b^{0.9}\,\overline{\mathbf{Pr}}_b^{0.66}\left(\frac{\rho_w}{\rho_b}\right)_x^{0.43}\left(1 + 2.4\frac{D}{x}\right) \tag{2-3}$$

Where x is the axial location along the heated length of the test section. The final term in the Bishop et al. correlation accounts for entrance region effects. This term is specific to the experimental setup used to retrieve the dataset. For this reason, this correlation is often used without this term, as shown in Equation 2-4.

$$\mathbf{Nu}_b = 0.0069\,\mathbf{Re}_b^{0.9}\,\overline{\mathbf{Pr}}_b^{0.66}\left(\frac{\rho_w}{\rho_b}\right)_x^{0.43} \tag{2-4}$$

The experimental dataset used to develop this correlation was obtained with operating pressures from 22.8 – 27.6 MPa, bulk-fluid temperatures from 282 - 527°C, mass flux values from 651 – 3662 kg/m²·s and heat flux values from 0.31 – 3.46 MW/m².

In 2009, Mokry et al. [40] developed a correlation based on the approach used by Bishop et al. This was done in an effort to develop a new correlation using updated water property tables. The Mokry et al. correlation is shown in Equation 2-5.

$$\mathbf{Nu}_b = 0.0061\,\mathbf{Re}_b^{0.904}\,\overline{\mathbf{Pr}}_b^{0.684}\left(\frac{\rho_w}{\rho_b}\right)_x^{0.564} \tag{2-5}$$

The experimental setup used to generate the dataset featured an operating pressure of 24 MPa, mass flux values from 200 – 1500 kg/m²·s, inlet temperatures from 320 - 350°C and heat flux values up to 1250 kW/m².

The correlations presented thus far have each been based on a bulk-fluid temperature approach. This means that the bulk-fluid temperature has been used to calculate the **Re** and **Pr** number; however, other researchers have suggested using an alternative approach, which is based on wall temperatures. This means that wall temperatures will be used to calculate both the **Re** and **Pr** number. Swenson et al. [41] developed such a correlation, as shown in Equation 2-6.

$$\mathbf{Nu}_w = 0.00459\,\mathbf{Re}_w^{0.923}\,\overline{\mathbf{Pr}}_w^{0.613}\left(\frac{\rho_w}{\rho_b}\right)_x^{0.231} \tag{2-6}$$

The experimental dataset used to develop this correlation was obtained using pressures from 22.8 MPa – 41.4 MPa, bulk-fluid temperatures from 75 – 576°C, wall temperatures from 93 – 649°C and mass flux values from 542 – 2150 kg/m²·s.

In 2010, researchers from the University of Ottawa compared many of the existing empirical correlations. The accuracies of these correlations were compared against an experimental dataset provided by Kirillov et al. at the Institute of Physics and Power Engineering. It was determined that the Mokry et al. correlation was the most accurate in the supercritical, near-supercritical and superheated steam regions [42].

For this reason, the Mokry et al. correlation will be used for the analysis in this work. Based on the scope of this work, a comparison of all the correlations shown is presented in Appendix C.

2.4.2 Correlations for Supercritical Carbon Dioxide

The Gupta et al. [43] correlation for supercritical CO_2 is based on the approach used by Swenson et al., as such the majority of the thermophysical properties used were based on wall temperatures. This correlation is shown in Equation 2-7.

$$\mathbf{Nu}_w = 0.004\,\mathbf{Re}_w^{0.923}\,\overline{\mathbf{Pr}}_w^{0.773}\left(\frac{\mu_w}{\mu_b}\right)_x^{0.366}\left(\frac{\rho_w}{\rho_b}\right)_x^{0.186} \tag{2-7}$$

2.5 Types of Heat Exchangers

The process of exchanging heat between two fluids at different temperatures separated by a solid wall occurs in many engineering applications. The equipment that is used for this process is a HX. There are many different kinds of HX, which are typically classified according to flow arrangement and type of construction.

Two common flow arrangements for HXs are the parallel-flow and counter-flow arrangements. In a parallel-flow arrangement, two fluids will enter the HX on the same side, flow in the same direction and the two fluids will then exit the HX from the same end. It is important to note that in this arrangement the outlet temperature of the cold fluid can never exceed the outlet temperature of the hot fluid [37].

In a counter-flow arrangement, two fluids will enter the HX on opposite sides and flow in opposite directions, thus leaving the HX at opposite ends. Therefore, the temperature difference between the two fluids at the inlet of the HX is not as large as it in a parallel-flow HX. Unlike a parallel-flow arrangement, however, HXs utilizing a counter-flow arrangement allow for heat transfer between the hotter portions of the two fluids at one end, as well as between the colder portions of the fluids at the other end. As a result, the outlet temperature of the cold fluid may now exceed the outlet temperature of the hot fluid [37].

Although there are several types of HXs, two of the most common types of HXs are double-pipe HXs and shell-and-tube HXs.

2.5.1 Double-pipe Heat Exchangers

A double-pipe HX consists of one pipe placed concentrically inside another pipe of a larger diameter. The double-pipe sections can be connected in either series or parallel arrangements. Double-pipe HXs are more suited towards applications wherein strict counter-flow is required due to a large temperature cross, for high-pressure applications and in cases where parallel units would need to be added or removed due to changes in operating practice or for maintenance purposes [44]. A simplified schematic of a counter-flow double-pipe HX is shown in Figure 2-27.

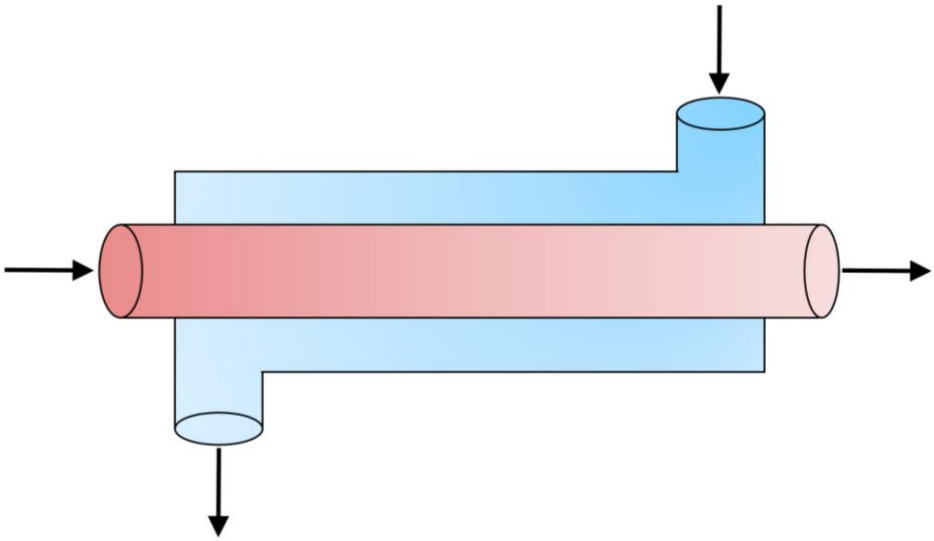

Figure 2-27. Schematic of a double-pipe heat exchanger

2.5.2 Shell-and-tube Heat Exchangers

Shell-and-tube HXs are the most commonly used basic HX configuration in process industries. There are various forms for this type of HX but the simplest involves a single tube and shell pass. A simplified schematic of a single tube and shell pass HX is shown in Figure 2-28. Baffles can be installed in shell-and-tube HXs to increase the

HTC of the shell side fluid as they will introduce turbulence to the fluid. Shell-and-tube HXs have a fairly high heat transfer area to volume and weight ratio and are relatively easy to construct in wide range of sizes [37, 44].

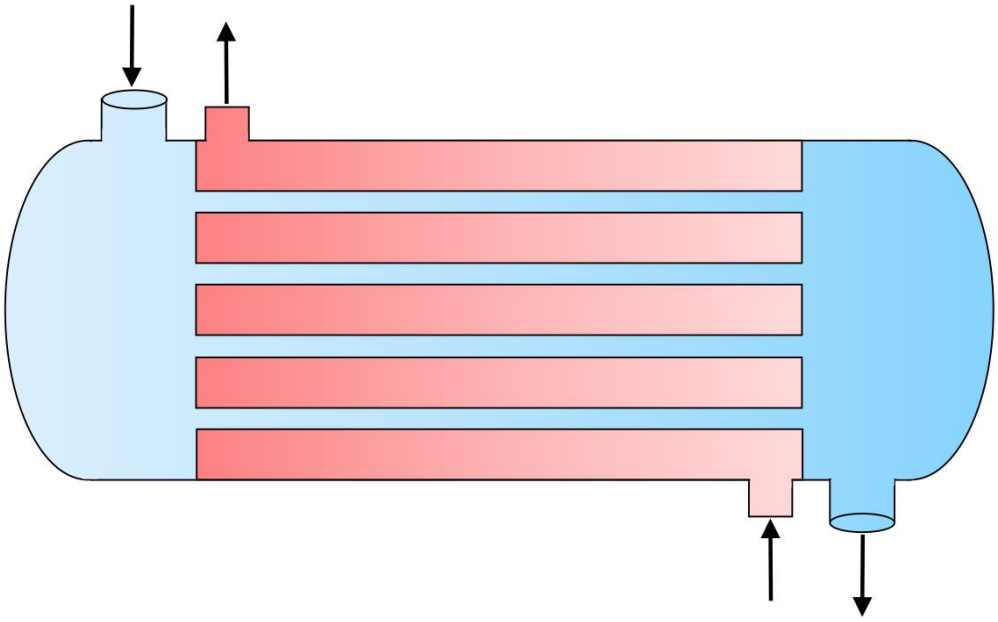

Figure 2-28. Schematic of a shell-and-tube heat exchanger

Chapter 3. Methodology

This chapter outlines the methodology used to complete the heat transfer analysis in this work. This analysis was conducted to meet the stated objective in Section 1.3, which is to assess the performance of the supercritical fluids in an intermediate HX. This is done by simulating the heat transfer between two supercritical fluids in an intermediate HX. This simulation is performed using a one-dimensional numerical model. The script for this numerical model is presented in Appendix A: MATLAB Script.

The methodology presented in this chapter is broken down into several steps. The thermal energy requirement is established in Section 3.1. This section describes the thermal energy requirement that the intermediate HX will need to satisfy in order to produce hydrogen at a rate of 1 kg/s. Conceptual design requirements for an intermediate HX are described. The requirements were developed in order to facilitate the development of a conceptual HX design. The design requirements are presented in Section 3.2. Based on the design requirements, a conceptual HX design is chosen in Section 3.3. This section defines the type of HX that is to be modelled, as well as the flow arrangement for the HX. This section also defines the operating conditions and specifications of the HX, which will serve as inputs into the numerical model. Additionally, safety considerations for the HX are also detailed in this section.

The final section of this chapter, Section 3.4, describes the heat transfer analysis that was conducted. The reference cases used as inputs for the numerical model are defined. The numerical model and theory used to simulate the heat transfer between the supercritical fluids is also detailed.

3.1 Thermal Energy Requirement for Hydrogen Production

Prior to the development of a conceptual HX design, the thermal energy requirement for hydrogen production must be established. In Section 2.1, it is shown that for a commercial-scale production rate of 1 kg/s, the thermal energy requirement for the 4-step Cu-Cl cycle is 224 MW_{th}. The Canadian SCWR based on a no-reheat cycle has a thermal power of 2540 MW_{th}. Therefore, approximately 8.8% of the total reactor thermal power would need to be diverted to meet a production rate of 1 kg/s.

The thermal energy requirement is dependent on the production rate that is set by a hydrogen production facility and is not fixed by any means; however, a thermal energy requirement of 224 MW_{th} is used as an input throughout all simulations in this work. This value is used in conjunction with the minimum temperature requirement of 530°C, as defined in Section 2.1, to determine the size of the HX.

The thermal energy requirement and minimum temperature requirement described in this section were used to define the operating conditions and specifications of a conceptual HX design. These operating conditions and specifications will serve as inputs into the numerical model. This is further explained in Section 3.4.2, where the numerical model used for the simulations is described.

3.2 Conceptual Design Requirements

Design requirements for a conceptual HX design to be used for the cogeneration of hydrogen are as follows:

1. The HX should be capable of transferring the necessary heat for hydrogen production via the 4-step Cu-Cl cycle to take place.

In order for the HX to be used to facilitate the cogeneration of hydrogen, it should be capable of transferring the required heat from the reactor coolant to the intermediate

working fluid of the HX. This requirement will be verified through a heat transfer analysis. The results obtained from this analysis are presented in Chapter 4.

2. The pipes used in the HX must be capable of withstanding high operating pressures and temperatures.

As stated earlier, the HX will be designed to operate with the use of supercritical fluids as the main working fluids. Therefore the material and dimensions of said material must be selected such that they are able to withstand these operating conditions.

3. The HX should be able to accept changes to the total flow rate within the HX.

A percentage of the coolant will be diverted from the reactor outlet towards the HX. If more coolant is diverted, more heat can be exchanged and if less coolant is diverted, less heat will be exchanged. The amount of coolant that is diverted will depend on the production requirements set by the hydrogen production facility. Therefore, depending on these requirements, the HX should be able to accommodate changes in the amount of coolant that is to be diverted from the reactor.

The stated design requirements will be used as the basis for a conceptual HX design that is to be used for hydrogen production.

3.3 Conceptual Heat Exchanger Design

Based on the stated design requirements, a counter-flow double-pipe HX was selected. While double-pipe HXs do not have a good heat transfer area to volume and weight ratio, they do provide other positives for this specific application. This is demonstrated by meeting the design requirements that were previously established.

As stated in Section 3.2, the first design requirement will be verified through the results from the heat transfer analysis, which is presented in Chapter 4. The second

design requirement states that the HX must be capable of withstanding high operating pressures. This requirement was set in place due to the expected operating conditions of the HX. The critical pressure of water and carbon dioxide are 22.064 MPa and 7.3773 MPa, respectively. Therefore, since this work assesses the performance of supercritical fluids, the HX will need to be able to operate at these elevated pressures. Double-pipe HXs are well-suited for high pressure applications with one of the benefits for using a double-pipe HX is the added safety under high pressures. Additionally, they are also more suited towards applications wherein a large temperature cross is required. This added benefit will aid in ensuring the desired temperature change occurs within the HX.

The third design requirement states that the HX should be capable of accepting changes to total flow rates within the HX. Double-pipe HX designs benefit from the ability to add and/or remove parallel units. This allows for the size of a HX to be adjusted based on the hydrogen production requirement. If more pipes are required to transfer more energy from the reactor to the hydrogen production facility, parallel units can be added to a double-pipe HX much easier than that of shell-and-tube HX. For these reasons a double-pipe HX was selected for analysis. Analyses on shell-and-tube HXs can be conducted as a part of future research efforts to determine their viability.

The working fluids for the conceptual design of an intermediate HX are the coolant from the reactor and an intermediate working fluid. Two intermediate working fluids are selected for analysis: (1) SCW and (2) supercritical CO_2. The SCW-to-SCW HX will be referred to as HX-1 and the SCW-to-supercritical CO_2 will be referred to as HX-2.

Both HX-1 and HX-2 will feature the aforementioned double-pipe design. In both HXs, the SCW reactor coolant will flow through the inner pipe and the intermediate working fluid will flow through the annulus between the inner and outer pipe. Since

the reactor coolant is the heat source in the HX, it is considered the hot fluid in this scenario. Therefore, the inner pipe, where the hot fluid is flowing, is referred to as the hot side. The intermediate working fluid in the annulus is the colder of the two fluids and is considered as the cold fluid. Since the cold fluid is flowing through the annulus, this is referred to as the cold side.

A reference diagram for HX flow arrangement is shown in Figure 3-1. The reactor coolant is labelled as 'Hot Side' and coloured in red. The intermediate working fluid in the annulus is coloured in blue and is labelled as the 'Cold Side'. A counter-flow flow-arrangement is shown using the arrows on the diagram. The label '*Q*' and the associated arrows are used to show the direction of heat transfer from the hot side to the cold side.

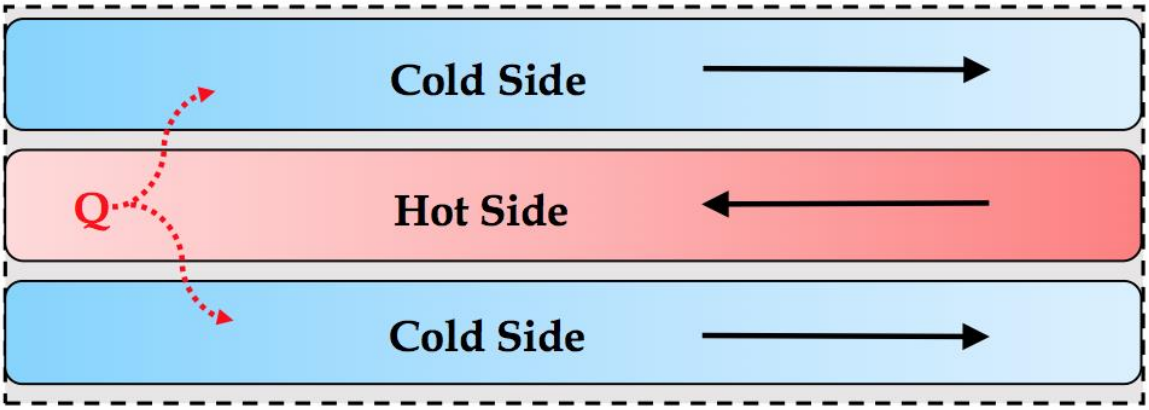

Figure 3-1. Reference diagram for HX flow arrangement

The HX type and flow arrangement have now been defined. It was shown how the chosen configuration will meet the established design requirements. The following sections will define the operating conditions, materials and piping specifications of the conceptual HX design.

3.3.1 Operating Conditions of Intermediate HX

The operating conditions for the hot side and cold side of the HX are determined by the temperature requirements of the 4-step Cu-Cl and by the operating conditions of the reactor coolant. It was stated that both HX-1 and HX-2 will use the reactor coolant as the working fluid on the hot side. Canadian SCWRs operate at a pressure of 25 MPa with reactor outlet temperatures of 625°C. The heat extraction point was selected as the outlet of the reactor, therefore, the inlet temperature of the hot side of the HX is 625°C. The outlet temperature of the hot side is determined such that an equal amount of energy is transferred between the two fluids. As such, the outlet temperature of the hot side is a case-dependent variable that is determined in the numerical model. This is done in order to preserve an energy balance between the two fluids. The heat lost by the hot side must be equal to the heat gained by the cold side, which is dependent on the operating conditions of the fluids. This is further described in Section 3.4.

An inlet temperature of 350°C was selected for the cold side. In order to achieve the inlet temperature that has been selected, preheaters would be required. Surveyed literature suggests that preheaters can comfortably achieve this value [45]. Additionally, if a lower inlet temperature is selected, the size of the HX will increase, as it will increase the desired temperature change. Therefore, an inlet temperature of 350°C was chosen to balance the load on both the preheaters and intermediate HX. The outlet temperature of the cold side was selected in accordance with the temperature requirements of the Cu-Cl cycle. In Section 2.1, it was shown that the maximum temperature requirement for the 4-step Cu-Cl cycle is 530°C. Therefore, the intermediate working fluid on the cold side would need to achieve this temperature before exiting the HX. For this reason, an outlet temperature of 530°C was selected for the cold side.

The pressure of the hot side for both HX-1 and HX-2 are 25 MPa as this is the pressure of the reactor coolant at the outlet of the reactor. The pressure of the cold side is different for each HX. The intermediate working fluid on the cold side of HX-1 is SCW. The reference pressure of the cold side for HX-1 was selected as 25.5 MPa, which is well above the critical pressure of water and is slightly higher than the 25 MPa of the hot side. The reason for this selection is that in the event of a leak in the inner pipe, the intermediate working fluid on the cold side would flow into the inner pipe, which will contain the reactor coolant on the hot side.

Unlike HX-1, HX-2 will utilize supercritical CO_2 as the intermediate working fluid on the cold side of the HX. The purpose behind studying supercritical CO_2 in addition to SCW relates to the critical point of the fluid. Supercritical CO_2 has a much lower critical point than SCW. The critical pressure of supercritical CO_2 is 7.3773 MPa, as compared to the 22.064 MPa of SCW. Therefore, the pressure of the cold side can be significantly reduced while still maintaining the fluid in a supercritical state. Therefore, the pressure of the cold side was set to 8.53 MPa, which was scaled down from the 25.5 MPa pressure in HX-1. The pressure was scaled down using Equation 2-1, as shown in Section 2.3.

The mass flux chosen for both the hot side and the cold side of HX-1 and HX-2 was 1000 kg/m^2·s. This value was selected based on the bounds of the **Nu** number correlations. Heat transfer correlations, more specifically **Nu** number correlations, for supercritical fluids were presented in Section 2.4. In this section it was stated that the Mokry et al. correlation would be used in the heat transfer analysis. The empirical dataset used to develop the Mokry et al. correlation incorporated mass fluxes from a range of 250 kg/m^2·s to 1500 kg/m^2·s. Therefore, the correlation is more suitable for calculations within this range. For this reason, the mass flux for both the hot side and the cold side of both HX-1 and HX-2 were set to 1000 kg/m^2·s. This also allows a margin on both the lower and upper bounds for several sensitivity analyses. The results from these sensitivity analyses are shown in Chapter 4.

The operating conditions for the fluids in HX-1 and HX-2 are summarized in Table 3-1 and Table 3-2, respectively. The working fluids, pressures, temperatures and mass flux for the hot side and cold side of each HX are listed in these tables. It is shown that while most of the parameters are fixed, the outlet temperature of the hot side is a variable. A more detailed discussion on the parameters for each of the individual test cases are presented in the following chapter.

Table 3-1. Fluid parameters for HX-1 (SCW-to-SCW)

Parameters	**Hot Side**	**Cold Side**
Fluid	SCW	SCW
Pressure (MPa)	25	25.5
Inlet Temperature (°C)	625	350
Outlet Temperature (°C)	To be calculated	530
Mass Flux (kg/m^2·s)	1000	1000

Table 3-2. Fluid parameters for HX-2 (SCW-to-supercritical CO_2)

Parameters	**Hot Side (Reactor Coolant)**	**Cold Side (HX Working Fluid)**
Fluid	SCW	Supercritical CO_2
Pressure (MPa)	25	8.53
Inlet Temperature (°C)	625	350
Outlet Temperature (°C)	To be calculated	530
Mass Flux (kg/m^2·s)	1000	1000

3.3.2 Material Selection and Piping Dimensions

With a conceptual HX type, flow-arrangement and operating conditions established, the materials and piping dimensions were selected. Research into material selection for HXs utilizing SCW was conducted by Thind in 2012 [45]. Inconel-600, Inconel-718, Inconel-800, Stainless Steel 304 (SS-304) and Zirconium were investigated. It was shown that the thermal conductivity of Inconel-600, Inconel-718, Inconel-800 and SS-304 increased linearly with an increase in temperature, while the thermal conductivity of Zirconium only begins to increase from temperatures of 300°C and greater. This comparison is shown in Figure 3-2 [45].

Figure 3-2 shows that Inconel-600, SS-304 and Zirconium outperform Inconel-718 and Inconel-800 in terms of thermal conductivity. While Zirconium does show good results for thermal conductivity, the material does not perform well at temperatures above 300°C due to elevated corrosion rates. The Ultimate Tensile Strength (UTS) of the material also drops significantly at higher temperatures [46].

The melting point for SS-304 and Inconel-600 are 1400 - 1455°C and 1354 - 1413°C, respectively [47]. Since the maximum temperature in the HX is 625°C at the inlet of the hot side, which is where the reactor coolant will enter the HX, the melting point for either material is not an issue. The UTS of Inconel-600 and SS-304 decrease as the temperature of the material increases. At 650°C, the UTS of Inconel-600 is approximately 450 MPa, while the UTS of SS-304 is 305 MPa [47, 48]. Due to its widespread use in HX applications, SS-304 was selected as the material of choice for this work. Investigations into the use of other material choices can be completed as a part of future research efforts.

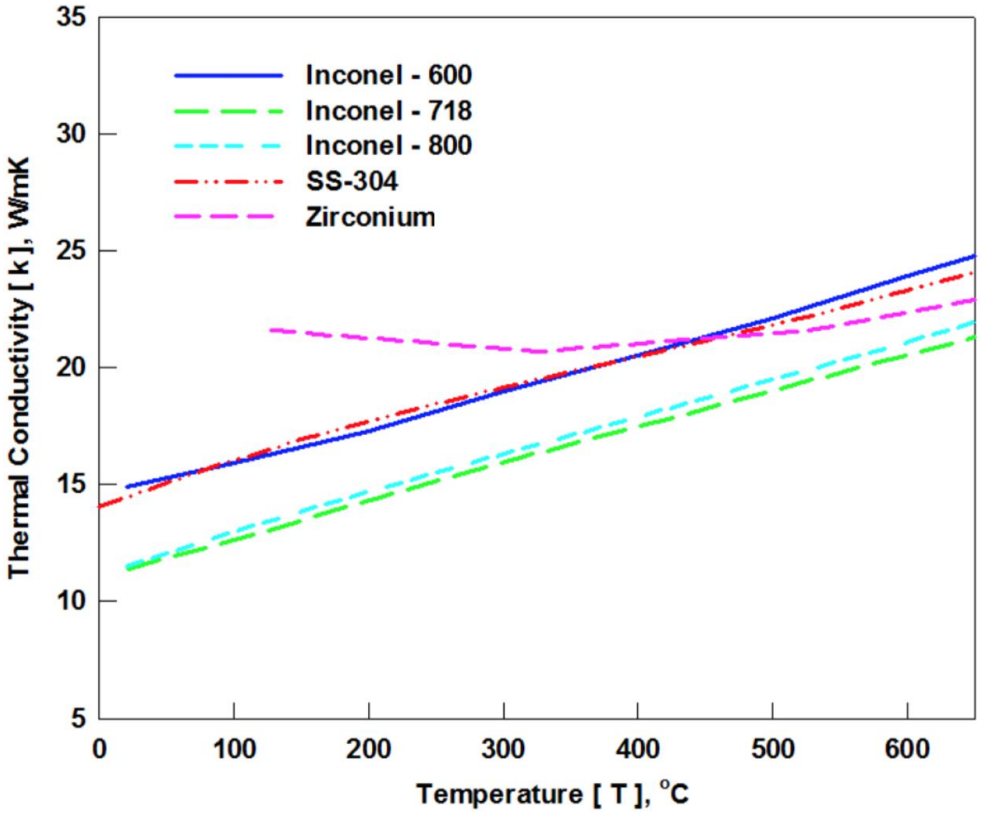

Figure 3-2. Thermal conductivity vs. temperature for various materials [45]

The second design requirement stated that the pipes used in the HX must be capable of withstanding high operating pressures and temperatures. ASME standards require the stress of the pressure boundary component be less than one-third of the UTS of the material. Therefore, in order to comply with this ASME standard, wall thicknesses for the pipes must be chosen accordingly.

The applicable ASME standard requires that the stress of the pressure boundary component be less than one-third of the UTS of the material. While the maximum temperature inside the HX will be 625°C, the UTS of SS-304 was conservatively taken at 650°C, as the UTS is lower at higher temperatures. The UTS of SS-304 at this temperature is 305 MPa. The minimum thickness of the pipes was determined calculated using Equation 3-1, shown on below:

$$\delta = \frac{P \cdot D}{2 \cdot S} \tag{3-1}$$

Where δ is the minimum required thickness, P is the pressure of the system, D is the inner diameter of the pipe and S is 1/3 of the UTS of the material, which in this case is SS-304.

Piping diameters and thicknesses were selected such that they adhere to standard Nominal Pipe Size (NPS) dimensions. To determine the dimensions of the pipes, an inner diameter was first selected. The minimum wall thickness needed to adhere to the aforementioned ASME standard was then calculated using Equation 3-1. With the inner diameter and wall thickness selected, the outer diameter of the pipes was determined using Equations 3-2 and 3-3.

$$d_o = d_i + 2\delta_d \tag{3-2}$$

$$D_o = D_i + 2\delta_D \tag{3-3}$$

The inner pipe and outer pipe diameters are shown using lower and upper case nomenclature, respectively; Equations 3-2 and 3-3 demonstrate this relationship. A cross-sectional view of the HX piping is shown in Figure 3-3.

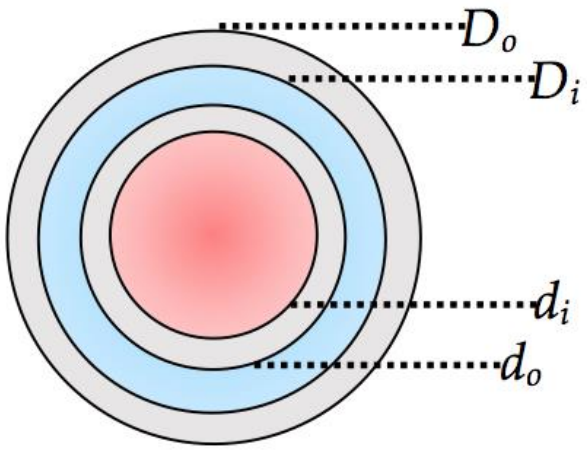

Figure 3-3. Cross-section of double-pipe heat exchanger

These calculations were performed as hand calculations which would serve as inputs to the numerical model. These hand calculations were performed so that pipe dimensions would conform to Schedule 40 or Schedule 80 pipe sizing standards.

The piping dimensions that were determined by the hand calculations are listed in Table 3-3. There are three sets of piping dimensions for inner pipe to go along with two sets of piping dimensions for the outer pipe. Several combinations of the listed dimensions were used to determine the impact of piping diameters and thicknesses on the overall size of the HX. Results are presented in Chapter 4.

It should be noted that the piping dimensions listed in Table 3-3 were used for both HX-1 and HX-2. This was done to assess the performance of the supercritical fluids, regardless of remaining design aspects.

Table 3-3. Piping Dimensions used in HX Analysis

Inner Pipe		**Outer Pipe**	
Outer Diameter, d_o (mm)	**Wall Thickness, δ_d (mm)**	**Outer Diameter, D_o (mm)**	**Wall Thickness, δ_D (mm)**
26.7	2.9	42.2	4.9
26.7	3.9	48.3	5.1
33.4	3.4	-	-

3.3.3 Safety Considerations

Richards et al. [49] investigated the use of modular helium reactor for hydrogen cogeneration. The reactor would link to a hydrogen facility based on the S-I cycle. It was suggested that a distance of approximately 100 – 150 m should separate the NPP and the hydrogen production facility. Ultimately, the distance between these two facilities will largely depend on regulatory and safety concerns. Heat losses will also play a significant role in determining distance between the two facilities. While heat losses are not considered in this work, it still important to mitigate these losses. One of the benefits of placing the hot fluid in the inner pipe of the HX is that this will reduce the amount of heat that is lost to the external environment.

The coolant from the reactor will be diverted from the reactor to an intermediate HX. Since the coolant must pass through the reactor core before being diverted towards the HX, there is a possibility that the coolant could contain radioactive impurities. This possibility is further increased in an accident scenario. This can raise safety concerns with radioactive material breaching containment as it is travelling towards the HX. Therefore, the intermediate HX will be need to be placed within the containment facility of the reactor. By placing the HX within the containment building, the probability of releasing radioactive material through the coolant, is greatly reduced.

3.4 Heat Transfer Analysis

In order to meet the stated objective of this thesis, a heat transfer analysis was conducted. The analysis was performed by a one-dimensional numerical model developed in MATLAB. The numerical model simulates the heat transfer between two supercritical fluids in an intermediate double-pipe HX.

3.4.1 Reference Cases for HX-1 and HX-2

Reference cases for HX-1 and HX-2 were developed based on the conceptual design detailed in Section 3.3. A summary of the operating parameters for the reference cases of HX-1 and HX-2 are listed in Table 3-4 and Table 3-5, respectively. The parameters listed in Table 3-4 and Table 3-5 summarize the inputs from the conceptual design of the HX that were used in the numerical model to conduct the simulations.

The outlet temperature of the hot side is not listed in either table as it is not an input in the numerical model, rather it is a case-dependent variable that is calculated during each test case, including the reference cases.

In addition to the two reference cases discussed here, several test cases were conducted as part of a sensitivity analysis. This was done to determine how the operating parameters can impact the overall size of the HX. These test cases included sensitivity analyses on mass flux, pressure and piping diameters; the results are discussed in detail in Chapter 4.

Table 3-4. Operating parameters for reference case counter-flow double-pipe HX-1

Operating Parameter	**Inner Pipe (Hot Side)**	**Annulus Gap (Cold Side)**
Fluid	SCW	SCW
Pressure (MPa)	25	25.5
Inlet temp. (^{o}C)	625	350
Outlet temp. (^{o}C)	-	530
Mass flux (kg/m^2·s)	1000	1000
Inner diameter (mm)	20.9	32.5
Outer diameter (mm)	26.7	42.2
Wall thickness (mm)	2.87	5.80

Table 3-5. Operating parameters for reference case counter-flow double-pipe HX-2

Operating Parameter	**Inner Pipe (Hot Side)**	**Annulus Gap (Cold Side)**
Fluid	SCW	Supercritical CO_2
Pressure (MPa)	25	8.53
Inlet temp. (^{o}C)	625	350
Outlet temp. (^{o}C)	-	530
Mass flux (kg/m^2·s)	1000	1000
Inner diameter (mm)	20.9	32.5
Outer diameter (mm)	26.7	42.2
Wall thickness (mm)	2.87	5.80

3.4.2 Numerical Model

A numerical model was developed in MATLAB. The inputs for the numerical model are summarized in Table 3-4 and Table 3-5. The numerical model simulates the heat transfer that is occurring within the HX. By doing this, the overall size of the HX can be predicted based on the inputs into the model. The size of the HX is determined such that it will meet the thermal energy requirement that was established in Section 3.1, as well as meet the minimum temperature requirement of the cold side. The HX is considered to be a steady-flow device at steady operating conditions such that the mass flow rate of each fluid remains constant throughout the HX.

The numerical model is comprised of four main components. These components are used to complete the heat transfer analysis; the four components of the numerical model are listed below:

1. Determine the total number of pipes required to meet the thermal energy requirement.
2. Approximate the length of the pipes in the HX using a linear temperature profile.
3. Determine the actual temperature profile of the fluids along the length of the HX.
4. Calculate the thermophysical properties and heat transfer coefficients of the fluids along the length of the HX, based on the actual temperature profiles.

In the first component of the numerical model, the total number of pipes required to meet the thermal energy requirement of 224 MW_{th} are determined. This was done by first determining the amount of energy being transferred in one pipe. The desired temperature change in the cold side is known for both HX-1 and HX-2, therefore the amount of energy being transferred in a single pipe can be evaluated. It was assumed that the outer surface of the HX is perfectly insulated. Heat losses to the surrounding

environment were not considered and heat transfer is only occurring between the two fluids. Therefore, once the rate of heat transfer of a single pipe was calculated, the total number of pipes required can be determined using the 224 MW_{th} thermal energy requirement.

The second component of the numerical model approximates the pipe lengths of the HX. This approximation was completed using the assumption of a linear temperature profile. This assumption adds uncertainty to the pipe lengths of the HX. The objective of this thesis is not to make an accurate sizing prediction, rather it is to assess the performance of supercritical fluids. In this assessment, it is more important to assess the how the size of the HX responds to changes in the operating conditions of fluids, not to determine the actual size of the HX. Therefore, this uncertainty was deemed acceptable.

The third component of the numerical model determines the actual temperature profile of the fluids along the length of the HX, using the pipe lengths determined in the previous component of the model. The temperature is calculated in 10 cm increments. After several initial trials, a 10 cm increment was chosen as there was no measurable increase in accuracy when moving to a smaller increment size. The computational time simply increased. It is assumed that the temperature of the fluids remain constant in each of these nodes. The temperature profiles are determined in 10 cm increments because of the significant variation in the thermophysical properties within the pseudocritical region; these properties are determined in the fourth component of the numerical model.

The actual temperature profiles are determined using iterations based on the expected enthalpy change of the fluid across the node. It additionally assumed that the enthalpy change is constant throughout the length of the HX. In order to validate the assumptions made in determining the temperature profiles, the results were compared against open literature. These results are further discussed in Chapter 4.

The fourth component of the numerical model was used to calculate the thermophysical properties of the fluids based on the actual temperature profiles of the fluids in the HX. The thermophysical properties of the fluids were obtained from NIST REFPROP using the temperature and pressure of the fluids at each node. Thermophysical properties were determined at both bulk-fluid and wall temperatures. The bulk-fluid properties were obtained using the temperature profiles determined in the third component of the numerical model. The wall-fluid properties were obtained using an initial estimate for wall temperature. At each node, the wall temperature was assumed to be 5°C below the hot side bulk-fluid temperature. Once all of the thermophysical properties were obtained, the HTC of the fluids and thermal resistances were evaluated along the length of the HX. Using the thermal resistances, the wall temperatures at each node are calculated. The initial estimate for wall temperatures was then verified. This was done in an iterative process until the initial estimate for wall temperature and the calculated wall temperature are in agreement within a ±0.3°C difference.

All of the components of the numerical model described in this section were completed using MATLAB. The MATLAB script of the numerical model is shown in Appendix A. This MATLAB script was independently peer reviewed by Ph.D. student Amjad Farah.

3.4.3 Modelled Equations

This section describes the equations that were modelled in the numerical model to conduct the heat transfer analysis. To begin, the rate of heat transfer in the pipes was calculated; this was done using Equation 3-4. Since the desired temperature change of the cold side is defined as an input in the numerical model, the change in enthalpy of the cold side is also known. Therefore, the rate of heat transfer of the cold side can be determined.

$$\dot{Q}_{cs} = \dot{m}_{cs}\Delta H_{cs} \quad (3\text{-}4)$$

Using the rate of heat transfer from Equation 3-4, the outlet temperature of the hot side can be determined by rearranging Equation 3-5.

$$\dot{Q}_{hs} = \dot{m}_{hs}\Delta H_{hs} \quad (3\text{-}5)$$

Where the subscripts *hs* and *cs* denote the hot side and cold side, respectively.

It is assumed that there is no heat loss to the environment. Therefore, Equations 3-4 and 3-5 must show that the thermal energy loss on the hot side is equal to the thermal energy gain on the cold side. Therefore, using the heat transfer rate from the cold side, the hot side outlet temperature was calculated.

The total number of pipes is determined using the heat transfer rate from Equations 3-4 and 3-5. Once the heat transfer rate in a single pipe is determined, the total number of pipes required can be determined using the previously established thermal energy requirement of 224 MW_{th}.

As shown in Equations 3-4 and 3-5, the total rate of heat transfer is dependent on the mass flow rate in the pipe. Using mass flux and cross-sectional area as an input, the mass flow rate of a pipe is determined using Equation 3-6.

$$\dot{m} = GA_C \quad (3\text{-}6)$$

Where G is the mass flux of the fluid and A_c is the cross-sectional area. Therefore, since the mass flow rate is not a fixed value and is dependent on the selected mass flux and cross-sectional area in a test case, the hot side outlet temperature is not used as an input into the numerical model. These calculations summarize the first component of the numerical model.

The second component of the numerical model was used to estimate the pipe lengths of the HX. Analyses of HXs are typically performed utilizing one of two methods.

Ultimately, this choice is dependent on the desired outcome of the analysis. Selecting a HX can be done to either achieve a specified temperature change in a fluid stream of a known mass flow rate, or to predict outlet temperatures of the hot and cold fluid streams based on a specified HX. The Log Mean Temperature Difference (LMTD) method is better suited towards the first task, while the Effectiveness-NTU method is typically employed for the latter. This work is focused on achieving a specified temperature change and as a result the LMTD was the methodology selected. This methodology served to determine the pipe lengths of the HX.

In using the LMTD method, the logarithmic temperature difference between the two fluids across the HX is determined using Equation 3-7 [37].

$$\Delta T_{lm} = \frac{\Delta T_1 - \Delta T_2}{ln\left(\frac{\Delta T_1}{\Delta T_2}\right)} \tag{3-7}$$

Where,

$$\Delta T_1 = T_{hs,in} - T_{cs,out} \tag{3-8}$$

$$\Delta T_2 = T_{hs,out} - T_{cs,in} \tag{3-9}$$

Using Equation 3-7, the rate of heat transfer in a HX can be expressed in analogous manner to Newton's law of cooling through Equation 3-10 [37].

$$\dot{Q} = U A_s \Delta T_{lm} \tag{3-10}$$

Where U is the overall HTC, A_s is the heat transfer surface area and ΔT_{lm} is the LMTD. Since the rate of heat transfer, $\dot{Q}$, is known and the LMTD can be determined using Equation 3-7, Equation 3-10 can be rearranged to determine the heat transfer surface area, A_s. Once the heat transfer surface area is calculated, the pipe lengths required to achieve the desired temperature change can be determined.

Of all the parameters shown in Equation 3-10, the only remaining unknown is U. In order to calculate U, the thermal resistances of the fluids and pipe wall must first be determined.

To start, the non-dimensional numbers **Re** and average $\overline{\mathbf{Pr}}$ need to be calculated. These non-dimensional numbers are used to calculate the **Nu** of the hot side and cold side, as shown in Section 2.4. The **Re** number is calculated for the hot side and cold side using Equation 3-11 and 3-12, respectively [37].

$$\mathbf{Re}_{b,hs} = \frac{G_{hs} d_i}{\mu_{b,hs}} \tag{3-11}$$

$$\mathbf{Re}_{b,cs} = \frac{G_{cs} D_{hy}}{\mu_{b,cs}} \tag{3-12}$$

Where D_{hy} is the hydraulic diameter and μ_b is the dynamic viscosity of the fluid taken at its bulk temperature. The dynamic viscosity is taken from NIST REFPROP. The hydraulic diameter is used to apply an effective diameter to noncircular tubes and is calculated using Equation 3-13.

$$D_{hy} = \frac{4A_c}{p_{wetted}} \tag{3-13}$$

Where p_{wetted} is the wetted perimeter of the pipe. The hydraulic diameter for an annulus is shown in Equation 3-14, which further simplifies to Equation 3-15.

$$D_{hy} = \frac{4\left(\frac{\pi}{4}\right)\left(D_i^2 - d_o^2\right)}{\pi(D_i + d_o)} \tag{3-14}$$

$$D_{hy} = D_i - d_o \tag{3-15}$$

Now that the equations for determining the **Re** number have been defined, the equations to determine the average $\overline{\mathbf{Pr}}$ are discussed. In order to determine the average $\overline{\mathbf{Pr}}$, the average specific heat, $\overline{C_p}$, must be determined; this is shown in Equation 3-16.

$$\overline{C_p} = \frac{H_w - H_b}{T_w - T_b} \tag{3-16}$$

Where H_w is the enthalpy of the fluid based on wall temperature, T_w, and H_b is the enthalpy of the fluid based on its bulk temperature, T_b. The wall temperature and corresponding enthalpy are determined using an initial estimate, as described in Section 3.4.2. This initial estimate is that wall temperature is assumed to be 5°C less than the bulk-fluid temperature of the hot side at each node.

The average $\overline{\mathbf{Pr}}$ number is calculated using Equation 3-17.

$$\overline{\mathbf{Pr}}_b = \frac{\mu_b \overline{C_p}}{k_b} \tag{3-17}$$

Once the **Re** number and average $\overline{\mathbf{Pr}}$ number have been calculated, the **Nu** number can be calculated using the equations presented in Section 2.4. The HTC of the hot side and the cold side can then be determined using Equations 3-18 and 3-19, respectively.

$$HTC_{hs} = \frac{\boldsymbol{Nu}_{b,hs} k_{b,hs}}{d_i} \tag{3-18}$$

$$HTC_{cs} = \frac{\boldsymbol{Nu}_{b,cs} k_{b,cs}}{D_{hy}} \tag{3-19}$$

Where k_b is the thermal conductivity of the fluid. The HTCs shown in Equations 3-18 and 3-19 can be used to determine the thermal resistances, R, of the hot side and the cold side; the corresponding equations are shown in Equation 3-20 and 3-21 [50].

$$R_{hs} = \frac{d_o}{HTC_{hs} d_i} \tag{3-20}$$

$$R_{cs} = \frac{1}{HTC_{cs}} \tag{3-21}$$

In addition to calculating the thermal resistances of the fluids, the thermal resistance of the pipe must also calculated using Equation 3-22.

$$R_{pipe} = \frac{d_o \ln\left(\frac{d_o}{d_i}\right)}{2k_{pipe}} \tag{3-22}$$

Where k_{pipe} is the thermal conductivity of the pipe. The material selected in this work is SS-304; the thermal conductivity for SS-304 is determined using Equation 3-23 [37].

$$k_{pipe} = 2 \cdot 10^{-8} T_w^3 - 4 \cdot 10^{-5} T_w^2 + 3.98 \cdot 10^{-2} T_w + 5.728 \tag{3-23}$$

The overall HTC is determined using Equation 3-24.

$$\frac{1}{U} = R_h + R_{pipe} + R_c \tag{3-24}$$

U can then be substituted into Equation 3-10 to estimate the length of the pipes for the HX, thus completing the second component of the numerical model.

It was stated earlier that wall-fluid properties were determined using an initial estimate for wall temperature. Using Equation 3-25 by Shah and Sekulic [50], this initial estimate can be verified as described in Section 3.4.2.

$$T_w = \frac{\left(\frac{T_{b,hs}}{R_{hs}}\right) + \left(\frac{T_{b,cs}}{R_{cs}}\right)}{\left(\frac{1}{R_{hs}}\right) + \left(\frac{1}{R_{cs}}\right)} \tag{3-25}$$

The third component of the numerical model computed the actual temperature profiles using the expected enthalpy change of the fluid across the length of the HX. The incremental enthalpy change was determined by dividing the total enthalpy change of the fluid, based on the inlet and outlet temperatures, along the length of the pipes determined in the second component.

The fourth component of the numerical model calculates the actual thermophysical properties and HTCs of the hot side and the cold side. The process for these calculations involved using Equations 3-11 to 3-25, as was done in the second component of the numerical model. The reason for this being that the second component of the numerical model used a linear temperature profile assumption. As

a result, the thermophysical properties would need to be recalculated to capture the physics within the HX based on the actual temperature profiles, which were obtained in the third component. The average U based on the linear temperature profiles and actual temperature profiles were compared during initial trials. It was determined that the error in the average U from this assumption was less than 1%.

Chapter 4. Results and Analysis

The analysis performed in this work is divided into two main parts. The two main parts are distinguished by the types of fluids used in the HX. As described in Chapter 3, two intermediate working fluids were considered in this work: (1) SCW and (2) supercritical CO_2. The first part of the heat transfer analysis dealt with the SCW-to-SCW HX, referred to as HX-1. The second part dealt with the SCW-to-supercritical CO_2 HX, referred to as HX-2.

For each HX, a simulation was conducted on a reference case and a heat transfer analysis was performed. Heat transfer analyses were also performed on multiple test cases, which incorporated a sensitivity analyses of various parameters. These test cases varied fluid parameters such as pressure and mass flux to determine the impact on the overall size of the HX. Test cases were also conducted to determine the impact of varying piping dimensions.

For each of these test cases a thermal energy requirement of 224 MW_{th} and a cold side outlet temperature requirement of 530^{o}C were selected, as described in Section 3.1.

4.1 HX-1: SCW-to-SCW

An initial reference case as well as ten additional test cases were developed to assess the impact of various parameters on the size of HX-1.

4.1.1 Reference Case

The operating parameters used in this reference case are listed in Table 3-4 in Section 3.4.1.

A mass flux of 1000 kg/m^2·s was used for both the hot side and the cold side. The mass flow rates per pipe and total mass flow rate were determined using these mass flux values. The total mass flow rate of the hot side is 168 kg/s. This is approximately 12% of the total mass flow rate in the current Canadian SCWR concept. This is the percentage of the Canadian SCWRs flow rate that would need to be diverted for the production of hydrogen. Ultimately, this value is dependent on the desired production rate; the production rate chosen in this work is 1 kg/s. By decreasing this requirement, the percentage of reactor coolant required by the system would also decrease. Similarly, by increasing the requirement, the percentage of reactor coolant required by the system would also increase.

The results from the reference case are shown in Figure 4-1. The results show that a total of 488 pipes with a length of 19.9 m would be required to produce hydrogen at the desired rate of 1 kg/s. This amounts to a total heat transfer area of 812 m^2.

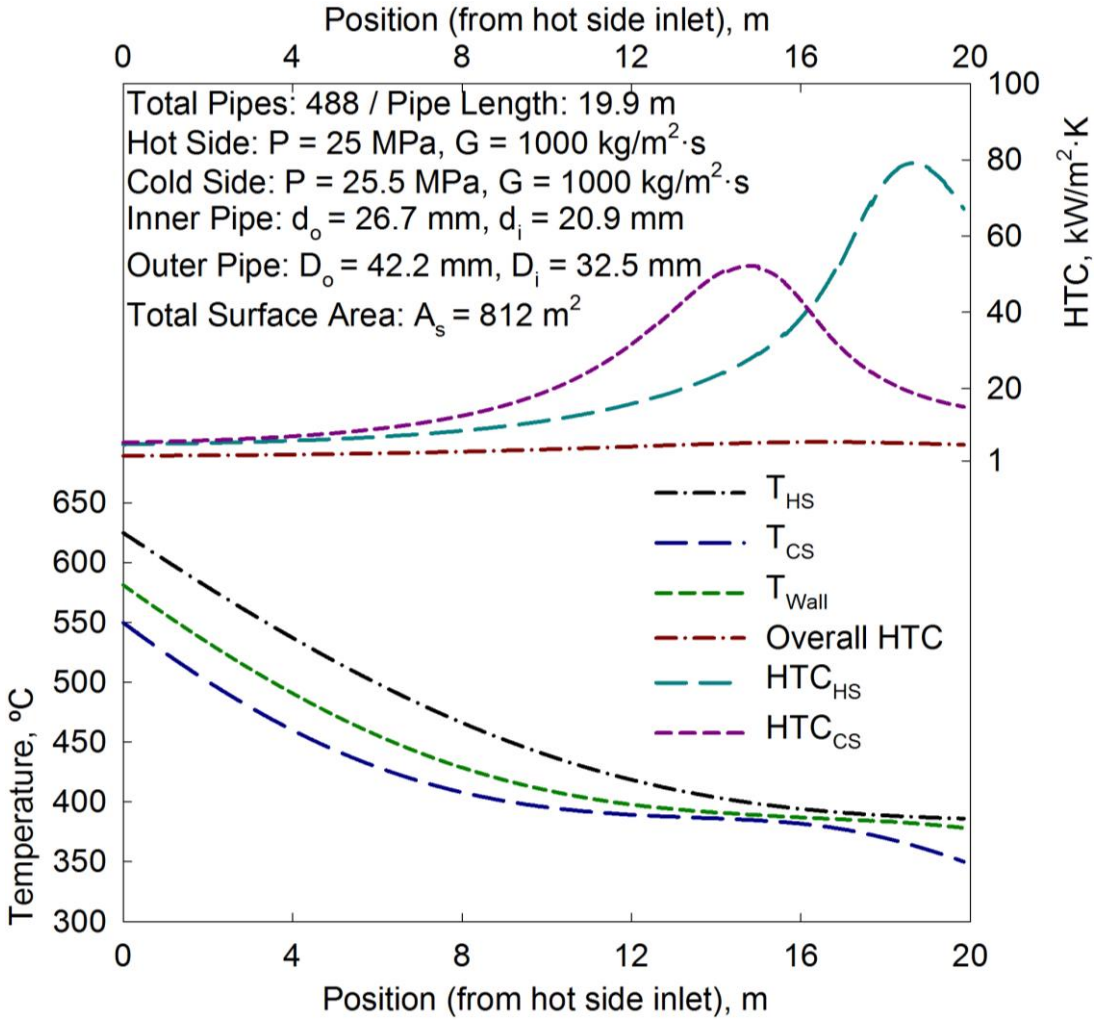

Figure 4-1. Reference Case for HX-1: Hot side, cold side and wall temperatures vs. position. Local and overall HTC vs. position.

The results from Figure 4-1 show that the hot side and the cold side enter the pseudocritical region while in the HX. This is evidenced by the variation in the HTC of the two fluids. This variation is to be expected within the pseudocritical region. Supercritical fluids experience a peak in the specific heat indicating the location of the pseudocritical point. At approximately 12 m from the hot side inlet, the temperature profiles begin to exhibit a 'pinching' effect. The difference in temperature between the hot side and the cold side profiles decreases and the profiles 'pinch' each other. To validate the temperature profiles, the results were compared against openly available literature. The surveyed literature showed that the temperature profiles for supercritical fluids experience a 'pinching' effect as shown in Figure 4-1. This is attributed to the peak in specific heat while the fluid is operating in the pseudocritical region. This is also evidenced by flattening temperature profiles. When the temperature profiles begin to 'pinch' one another, they also flatten out. This is reflective of the peak in specific heat where due to this peak more energy is required to increase the temperature of the fluid.

The profiles for the thermal conductivity and specific heat for both the hot and cold side along the length of the HX are shown in Figure 4-2. Additional thermophysical properties are shown in Figure B-1 in Appendix B. It is evident that both properties undergo significant variation within the pseudocritical region. The thermal conductivity of the cold side experiences a local peak at the pseudocritical point. While a peak in specific heat for the cold side is shown, a peak for the hot side is not. This occurs because the outlet temperature of the hot side is 386^{o}C. The pseudocritical temperature for water at 25 MPa is 384.5^{o}C. Therefore, while the fluid on the hot side does operate in the pseudocritical region, it does not reach the pseudocritical point.

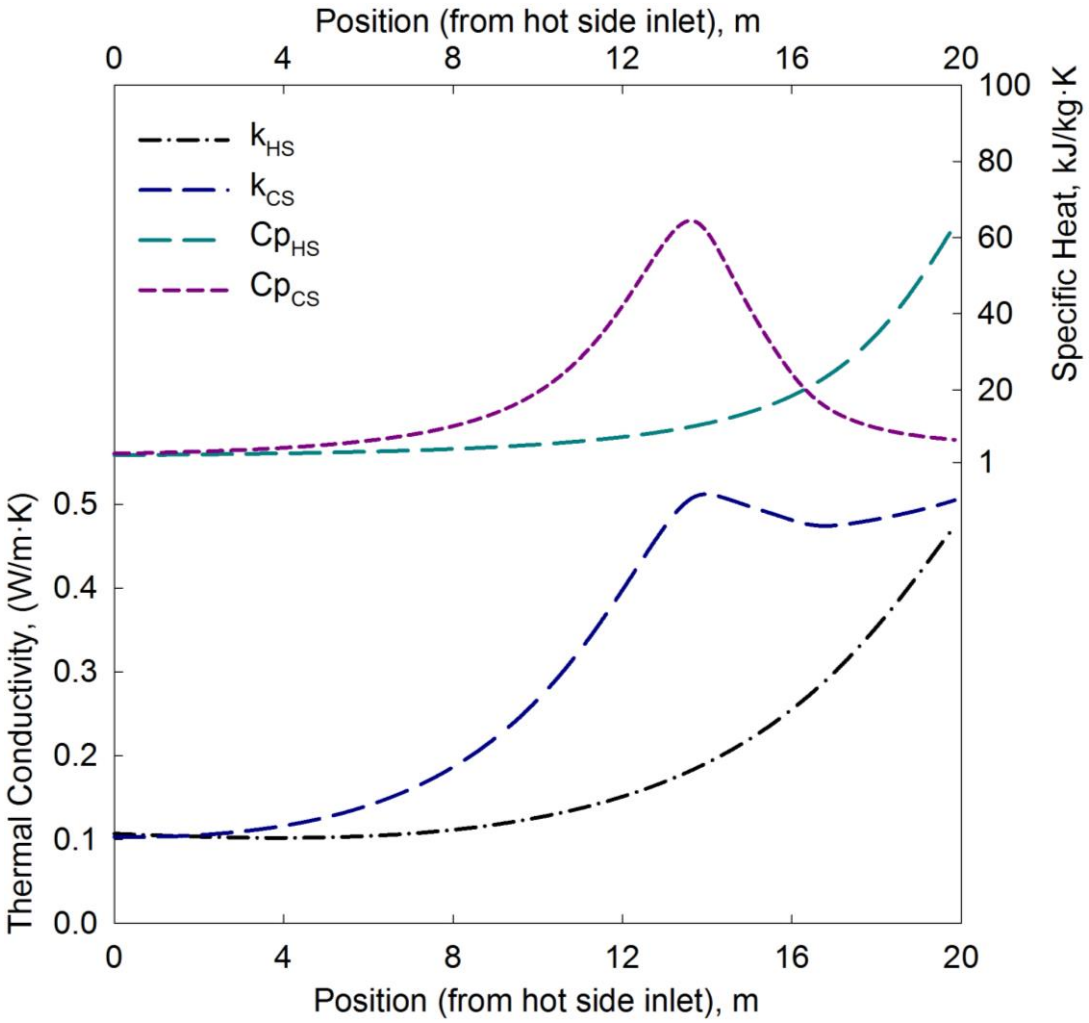

Figure 4-2. Reference Case for HX-1: Hot side and cold side thermal conductivity vs. position. Specific heat vs. position.

The average specific heat and HTC of the two fluids are shown in Figure 4-3. The average specific heat is the ratio of the difference between the enthalpies of the fluid at wall temperature and bulk temperature to the difference in the fluids wall and bulk temperature. As shown in Figure 4-1, the fluid wall temperature is different than that of the bulk-fluid temperature. In the case of the hot side, the temperature of the fluid at the wall is several degrees lower than that of the bulk temperature. For the cold side, the temperature of the fluid at wall is higher than that of the bulk temperature. Therefore, when determining the average specific heat as described above and shown in Equation 3-16, the location of this peak will shift as compared to a non-averaged specific heat. The Mokry et al. correlation, which is used to determine the **Nu** number, utilizes the average $\overline{\mathbf{Pr}}$ number. The average $\overline{\mathbf{Pr}}$ number is determined using the average specific heat as shown in Equation 3-17. Therefore the variation in the local HTCs shown in Figure 4-1 and Figure 4-3, culminating in moderately pronounced peaks, can be attributed to the peaks in the average specific heat.

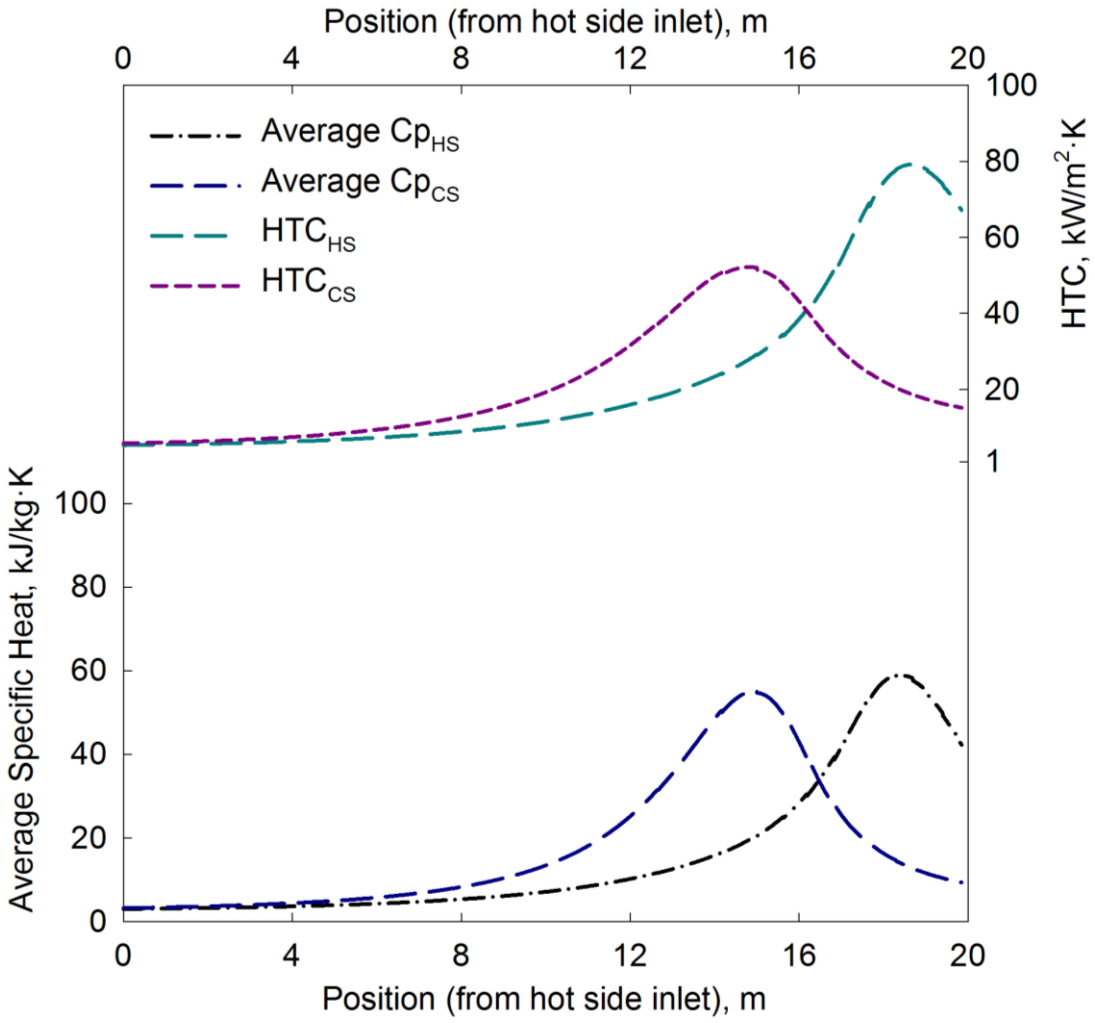

Figure 4-3. Reference Case for HX-1: Hot side and cold side average specific heat vs position. Local HTC vs position.

4.1.2 Sensitivity Analysis: Mass Flux

The impact of mass flux was assessed. To study the impact of this parameter, several combinations of mass flux values were chosen. This was done while maintaining all of the other parameters from the reference case the same. Initially, the mass flux of the hot side is kept constant at 1000 kg/m^2·s, while the mass flux of the cold side is varied. The mass flux was varied from 500 to 1250 kg/m^2·s in increments of 250 kg/m^2·s, excluding 1000 kg/m^2·s, as this was done as the reference case. The results from these test cases are shown in Figure 4-4, Figure 4-5 and Figure 4-6. In test case #1, when the mass flux for the cold side is 500 kg/m^2·s, the resultant number of pipes required was 975 with a length of 10.5 m per pipe. At 750 kg/m^2·s in test case #2, the resultant number of pipes required was 650 with a length of 14.3 m per pipe. Finally, in test case #3 shown in Figure 4-6, when the mass flux of the cold side is 1250 kg/m^2·s, the piping requirements became a total of 390 pipes with a length of 31.5 m per pipe.

It is evident that varying the mass flux on the cold side has an impact on the overall size of the HX. When the mass flux is reduced, the pipe length decreases but the number of pipes required to transfer the same amount of heat increases. Similarly, if the mass flux is increased, the pipe length increases but the number of pipes required decreases. The reason for this is that the mass flux has a direct impact on the amount of heat being transferred in a pipe. The mass flow rate of a fluid is proportional to its mass flux. As per Equations 3-4 and 3-5, the amount of heat lost by the hot side and gained by the cold side is directly proportional to the mass flow rate of the two fluids. Therefore, since the inlet and outlet temperatures of the cold side are fixed, the amount of heat being transferred to the cold side must change when the mass flux is changed.

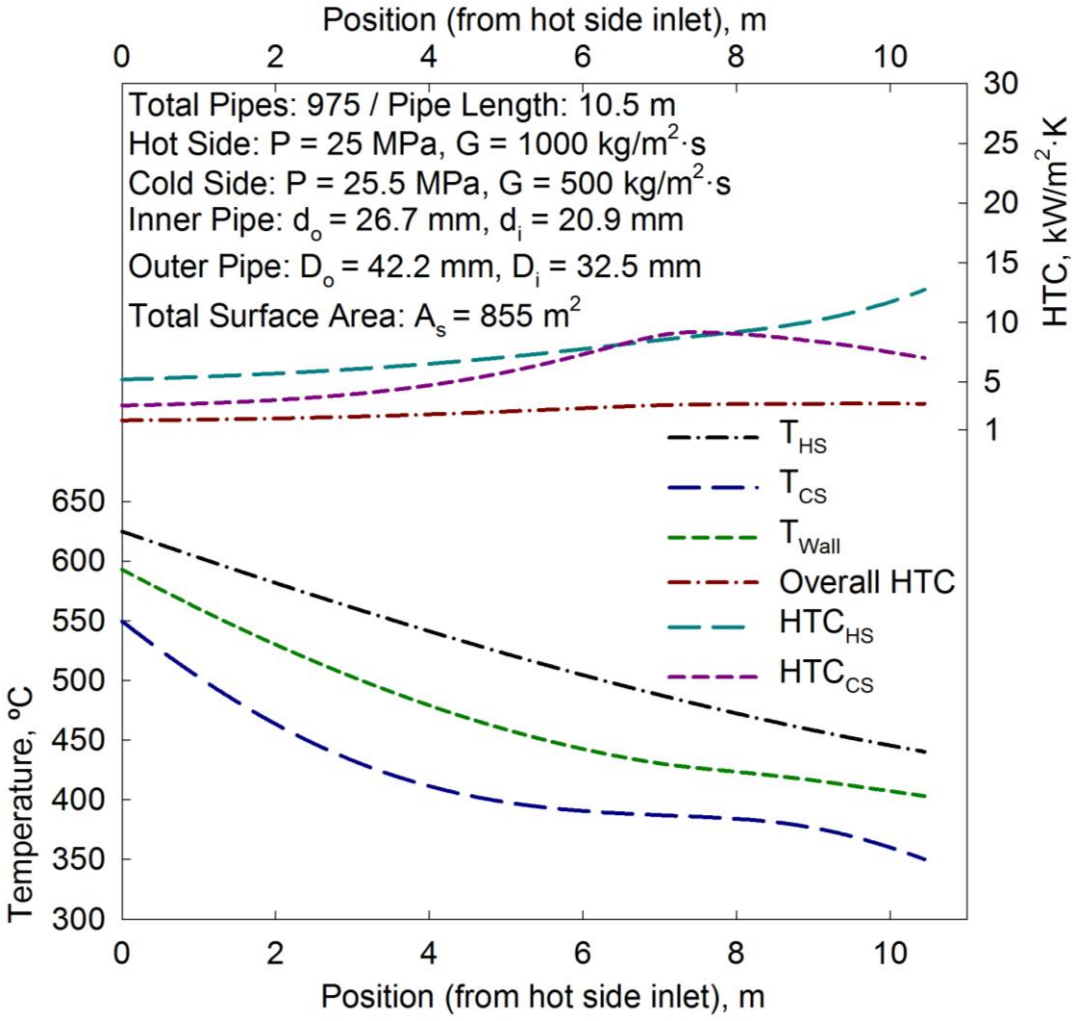

Figure 4-4. Test case #1 for HX-1: G_{cs} = 500 kg/m²·s. HTC and temperature profiles vs. position for the hot side and cold side.

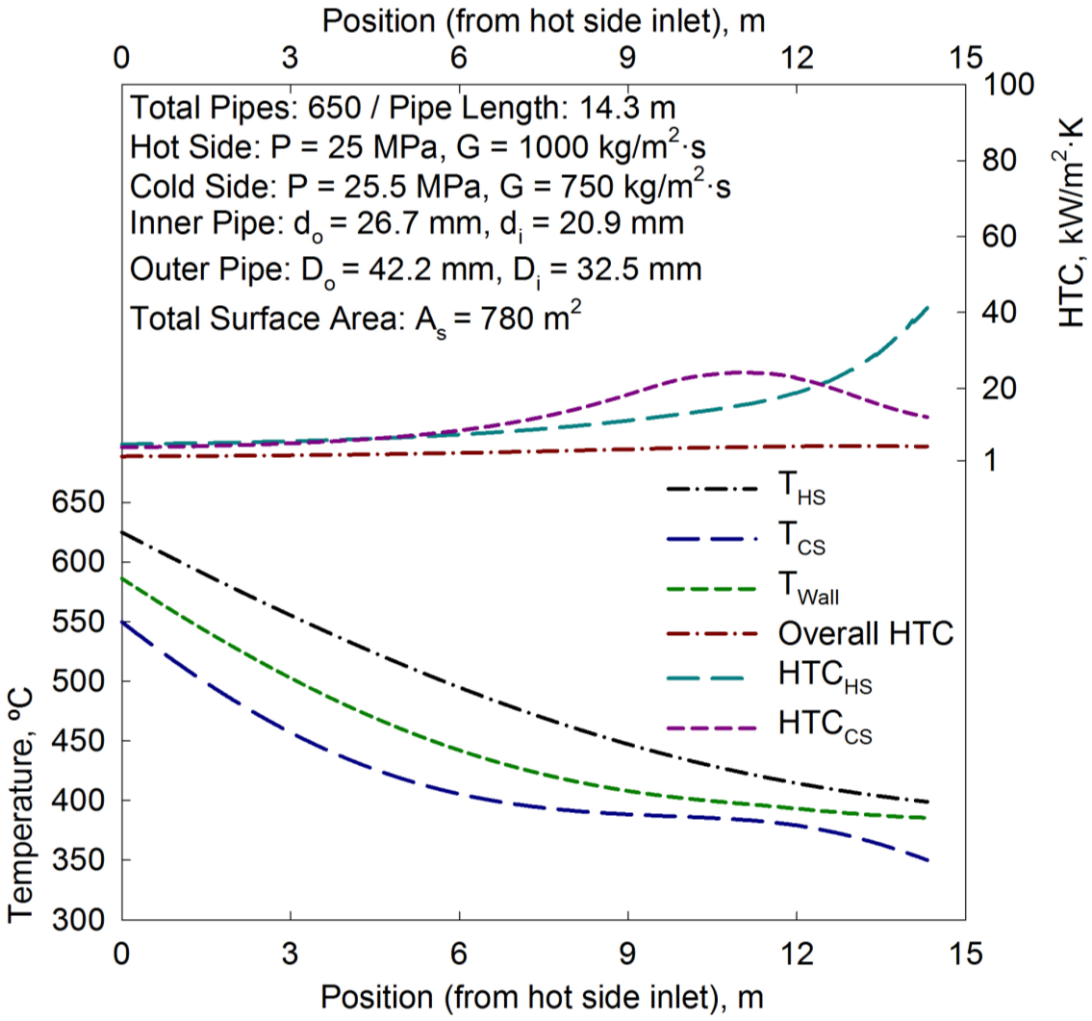

Figure 4-5. Test case #2 for HX-1: G_{cs} = 750 kg/m²·s. HTC and temperature profiles vs. position for the hot side and cold side.

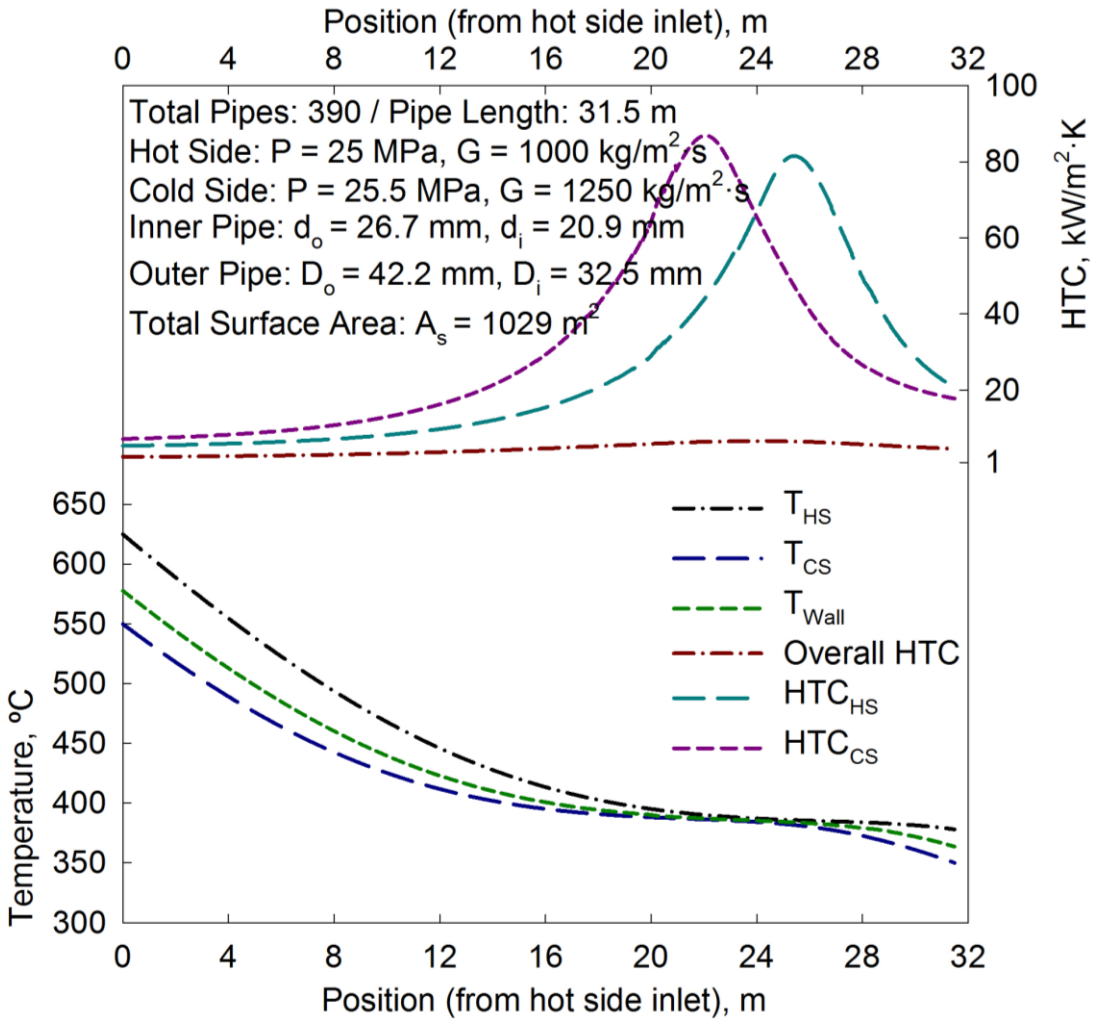

Figure 4-6. Test case #3 for HX-1: G_{cs} = 1250 kg/m²·s. HTC and temperature profiles vs. position for the hot side and cold side.

Two additional test cases on mass flux were developed. In these two cases, both the mass flux on the cold side and the hot side were varied as opposed to just the cold side mass flux. In test case #4, shown in Figure 4-7, mass flux was set to 500 kg/m^2·s on both the hot side and cold side. In test case #5, shown in Figure 4-8, mass flux was set to 1500 kg/m^2·s on both sides of the HX. The results from these two cases demonstrate a similar result as the test cases shown in Figure 4-4, Figure 4-5 and Figure 4-6. The results show that an increase in mass flux also increases the pipe lengths but decreases the number of pipes required. A decrease in mass flux showed the opposite result. As per Figure 4-7, when the mass flux is 500 kg/m^2·s for both sides the number of pipes required is 975 with a pipe length of 12.9 m. Figure 4-8 showed that number of 325 pipes with pipe lengths of 26.6 m were required for the production of hydrogen.

The results from Figure 4-7 and Figure 4-8 can be explained using Equations 3-4 and 3-5. When the mass flux is lowered the rate of heat transfer is also lowered. As a result, the energy being transferred to the cold side is also lowered and more pipes will be required. Additionally, when the mass flux is lowered the fluid is traveling slower through the HX. This means the fluid will spend more time in the HX and the length of pipes required to achieve the desired temperature change decreases. Consequently, a change in the number of pipes required and the length of these pipes impacts the total heat transfer surface area.

The best result in terms of heat transfer surface area was obtained from test case #5, shown in Figure 4-8. The mass flux of both fluids is set to 1500 kg/m^2·s in this test case and the total heat transfer surface area is 725 m^2. The worst result in terms of heat transfer area is test case #4, shown in Figure 4-7; the required heat transfer area is 1056 m^2. In test case #5, the length of the pipes is the second largest of all five test cases but the number of pipes required is the lowest. The reverse is true for test case #4. In this case the length of pipes is the second lowest but the number of pipes required is largest.

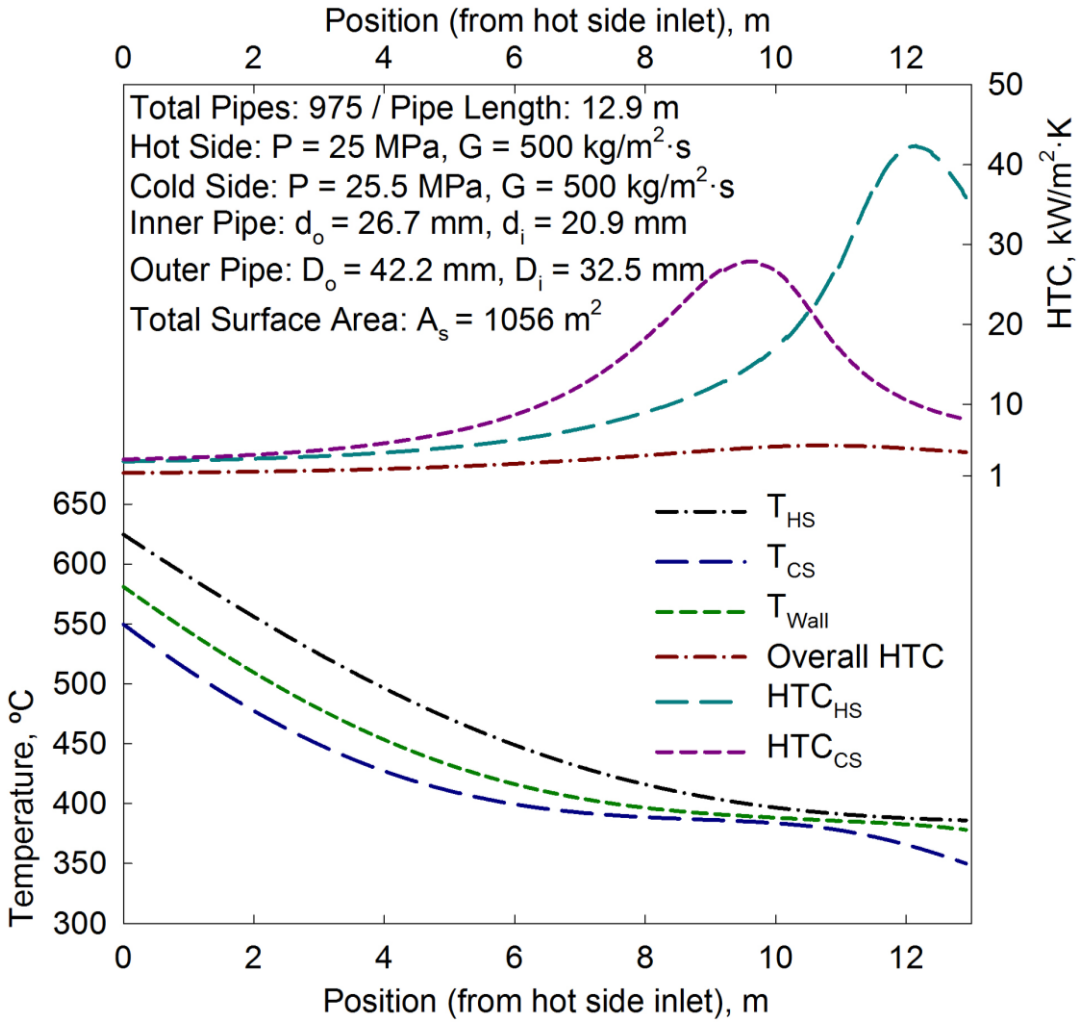

Figure 4-7. Test case #4 for HX-1: G = 500 kg/m²·s. HTC and temperature profiles vs. position for the hot side and cold side.

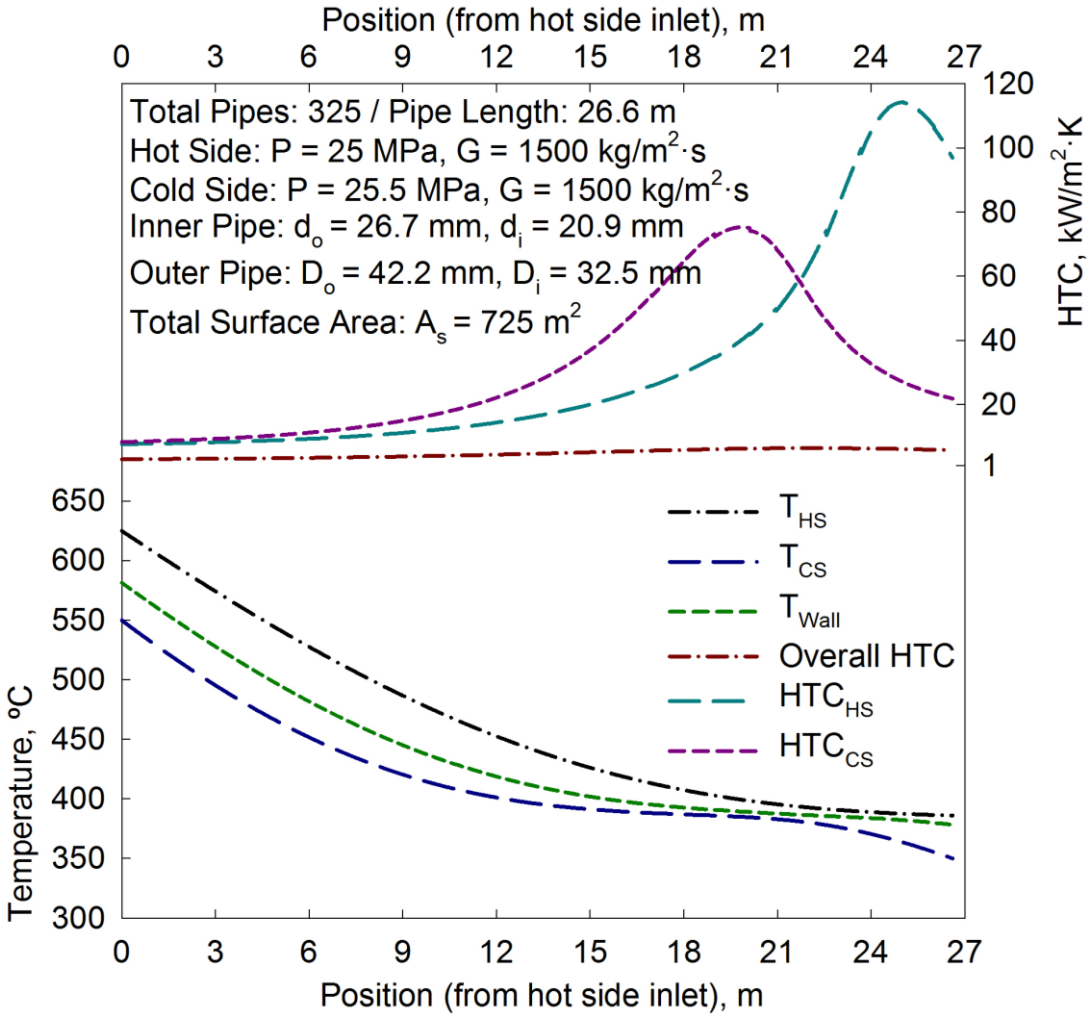

Figure 4-8. Test case #5 for HX-1: G = 1500 kg/m²·s. HTC and temperature profiles vs. position for the hot side and cold side.

Varying the magnitude of the mass flux also had an impact on the outlet temperature of the hot side. In the first three test cases, where only the mass flux of the cold side is varied, the outlet temperature of the hot side increases when the mass flux is decreased. The reverse is true for when the mass flux is increased as the outlet temperature of the hot side decreases. The hot side outlet temperatures shown in Figure 4-4, Figure 4-5 and Figure 4-6 are 440°C, 399°C and 378°C, respectively.

The outlet temperature of the hot side has a significant impact on the thermophysical property profiles of the fluid. In test case #1, the fluid does not enter the pseudocritical region. As a result, the thermophysical properties of the fluids do not undergo the significant variation that is experienced within the pseudocritical region. While this can be seen as a positive, it is important to note that the hot side fluid must return to the reactor once it has exited the HX. Since the inlet temperatures for SCWRs is approximately 350°C, having a relatively large disparity between the outlet temperature of the hot side of the HX and the reactor inlet temperature may not be beneficial due to the raised potential for thermal shock. As shown in Figure 4-7 and Figure 4-8, the outlet temperature of the hot side is 386°C in both cases. This can be attributed to the fact that the mass flux for the hot side and cold side is the same in both cases, which aligns with the results shown in the reference case where the mass flux is also the same for both fluids.

4.1.3 Sensitivity Analysis: Pressure

The impact of varying pressures on the cold side of the HX was assessed. Similar to what was done in the previous section, the pressure of the cold side was varied to determine the impact this would have on the size of the HX. Two test cases were conducted. The results from these test cases are shown in Figure 4-9 and Figure 4-10, respectively. In test case #6 the pressure of the cold side was decreased to 23 MPa. The number of pipes required for hydrogen production was 482 with pipe lengths of 19.6 m, with a total heat transfer surface area of 789 m^2. The hot side outlet temperature in this test case is 386^oC. In test case #7, when the pressure is increased to 28 MPa, the resultant number of pipes required was 494 with a length of 19.8 m per pipe. The resultant total heat transfer area was 819 m^2. The hot side outlet temperature for this test case is 386^oC.

From these results it is evident that the difference in HX size is not significantly different. It was shown that decreasing the pressure of the cold side will reduce the size of the HX, while increasing the pressure of the cold side has the opposite effect. In Figure 2-15, it was shown that while in the pseudocritical region, the thermal conductivity of water begins to decrease rapidly, experiences a local peak at the pseudocritical point, and then begins to decrease again. It was also shown that the magnitude of this local peak decreases with an increase in pressure. As previously discussed in Section 4.1.1, there is also a peak in specific heat. This is not a local peak as with thermal conductivity rather it is a global peak. This peak also becomes less pronounced with an increase in pressure as shown in Figure 2-14.

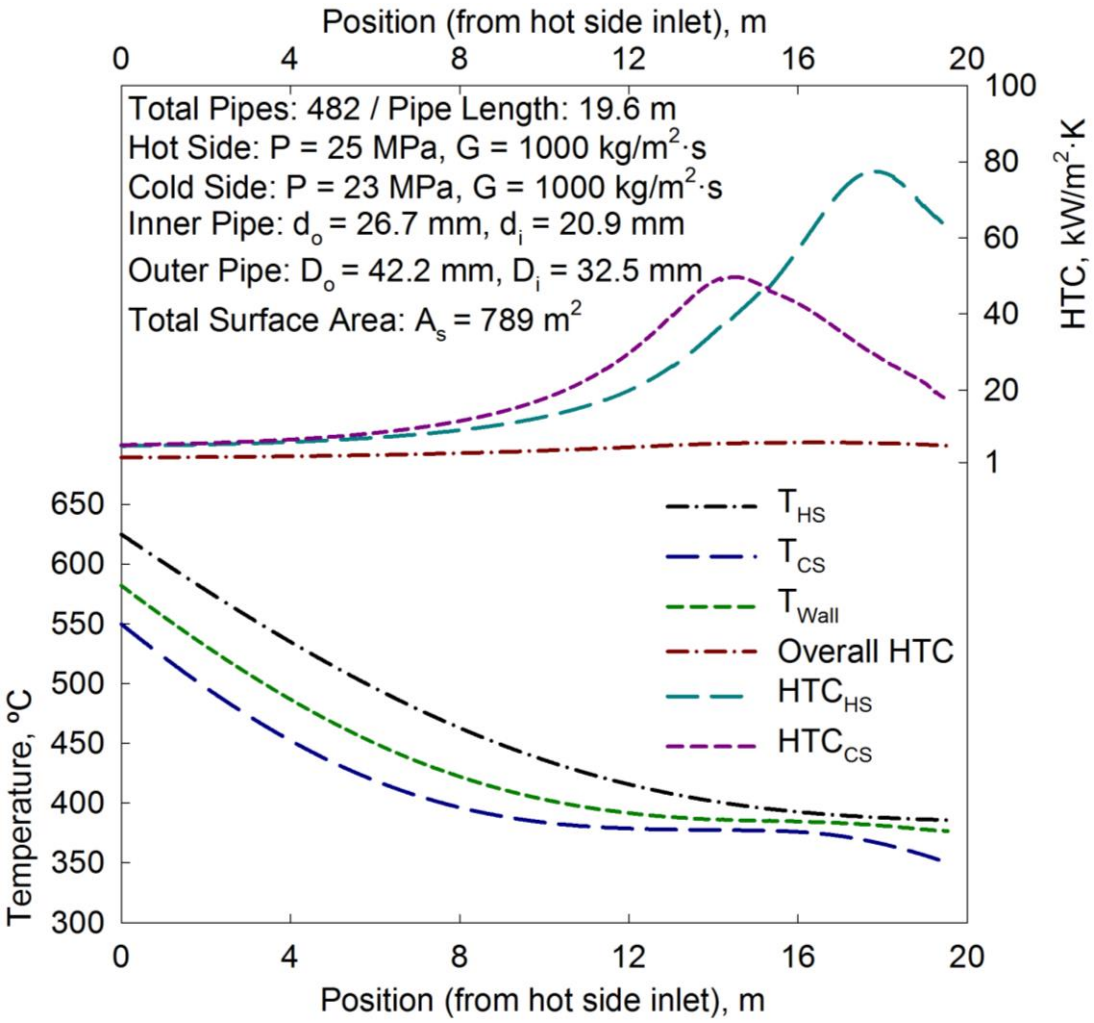

Figure 4-9. Test case #6 for HX-1: P_{cs} = 23 MPa. HTC and temperature profiles vs. position for the hot side and cold side.

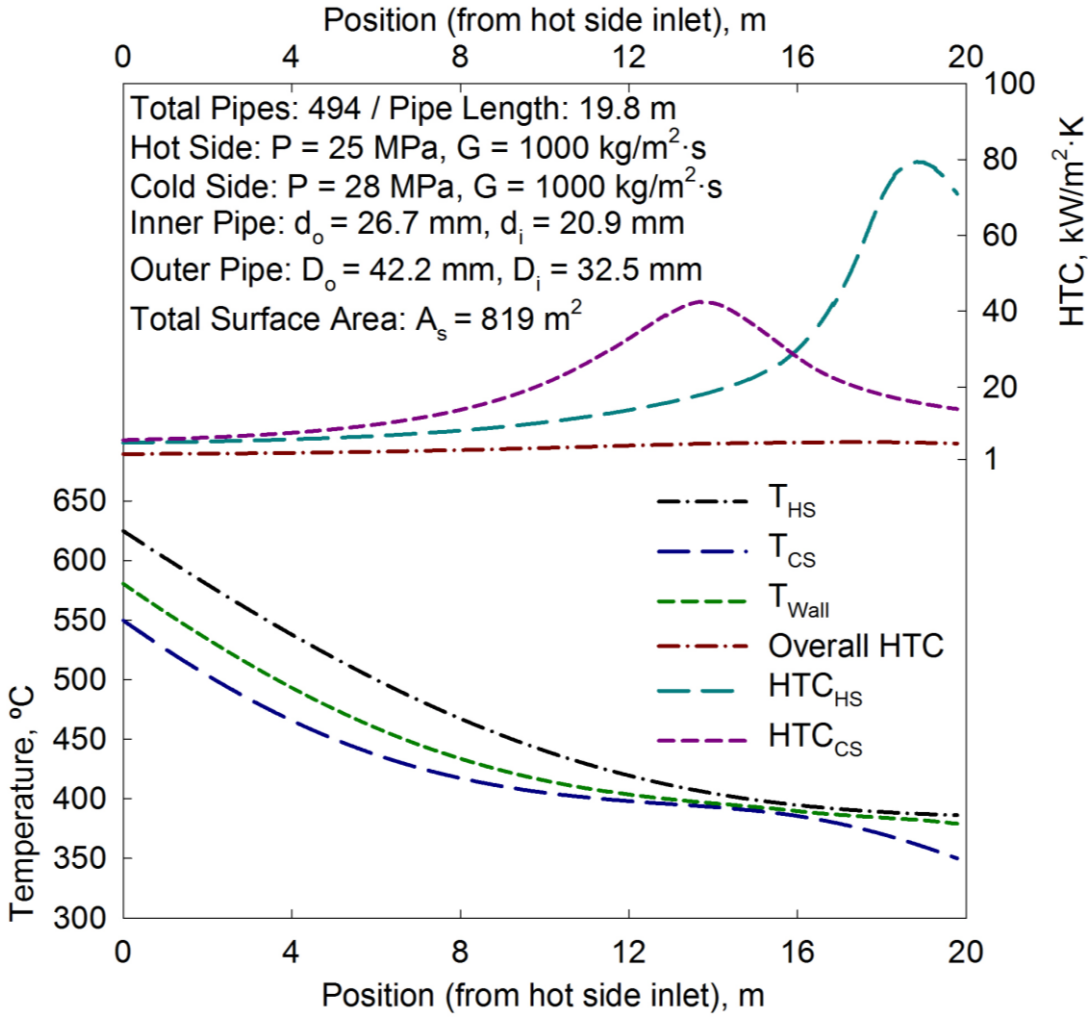

Figure 4-10. Test case #7 for HX-1: P_{cs} = 28 MPa. HTC and temperature profiles vs. position for the hot side and cold side.

In test case #6 where the pressure of cold side is 23 MPa, the peak in specific heat is much more prominent than at the 28 MPa in test case #7. This is due to the pressure in test case #6 being closer to the critical pressure of 22.064 MPa. At 23 MPa, more energy is required to raise the temperature of the fluid, which allows for the cold side to store more energy while passing through the pseudocritical region. Therefore, since the fluid has a greater energy content, the number of pipes required in the HX was reduced. While this would suggest that the fluid at 23 MPa would require a longer pipe length to achieve the desired temperature change across the length of the HX, the thermal conductivity of the fluid is also higher in the pseudocritical region at 23 MPa when compared to 28 MPa. It is the combined effect of the respective local and global peaks in thermal conductivity and specific heat, which allow for the size of the HX to be reduced with a reduction in cold side pressure. The thermophysical property profiles along the length of the HX for test cases #6 and #7 can be found in Figure B-2 and Figure B-3, respectively.

Since the fluid of the hot side is the reactor coolant from an SCWR, it is not likely that the pressure of the hot side would be changed for this HX. As a result, no test cases were conducted with regards to changing of pressure on the hot side.

4.1.4 Sensitivity Analysis: Piping Dimensions

A sensitivity analysis was conducted on the dimensions of the pipes in the HX, more specifically, the diameters of the pipes used in the HX. For the reference case, the inner diameter of the inner pipe is 20.9 mm. To begin the sensitivity analysis, the inner diameter of the inner pipe was decreased. This was done by increasing the thickness of the wall of the inner pipe, resulting in an inner diameter of 18.8 mm. The results from test case #8 are shown in Figure 4-11. The resultant number of pipes required in this test case was 488 with a length of 28.9 m per pipe. The hot side outlet temperature is 379^{o}C.

In the test case #9, the inner diameter of the inner pipe was increased by decreasing the thickness of the wall; an inner diameter of 21.8 mm was selected. The results from this test case are shown in Figure 4-12. The resultant number of pipes required was 488 with a length of 17.7 m per pipe. The hot side outlet temperature is 388^{o}C.

When the diameter of the inner pipe was decreased, the surface area in which heat transfer takes place also decreased, consequently increasing the length of the pipes. Increasing the inner diameter of the inner pipe had the opposite effect. By increasing the inner diameter, the surface area in which heat transfer can take place also increased, therein by reducing the length of the pipes. The total heat transfer surface area for test case #8 and test case #9 was found to be 1184 m^2 and 720 m^2, respectively. As shown in Equation 3-10, the rate of heat transfer is proportional to the heat transfer surface area. Therefore, by increasing the inner diameter of the inner pipe, consequently increasing the heat transfer surface area, the rate of heat transfer was also increased. Ultimately, this resulted in a decrease to the required pipe lengths.

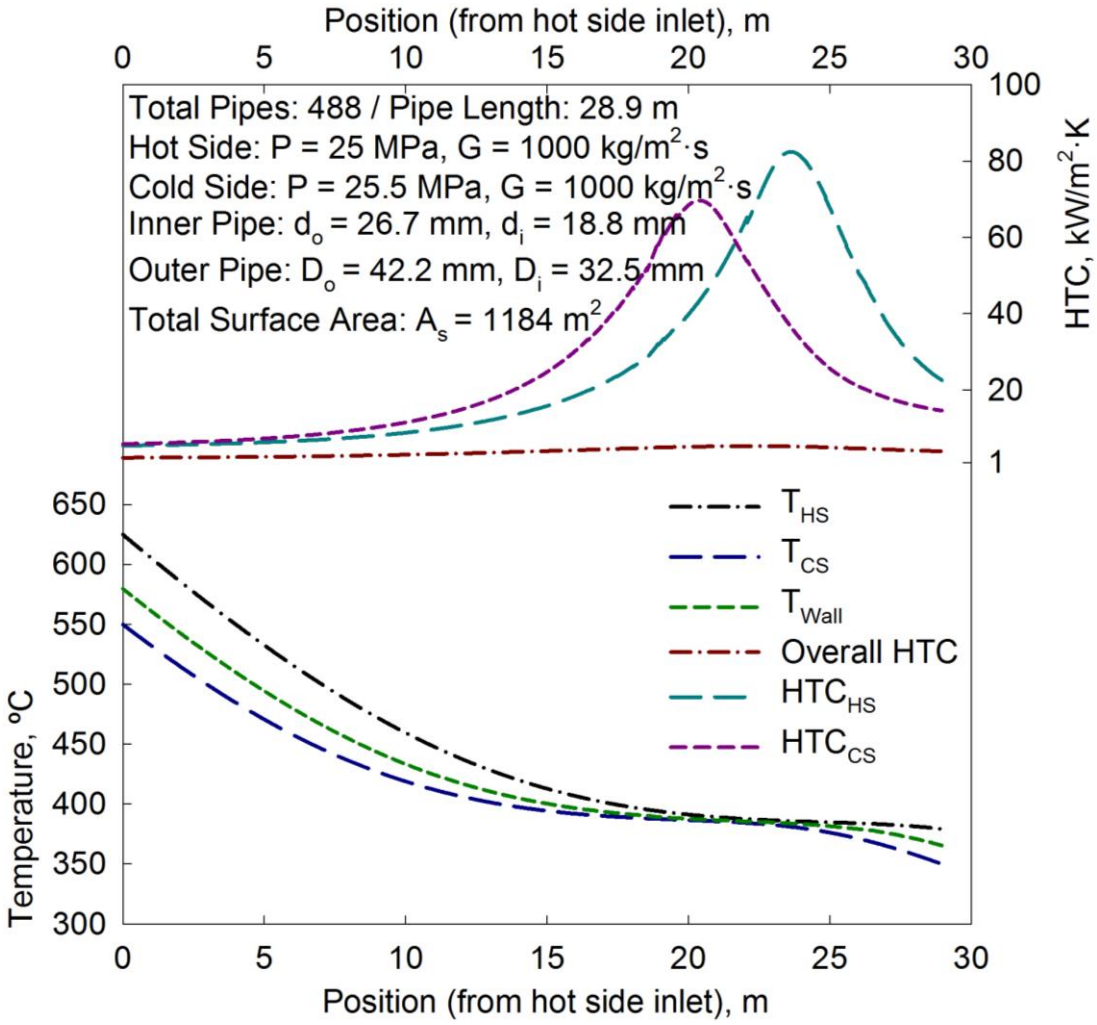

Figure 4-11. Test case #8 for HX-1: d_o = 18.8 mm. HTC and temperature profiles vs. position for the hot side and cold side.

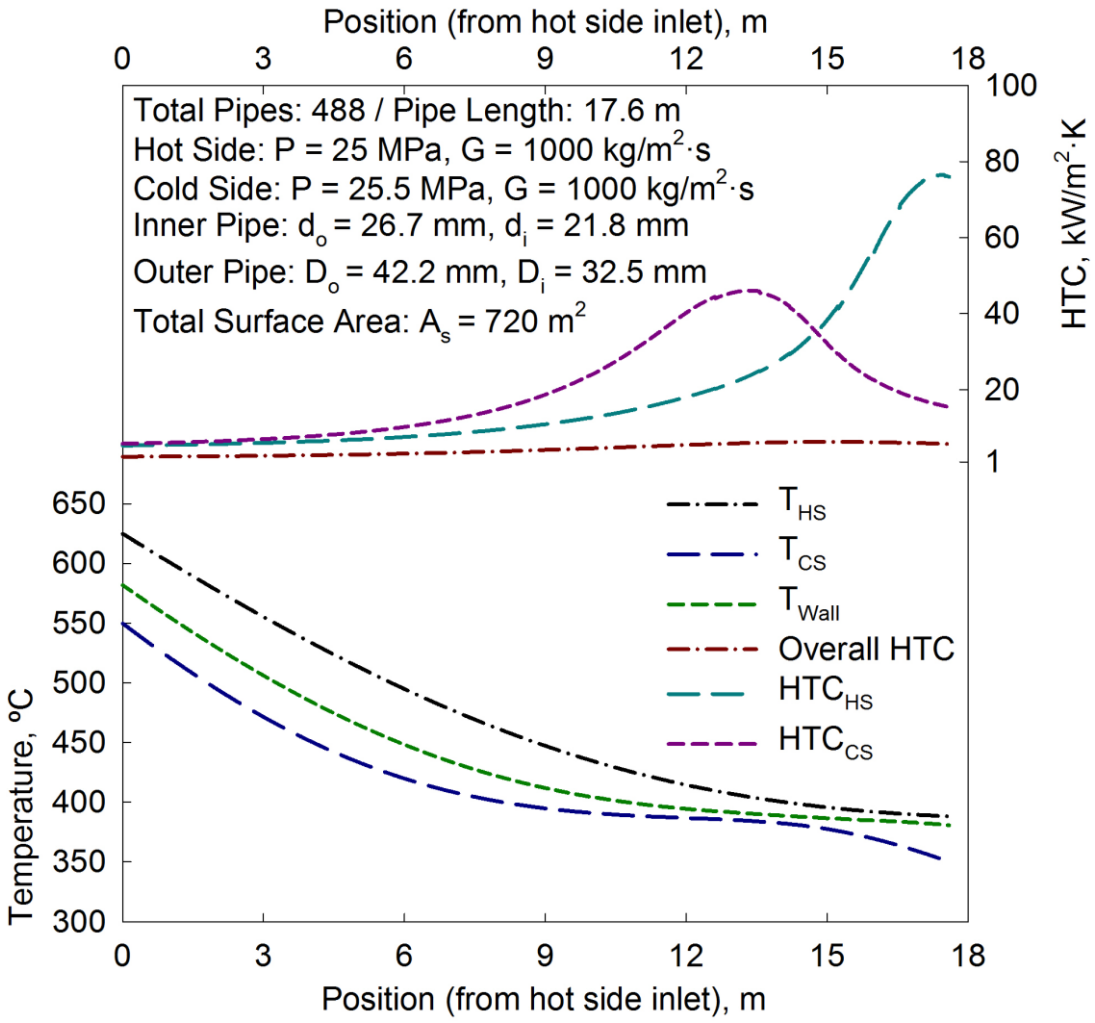

Figure 4-12. Test case #9 for HX-1: d_o = 21.8 mm. HTC and temperature profiles vs. position for the hot side and cold side.

In the final test case for HX-1 the inner diameter of the inner pipe was set to 26.6 mm. In order for the inner diameter of the inner pipe to be increased to 26.6 mm, additional dimensions had to change. The outer diameter of the inner pipe had to be increased to conform to standard NPS dimensions and to comply with ASME standards. This prompted for the dimensions of the outer pipe to be changed as well, to accommodate for the increase to the inner pipe. As a result, all of the piping dimensions were altered for test case #10. The outer diameter of the inner pipe was set to 33.4 mm. The inner and outer diameter of the outer pipe were set to 38.1 mm and 48.26 mm, respectively. The results from test case #10 are shown in Figure 4-13. The resultant number of pipes was 496 and with a length of 14.2 m per pipe. The total required heat transfer surface area was found to be 738 m^2. The hot side outlet temperature is 418^oC.

Comparing the results from test case #9 and test case #10 shows that while the inner diameter of the inner pipe is larger in test case #10, the total heat transfer surface area is smaller in test case #9. This can be attributed to the fact that all of the piping dimensions in the HX were increased for test case #10. Additionally, while the pipes are shorter in test case #10, due to an increased surface area, the number of pipes required is actually larger. In test cases #8 and #9, the number of pipes required is the same. This is because the dimensions of the outer pipe remain the same in both test cases. This does not apply for test case #10, where all piping dimensions were changed. Due to a change in the outer pipe dimensions, the mass flow rate of the cold side was also changed. Consequently, this affected the number of pipes required.

Due to the changes in the piping dimensions, the cross-sectional area of the cold side in test case #10 was reduced to 263.9 mm^2 from 269.7 mm^2 in test case #8 and #9. Therefore, as per Equation 3-6, the mass flow rate on the cold side is decreased. As shown in Equation 3-4, decreasing the mass flow rate reduces the amount of energy being transferred per pipe. For this reason, the number of pipes required in test case #10 is increased.

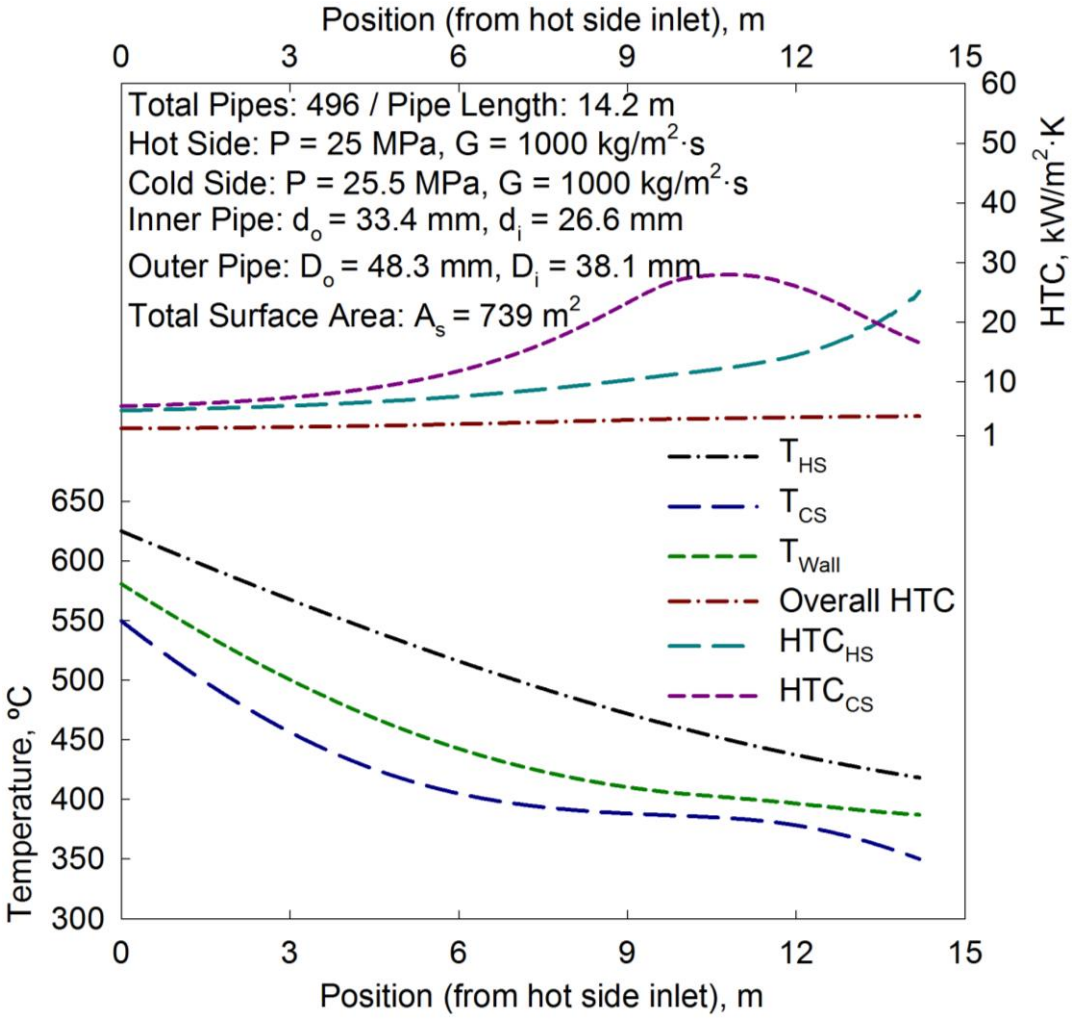

Figure 4-13. Test case #10 for HX-1: d_o = 26.6 mm. HTC and temperature profiles vs. position for the hot side and cold side.

4.2 HX-2: SCW-to-Supercritical CO_2

In addition to the analysis presented as a part of Section 4.1, an analysis on HX-2 was also conducted. A reference case and ten additional test cases on HX-2 are presented in this section.

4.2.1 Reference Case

The operating parameters used in this reference case are listed in Table 3-5 in Section 3.4.1.

Based on the operating parameters for this reference case, it was determined that the total mass flow rate of the hot side is 1120 kg/s. This is approximately 92% of the total mass flow rate in the current Canadian SCWR concept. This is the amount that would need to be diverted in order to meet thermal energy requirement associated with a hydrogen production rate of 1 kg/s. Ultimately, this is too large of a commitment as almost of all of the reactor coolant would need to leave the reactor for hydrogen production. Diverting this much of the reactor coolant for hydrogen production would significantly reduce the amount of electricity that can be generated by the reactor. This is in stark contrast to what the actual purpose a nuclear generating station is intended to do. Consequently, for HX-2 to be feasible, the desired production rate would need to be significantly decreased. For the purpose of having an equivalent point of comparison between HX-1 and HX-2, the thermal energy requirement used in the analysis of HX-2 was kept at 224 MW_{th}.

The results for the reference case of HX-2 are shown in Figure 4-14. These results show that a total of 3540 pipes with a length of 3.85 m per pipe to produce hydrogen at the desired rate of 1 kg/s. This amounts to a total heat transfer area of 1143 m^2. The outlet temperature of the hot side in this reference case is 564^oC.

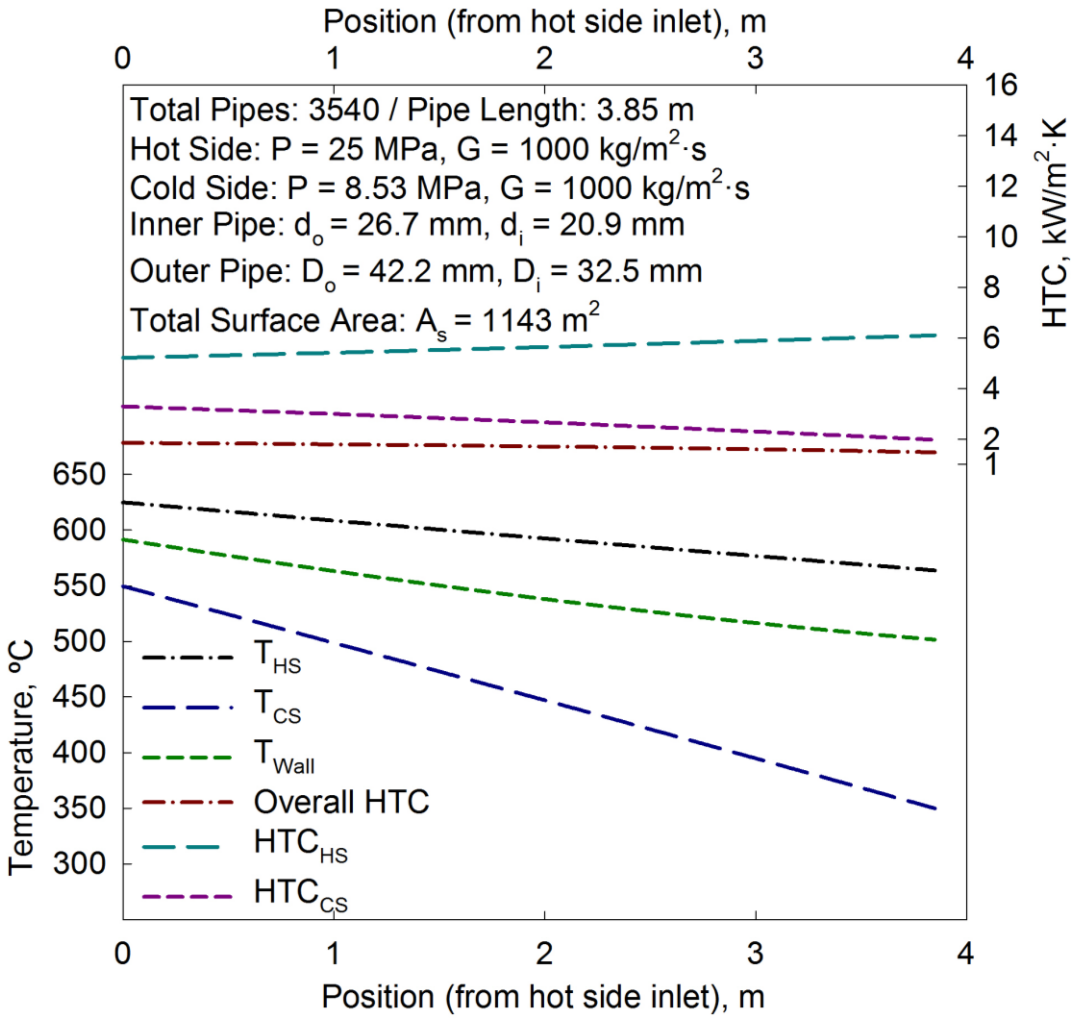

Figure 4-14. Reference Case for HX-2: Hot side, cold side and wall temperatures vs. position. Local and overall HTC vs. position.

Comparing the results from Figure 4-14 to those from Figure 4-1 show a rather stark contrast in the total number of pipes and pipe lengths required. This can be attributed to the critical point of CO_2. The critical point of CO_2 is 30.98°C and 7.3773 MPa. As shown in Figure 2-24, supercritical CO_2 experiences a peak in specific heat similar to that of water at the critical and pseudocritical point. It is also evident that above 80°C the profile for specific heat has completely flattened out. Since the HX operates well above the critical point of CO_2, the fluid does not experience the drastic peak in specific heat associated with the pseudocritical point within the HX. This can be seen in Figure B-4 in Appendix B. As a result, the cold side of HX-2 does not require nearly as much heat to achieve the desired temperature change. For this reason, the resultant pipes length for HX-2 are much lower than those obtained in HX-1.

The energy content of the pipes in the reference case for HX-2 is much lower than that of those HX-1. The number of pipes required to meet the thermal energy requirement for HX-2 is 3540. This is significantly higher than the 488 result from the reference case for HX-1.

From the profiles shown in Figure 4-14, it is evident that there is no peak in the HTC profile for the either the hot side or the cold side. This is a result of the HX operating entirely outside of the pseudocritical region. On the cold side, the operating temperature of the supercritical CO_2 working fluid is well beyond the pseudocritical point. On the hot side, the SCW exits the HX at 564°C, well above the pseudocritical point. Therefore, since neither fluid enters the pseudocritical region, there is no significant variation in thermophysical properties, more specifically the average specific heat.

While it may be considered a positive that neither fluid in the HX experiences a significant variation in thermophysical properties, it is also worth noting that the outlet temperature of the hot side was found to be 564°C. This is well above the

reactor inlet temperature of 350°C and must be taken into account due to the potential stresses that may result from thermal shock.

For comparison, a test case was developed using supercritical CO_2 on both the hot side and the cold side of the HX. The operating pressures and temperatures of both fluids have been scaled down to equivalent conditions of the reference case shown in Figure 4-1. The operating pressures and temperatures of this equivalent case are listed in Table 4-1.

Table 4-1. Operating parameters for equivalent case counter-flow double-pipe HX-2

Operating Parameter	**Inner Pipe (Hot Side)**	**Annulus Gap (Cold Side)**
Fluid	Supercritical CO_2	Supercritical CO_2
Pressure (MPa)	8.36	8.53
Inlet temp. (°C)	52	29
Outlet temp. (°C)	36	46

The objective of this thesis is to assess the performance of supercritical fluids in a HX application for the production of hydrogen. The purpose for showing this equivalent case is to show the significance of the pseudocritical region when it comes to heat transfer in supercritical fluids. As shown in Figure 4-15, there is a peak in the HTC profiles as the fluids travel through the pseudocritical region. As previously discussed in Section 4.1.1, the peaks in HTC are a result of the peaks in the average specific heat of the fluid. It is also evident that in the region in which the HTC profiles experience a peak, the temperature profiles of the fluids begin to flatten out. This is once again attributed to the peak in specific heat as more energy is required to increase the temperature of the fluid. For this reason, the length of the pipes increase.

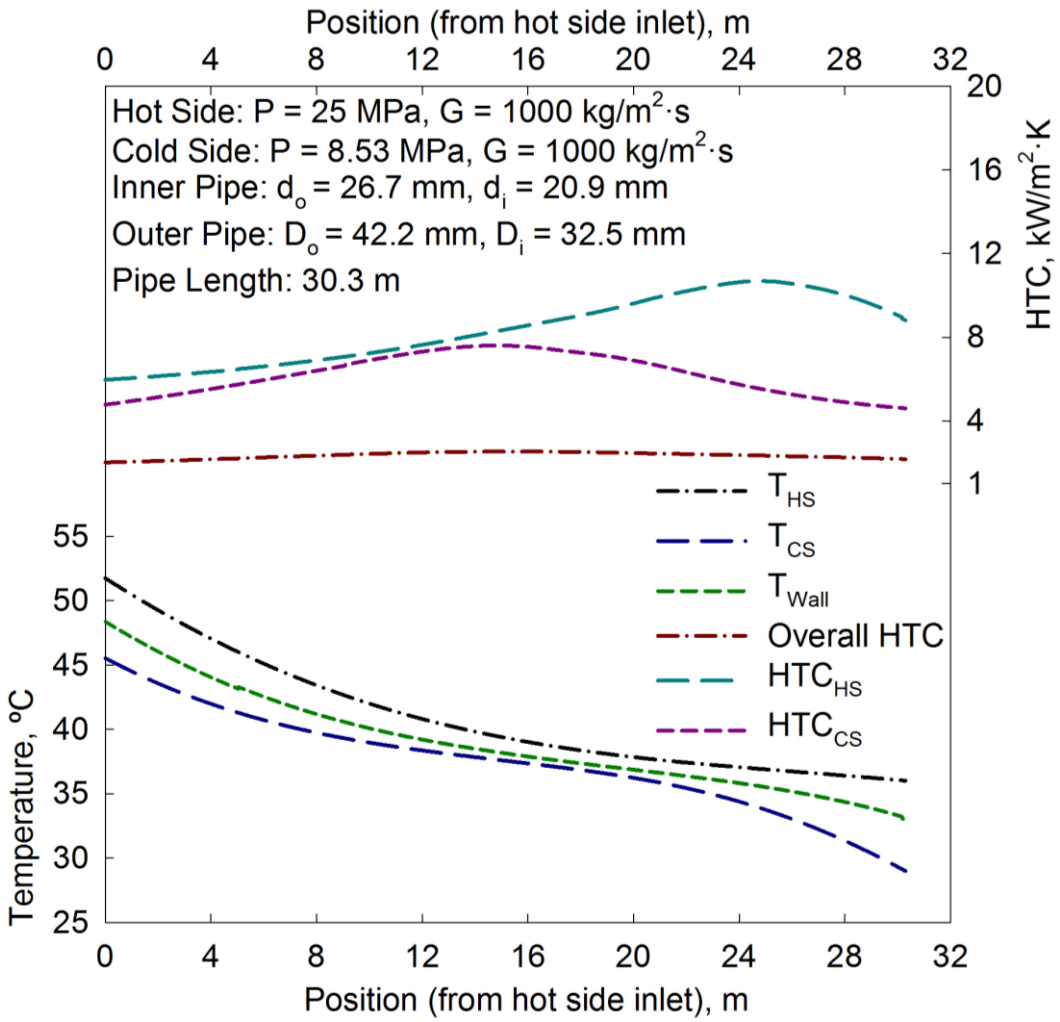

Figure 4-15. Equivalent Case for HX-2: Hot side, cold side and wall temperatures vs. position. Local and overall HTC vs. position.

4.2.2 Sensitivity Analysis: Mass Flux

A sensitivity analysis was conducted on HX-2 to determine the impact of the cold side mass flux on the size of the HX. The mass flux on the cold side was varied from 500 kg/m^2·s to 1250 kg/m^2·s in increments of 250 kg/m^2·s, excluding 1000 kg/m^2·s, as this value was used in the reference case. For the remaining two test cases the mass flux on both the hot side and the cold side were set to 500 kg/m^2·s and 1500 kg/m^2·s.

In test case #11, shown in Figure 4-16, the mass flux on the cold side was set to 500 kg/m^2·s. The results showed that 7079 total pipes with a length of 3.16 m per pipe would be required to meet a hydrogen production rate of 1 kg/s. The total heat transfer surface area in this test case was found to be 1875 m^2. The outlet temperature of the hot side in test case #11 is 594^{o}C. In test case #12, shown in Figure 4-17, the mass flux was set to 750 kg/m^2·s. This resulted in requirement of 4720 total pipes with a length of 3.49 m per pipe. The hot side outlet temperature is 578^{o}C. The total heat transfer surface area was found to be 1382 m^2. In test case #13, shown in Figure 4-18, the mass flux on the cold side was increased to 1250 kg/m^2·s. The resultant number of pipes required was 2832 with a length of 4.25 m per pipe. The resultant total heat transfer surface area of 1007 m^2. This outlet temperature for this test case is 549^{o}C.

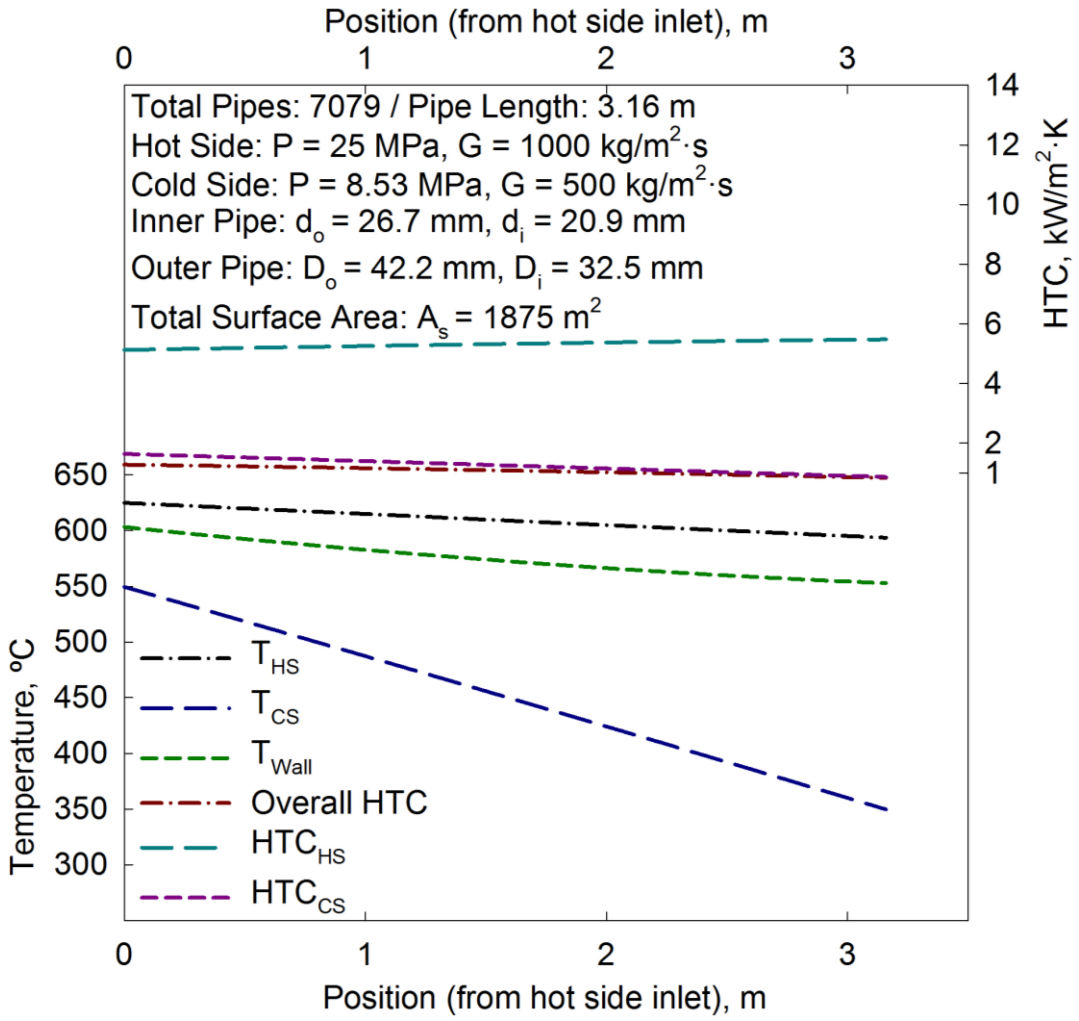

Figure 4-16. Test case #11 for HX-2: G_{cs} = 500 kg/m²·s. HTC and temperature profiles vs. position for the hot side and cold side.

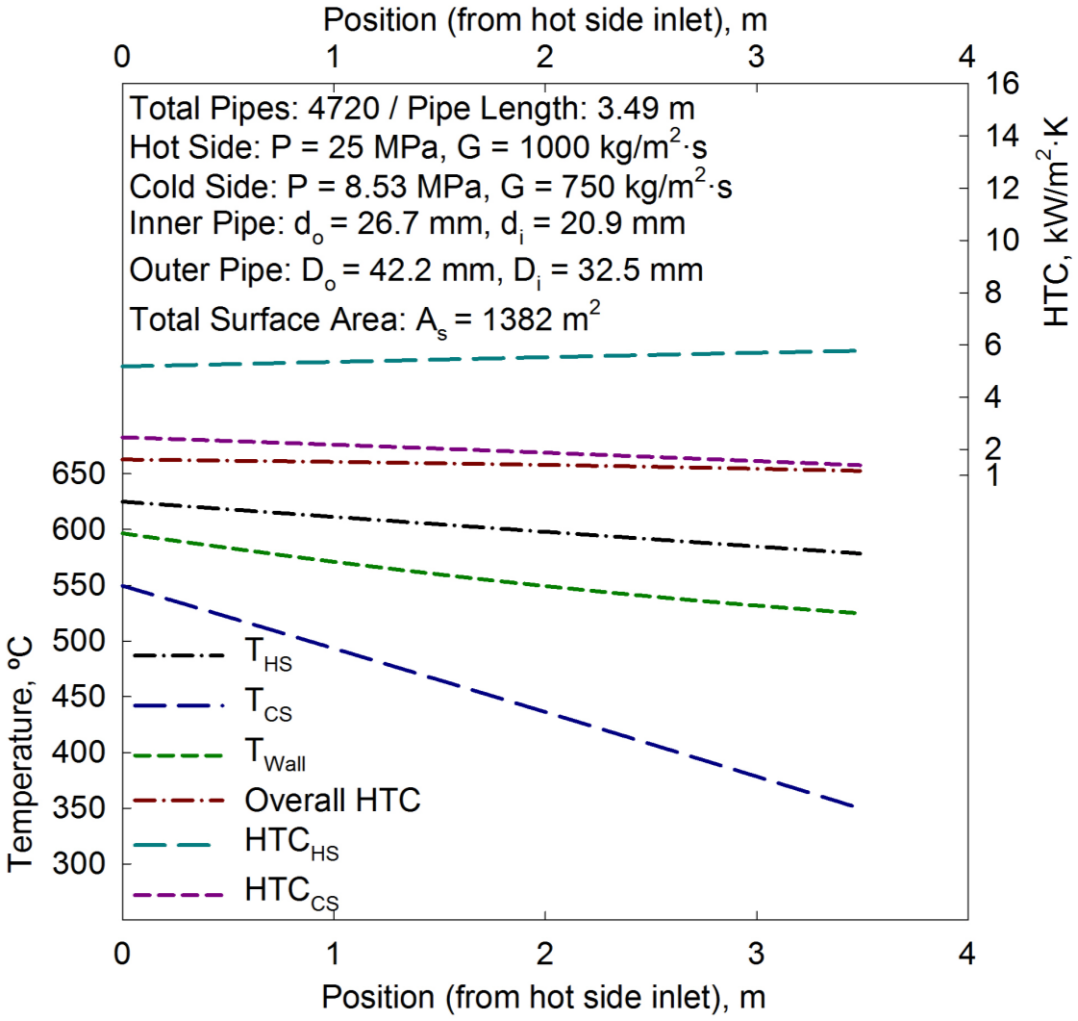

Figure 4-17. Test case #12 for HX-2: G_{cs} = 750 kg/m²·s. HTC and temperature profiles vs. position for the hot side and cold side.

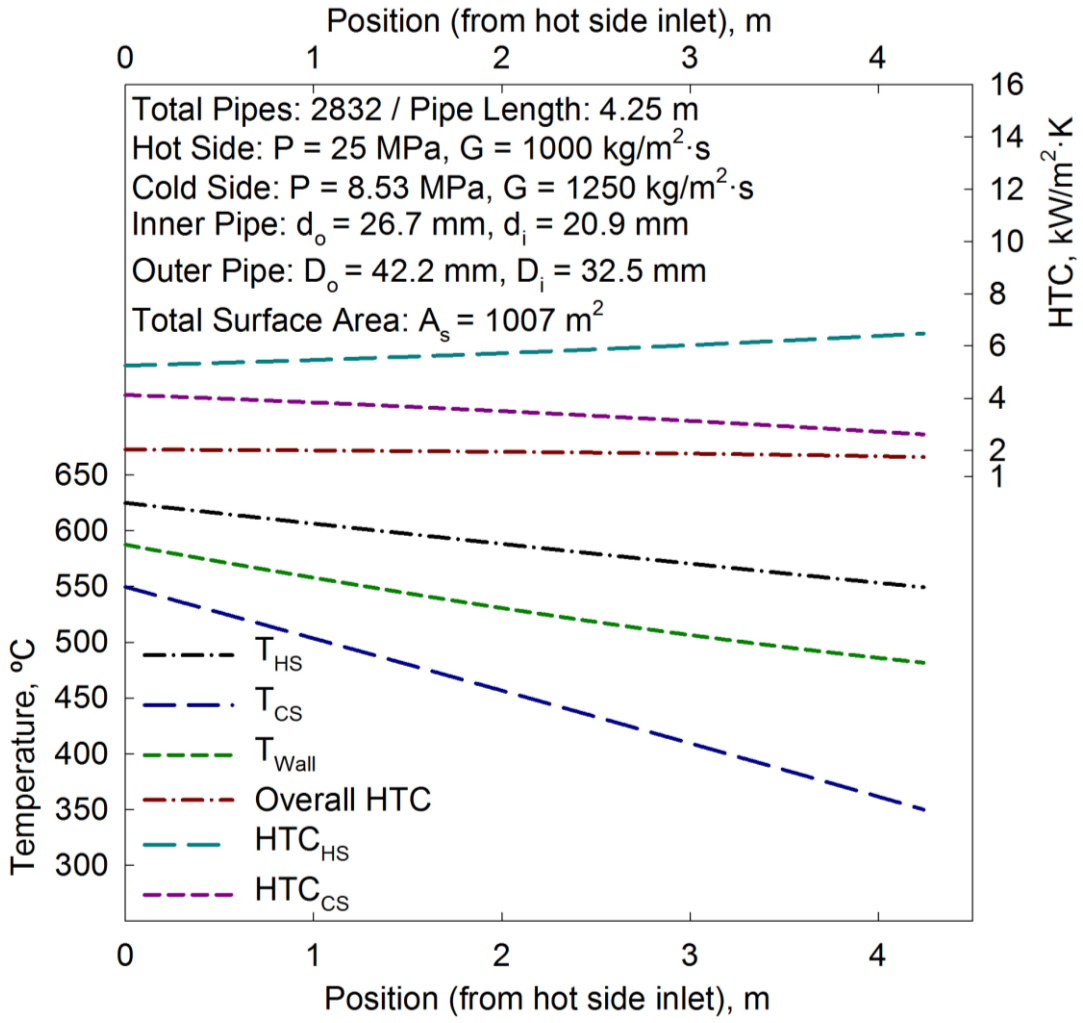

Figure 4-18. Test case #13 for HX-2: G_{cs} = 1250 kg/m²·s. HTC and temperature profiles vs. position for the hot side and cold side.

The results from test case #14 are shown in Figure 4-19. In this test case, both the hot side and cold side mass flux are set to 500 kg/m^2·s. The number of pipes required in this test case was found to be 7079 with a length of 3.42 m per pipe. The resultant total heat transfer surface area was 2027 m^2. The hot side outlet temperature in this test case is 564^{o}C. For test case #15, the mass flux for both the hot side and the cold side was set to 1500 kg/m^2·s, as shown in Figure 4-20. The resultant number of pipes required was 2360 with a pipe length of 4.25 m. The total heat transfer surface area in this test case was found to be 840 m^2. The hot side outlet temperature is 564^{o}C.

Similar to the results from HX-1, the length of the pipes is proportional to the mass flux of the fluids. The required number of pipes is inversely proportional to the mass flux of the fluid. The test case resulting in the lowest total heat transfer surface area was test case #15. This is when the mass flux of both the hot side and the cold side was increased to 1500 kg/m^2·s. One of the major reasons for this is due to significant decrease in the number of pipes required. As the mass flux of the fluids is increased, the mass flow rate is also increased, resulting in a greater energy content per pipe, therein by reducing the number of pipes required.

The worst result in terms of total heat transfer surface area is obtained when the mass flux was decreased to 500 kg/m^2·s on both sides of the HX. The results from this case showed that since the fluid is traveling slower, the required pipe lengths decreased, which also lowered the energy content of the pipes. As a result, the number of pipes required increased significantly. Consequently, the total required surface area was increased.

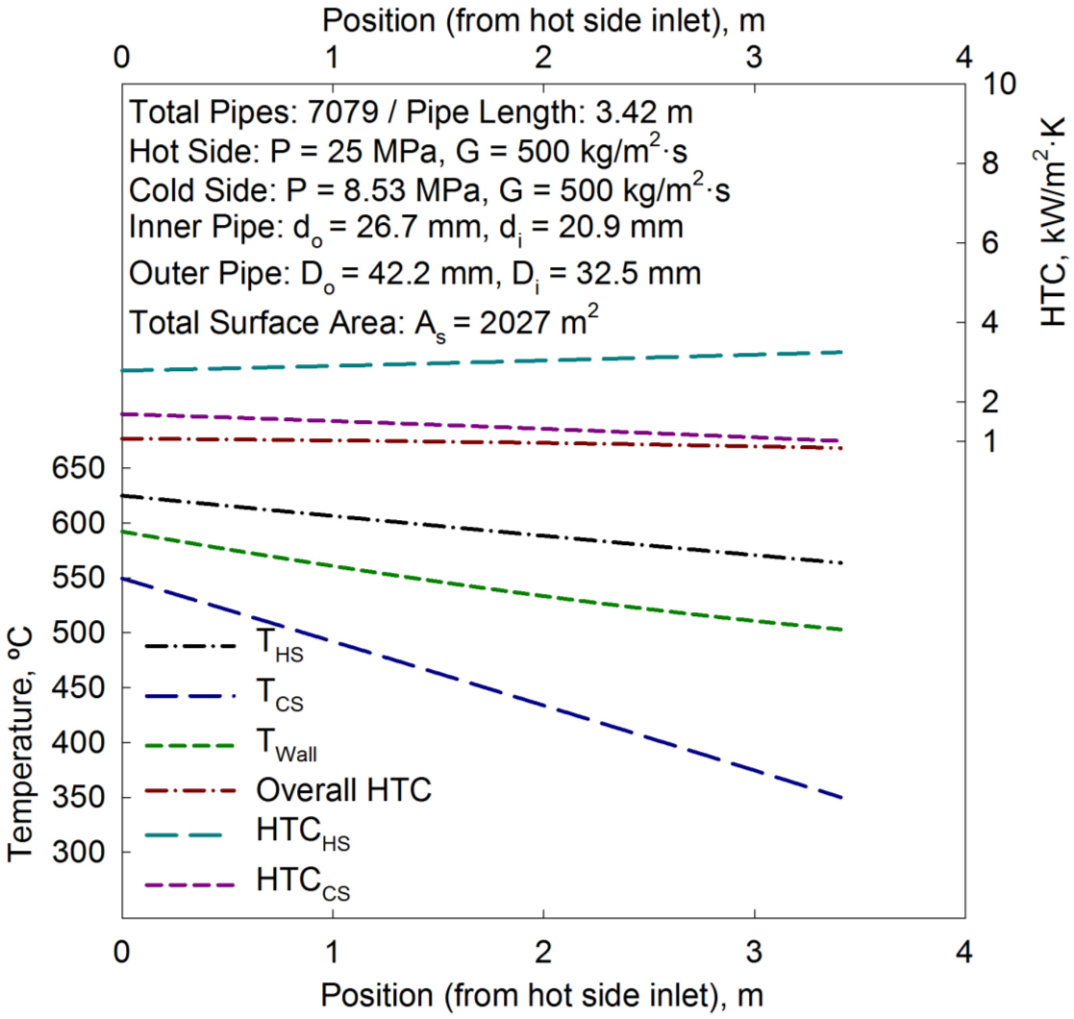

Figure 4-19. Test case #14 for HX-2: *G* = 500 kg/m²·s. HTC and temperature profiles vs. position for the hot side and cold side.

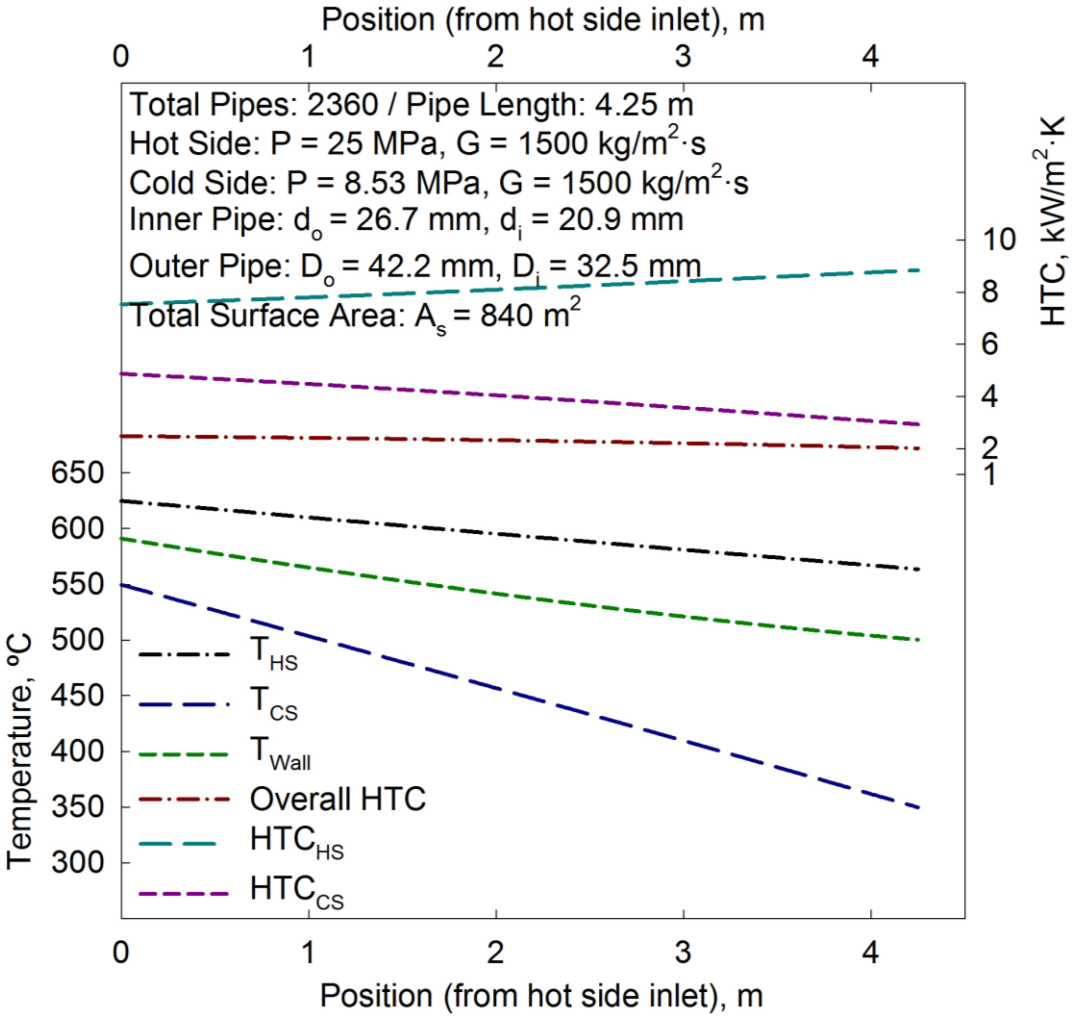

Figure 4-20. Test case #15 for HX-2: G = 1500 kg/m²·s. HTC and temperature profiles vs. position for the hot side and cold side.

4.2.3 Sensitivity Analysis: Pressure

The impact of varying the cold side pressure on the size of HX-2 was assessed. Two test cases were conducted where the pressure on the cold side was set to 7.69 MPa and 9.36 MPa. The results are shown in Figure 4-21 and Figure 4-22. These pressures are equivalent pressures that have been scaled down from the 23 MPa and 25 MPa used in the test cases for HX-1; pressures were scaled down using Equation 2-1.

Test case #16 shows that when the pressure on the cold side is decreased to 7.69 MPa, the resultant number of pipes required was 3552 with a length of 3.85 m per pipe. The hot side outlet temperature in this test case is 564°C. The resultant total surface area was found to be 1147 m^2. In test case #17, when the pressure is increased to 9.36 MPa, the required pipe length was determined to be 3.86 m with a total of 3528 pipes required. The outlet temperature in this test case is 563°C. The total heat transfer surface area was found to be 1140 m^2.

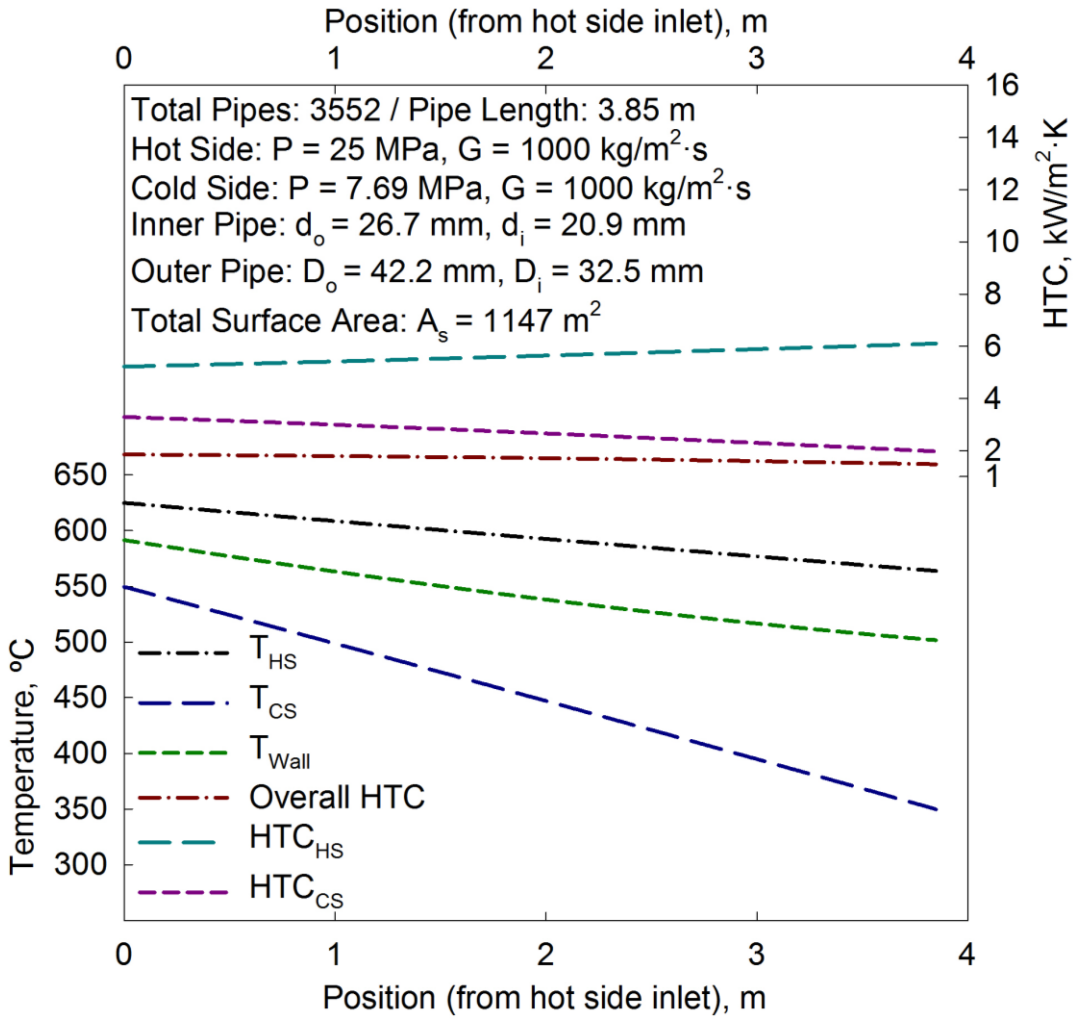

Figure 4-21. Test case #16 for HX-2: P_{cs} = 7.69 MPa. HTC and temperature profiles vs. position for the hot side and cold side.

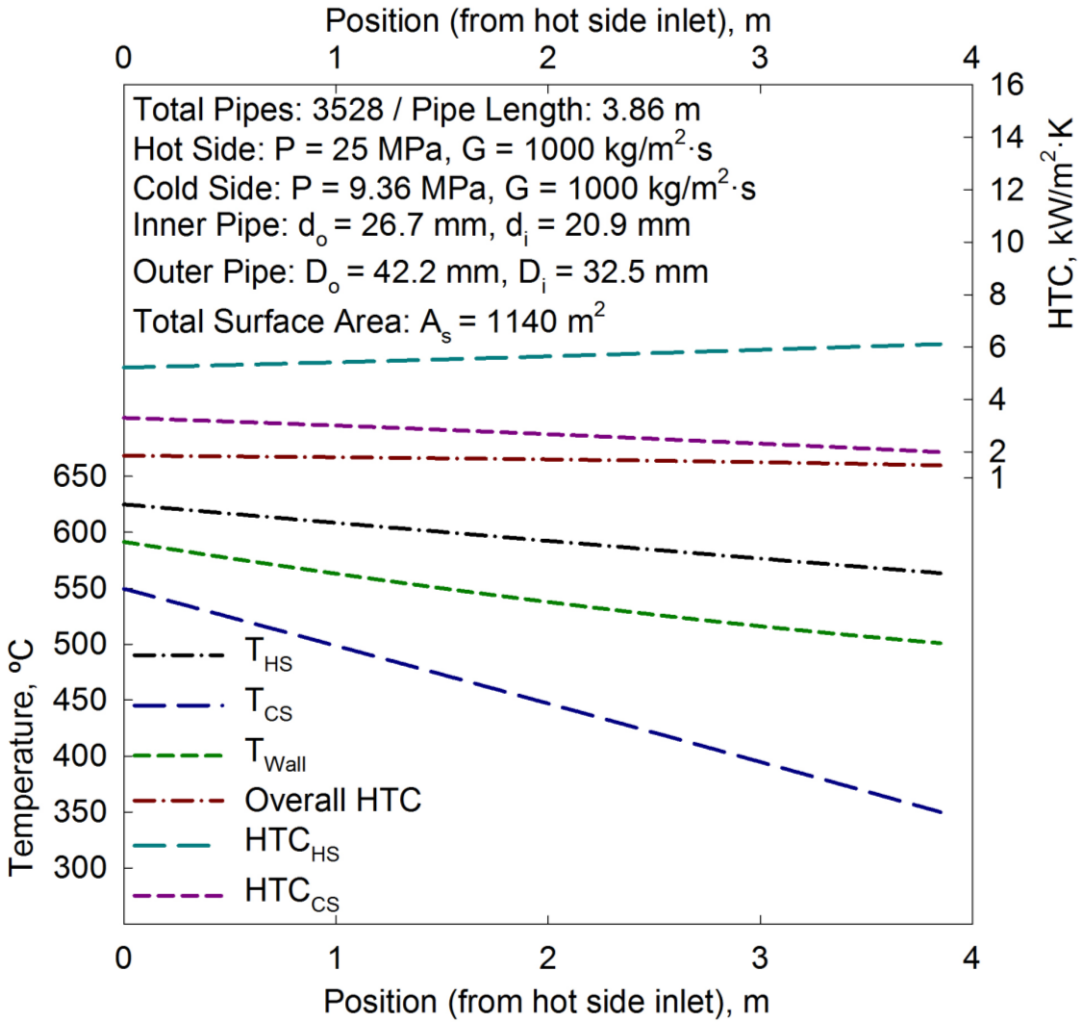

Figure 4-22. Test case #17 for HX-2: P_{cs} = 9.36 MPa. HTC and temperature profiles vs. position for the hot side and cold side.

When the pressure of the cold side is increased in HX-2, the overall heat transfer surface of the HX decreases slightly. This result is the opposite of what occurred in the sensitivity analysis of pressure in HX-1. The major difference between these two analyses is that HX-2 does not operate in pseudocritical region. As shown in Section 2.3, specific heat and thermal conductivity experience a global peak and local peak, respectively, in the pseudocritical region. For this reason, the values of these peaks are significantly higher at lower pressures. Consequently, when the pressure was decreased in HX-1, the total heat transfer surface area also decreased.

Since HX-2 operates outside of the pseudocritical region, the fluid will neither experience a peak in specific heat nor in thermal conductivity. As a result, the thermal conductivity and specific heat of the fluid at 9.36 MPa is slightly larger than when at 7.69 MPa, resulting in a smaller HX. The thermophysical property profiles for test case #16 and #17 are shown in Figure B-5 and Figure B-6.

4.2.4 Sensitivity Analysis: Piping Dimensions

The final sensitivity analysis conducted was on the piping dimensions of the HX-2. Similar to what was done for HX-1, the analysis focused on the diameters of the pipes. In test case #18, shown in Figure 4-23, the inner diameter of the inner pipe was decreased to 18.8 mm. The results showed that 3540 total pipes were required with a length of 3.84 m per pipe to meet the 1 kg/s production rate. The hot side outlet temperature is 550°C. Figure 4-24 shows the results of test case #19, where the inner diameter of the inner pipe was increased to 21.8 mm. The resultant number of pipes required was 3540 with a length of 3.86 m per pipe. The hot side outlet temperature is 568°C. The total heat transfer surface area for test case #18 and test case #19 are 1139 m^2 and 1146 m^2, respectively. Since the number of pipes is the same in both cases, the difference between the results is a 2 cm difference in pipe length.

The results from these two test cases show that when the inner diameter of the inner pipe is decreased, the length of the pipes decreased slightly. This is a rather negligible difference that can be attributed to how the pipe lengths are calculated. The length of pipes are determined using Equation 3-10. This is done by first calculating the overall HTC using Equation 3-24 and the methodology outlined in Section 3.4. As shown in Figure 4-23 and Figure 4-24, the magnitude of the HTC of the cold side is significantly lower than that of the hot side. Therefore, the overall HTC is limited by the cold side, which remains at a constant hydraulic diameter.

In contrast, the results for HX-1 showed that the HTC of the fluids is similar throughout the HX, therefore neither the hot side nor cold side HTC is significantly limiting the overall HTC. Therefore, the results show that since changing the inner diameter of the inner pipe has no direct impact on the HTC of the cold side, it also has relatively no effect on the overall HTC. For this reason, this minute difference was deemed negligible.

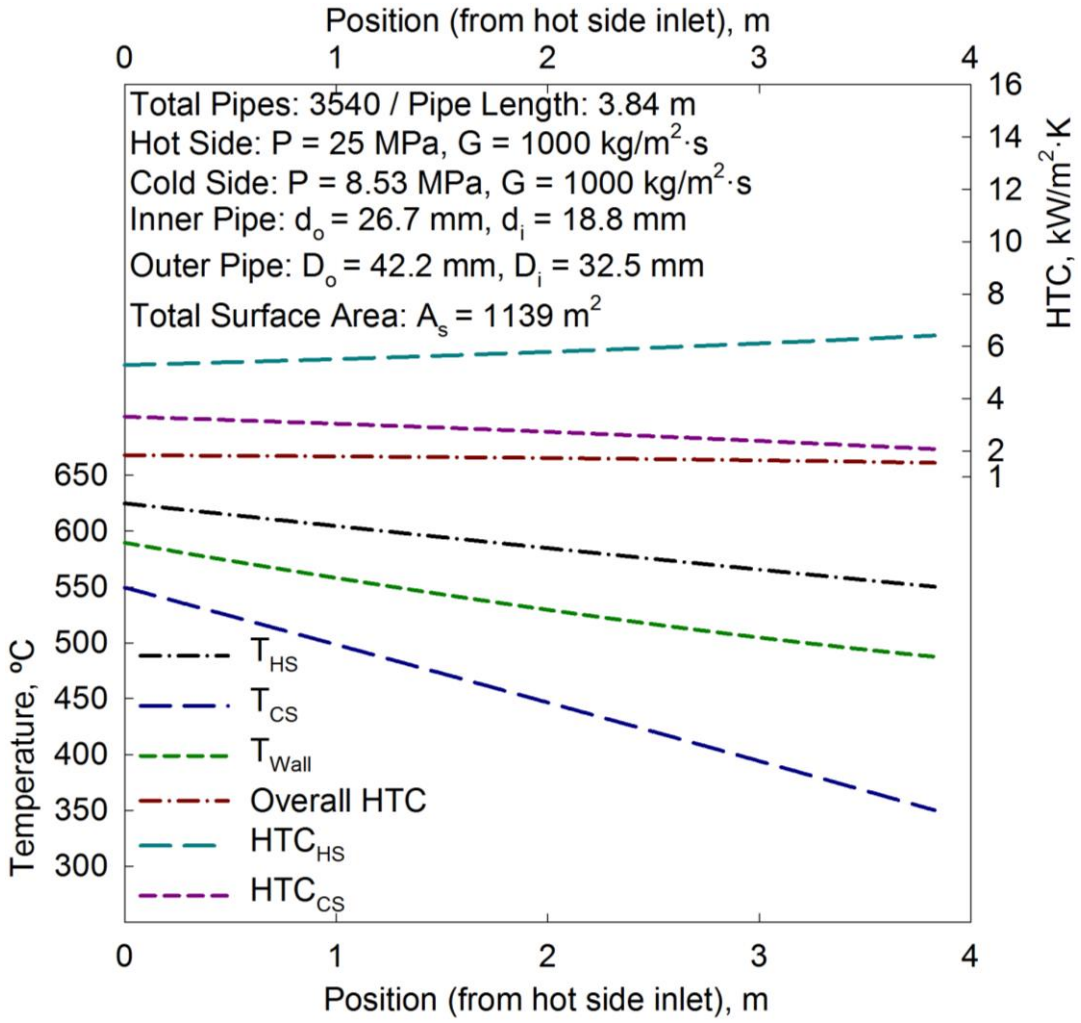

Figure 4-23. Test case #18 for HX-2: d_o = 18.8 mm. HTC and temperature profiles vs. position for the hot side and cold side.

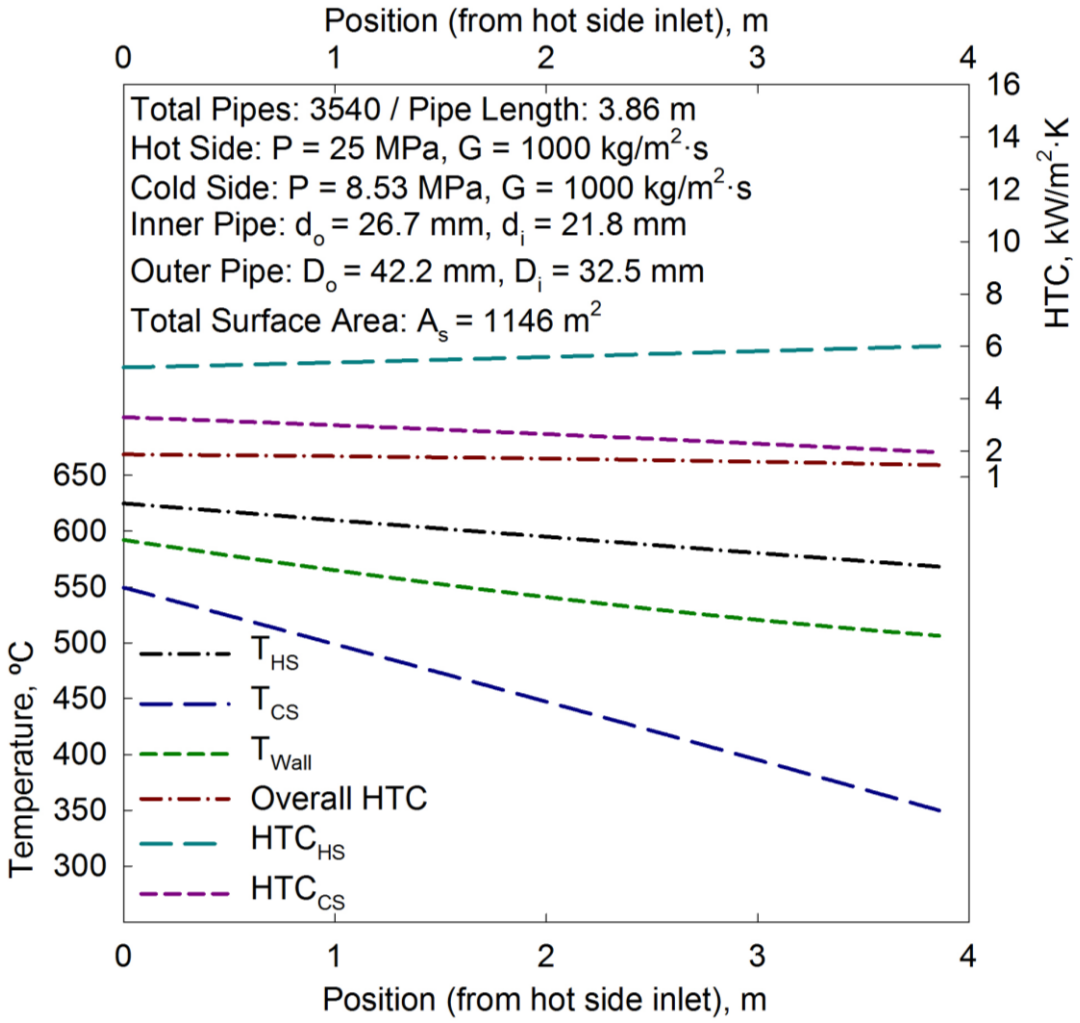

Figure 4-24. Test case #19 for HX-2: d_o = 21.8 mm. HTC and temperature profiles vs. position for the hot side and cold side.

Finally, for test case #20, the inner diameter of the inner pipe was set to 26.6 mm. Similar to what was done for HX-1, additional dimensions were changed to ensure that the HX complied with AMSE standards regarding minimum wall thickness. The piping dimensions used were identical to those from test case #10 for HX-1; these dimensions are discussed in Section 4.1.4. The results from test case #20 are shown in Figure 4-25. The number of pipes required was found to be 3605 and with a length of 3.07 m per pipe. The resultant total heat transfer surface area in this case was 1163 m^2. The hot side outlet temperature is 587^oC.

Comparing the results from test case #20 to test case #18 and #19 shows that while the inner diameter of the inner pipe is larger in test case #20, the total heat transfer surface area is smaller in the previous test cases. This is a result of the increase in all of the piping dimensions in the HX. These results are expected as they are similar to what was shown for HX-1. Therefore, while the pipes are shorter in test case #20, the total number of pipes required is larger, which increases the total heat transfer surface area.

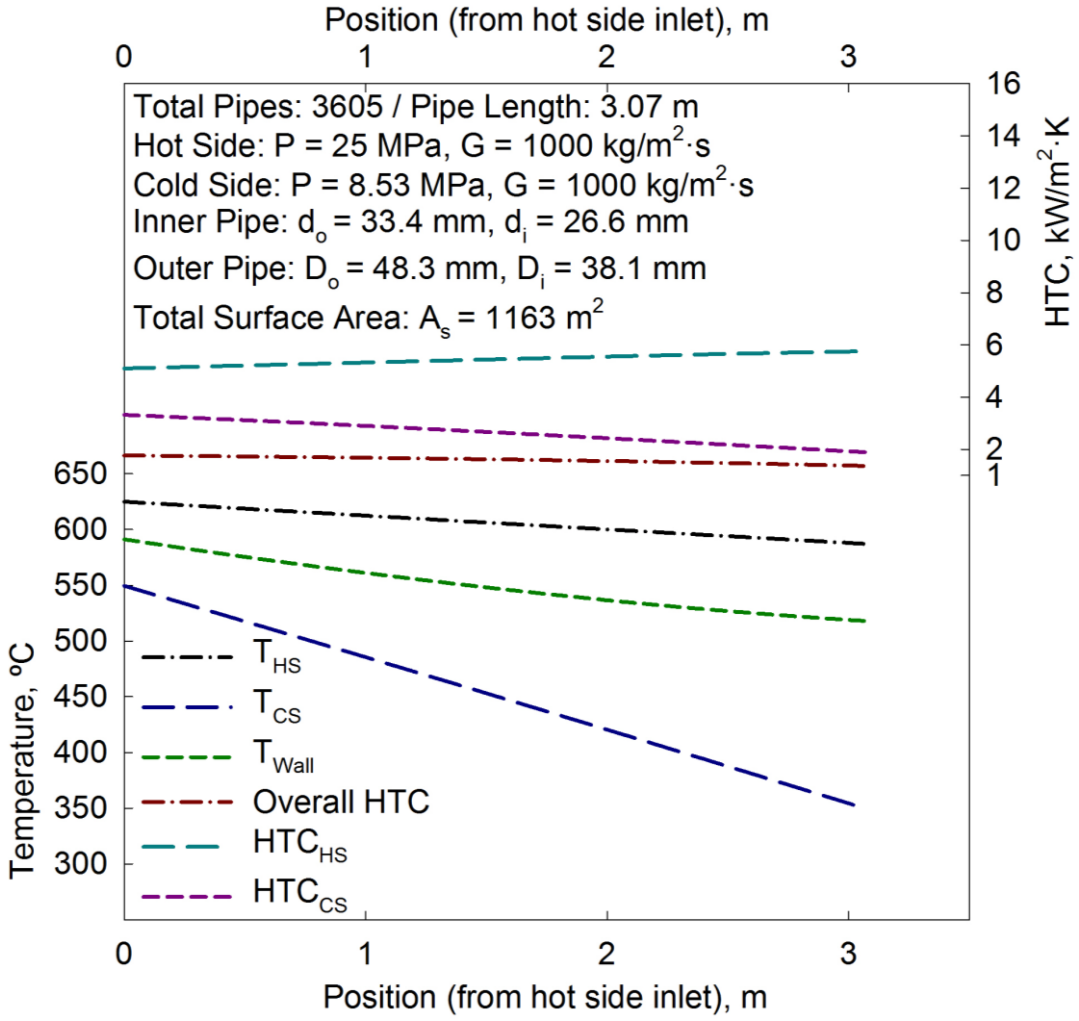

Figure 4-25. Test case #20 for HX-2: d_o = 26.6 mm. HTC and temperature profiles vs. position for the hot side and cold side.

Chapter 5. Concluding Remarks

This work assessed the performance of supercritical working fluids in an intermediate HX to be used for the production of hydrogen. The intermediate HX would be linked to a Canadian SCWR, where the coolant from the reactor would exchange its heat with the working fluid in the HX. The thermal energy requirements of the HX were based on the 4-step thermochemical Cu-Cl cycle, which was determined to be the most suitable hydrogen-production method due to its relatively low temperature requirement of approximately 530^{o}C.

A one-dimensional heat-transfer analysis was conducted on two reference cases. The first reference case was an SCW-to-SCW HX. The second reference case was an SCW-to-Supercritical CO_2 HX. These two HXs were referred to as HX-1 and HX-2, respectively. Based on the parameters of the reference case for HX-1, a total of 488 pipes with a length of 19.85 m per pipe are required to meet a thermal energy requirement of 224 MW_{th}. This amounted to a total heat transfer surface area of 811.76 m^2.

The reference case for HX-2 resulted in a total of 3540 pipes with a length of 3.85 m per pipe, amounting to a total heat transfer surface area of 1143.4 m^2. The results showed that pipe lengths were significantly shorter for HX-2 due to the lower specific heat of supercritical CO_2. This reduced the energy content of the fluid and resulted in a significant increase in the number of pipes required.

A series of additional test cases were also conducted to determine the effect various parameters had on the overall size of the HX. These additional test cases looked to determine the impact of mass flux, pressure and piping dimensions on the overall size of the HX.

Decreasing the mass flux on the cold side resulted in shorter pipe lengths but increased the number of pipes required, while increasing resulted in the opposite

effect. These trends were also observed in the test cases in which the mass flux on both the hot and cold side were varied.

It was also shown that varying the pressure on the cold side impacted the thermophysical properties of the fluids therein by affecting the overall size of the HX. In the case of HX-1 where the fluids would enter the pseudocritical region, it was shown that decreasing the pressure closer to the critical pressure also decreased the overall size of the HX. For HX-2, since neither fluid entered the pseudocritical region, the peaks associated with this region were not present. Therefore, the overall size of the HX decreased with a decrease in pressure and vice versa.

In HX-1 varying the inner diameter of the inner pipe had an impact on the size of the HX; however, this same change had a negligible effect in HX-2. For both HXs it was also shown that increasing the diameter of the inner pipe to 26.6 mm resulted in shorter pipes. The number of pipes increased, however, as the cross-sectional area of the cold side was also impacted in this test case.

It was shown that while various combinations of mass flux, pressure and piping dimensions can be implemented to optimize the design of the HX, the fluid used on the cold side would depend on the desired hydrogen production rate. In HX-1, the reference case showed that approximately 12% of a Canadian SCWRs total mass flow rate would need to be diverted from the reactor to meet a thermal energy requirement of 224 MW_{th}. In contrast, the reference case for HX-2 showed a much higher 92%.

Based on these results, it was determined that using supercritical CO_2 would not be feasible for a production rate of 1 kg/s. Therefore, unless a significantly smaller production rate is required, SCW would need to be used on the cold side as was done in HX-1 due to the increased energy content of the fluid.

Chapter 6. Future Work

Future work should consist of optimizing the operating conditions of the HX based on the work presented in this thesis. This should be done by moving towards a two-dimensional analysis or even a three-dimensional computation fluid dynamics model to get a better understanding of the fluids properties in the HX. The significance of the pseudocritical region and its impact on the overall size of the HX was shown throughout the various test cases. Therefore, a more sophisticated model would be required to better assess the complex phenomena associated with supercritical fluids. The results from this model could also be used to better approximate the size of the HX. Research could move towards a detailed design of the HX based on the requirements of the Cu-Cl cycle and a desired production rate.

The results showed that based on the selected HX design and operating conditions, supercritical CO_2 would not be feasible with a production rate of 1 kg/s. Therefore, future research should be conducted to determine the feasibility of the fluid at lower production rates. Additional analyses should also be conducted on a shell-and-tube HX. The benefits of a double-pipe HX were listed in this work, however, a shell-and-tube HX may bring about additional benefits or insights when combined with a relatively low-pressure fluid, such as supercritical CO_2. In this context, the operating conditions of the fluid can be optimized for supercritical CO_2 based on the work presented in this thesis. This can include increasing the mass flux of the fluid to minimize piping requirements.

In this work, the thermal conductivity and tensile strength of a few selected materials were assessed. This should be expanded with a more in-depth material analysis to analyze material stresses that may arise due to the operating conditions of the supercritical fluids. In addition, the impact of heat losses to the environment on the overall size of the HX should also be considered as a part of future studies.

References

[1] International Energy Agency, "World Energy Outlook," London, 2013.

[2] World Nuclear Association, "World Energy Needs and Nuclear Power," January 2015. [Online]. Available: http://www.world-nuclear.org/info/Current-and-Future-Generation/World-Energy-Needs-and-Nuclear-Power/. [Accessed 17 March 2015].

[3] World Nuclear Association, "Nuclear Power in the World Today," February 2015. [Online]. Available: http://www.world-nuclear.org/info/Current-and-Future-Generation/Nuclear-Power-in-the-World-Today/. [Accessed 17 March 2015].

[4] J.-L. Bourdages and M. Zakzouk, "Nuclear Energy: Challenges and Opportunities," *41st Parliament Current and Emerging Issues,* pp. 60-61, June 2011.

[5] Generation IV International Forum, "GIF R&D Outlook for Generation IV Nuclear Energy Systems," 2009.

[6] I. L. Pioro and R. B. Duffey, Heat Transfer and Hydraulic Resistance at Supercritical Pressures in Power Engineering Applications, New York: ASME Press, 2007.

[7] J. M. H. Levelt Sengers, "Supercritical fluid: Their properties and applications," in *Supercritical Fluids*, Springer Netherlands, 2000, pp. 1-29.

[8] E. Schmidt, E. Eckert and V. Grigull, Heat Transfer by Liquids Near the Critical State, Dayton: Wright Field, Air Material Command, 1946.

[9] L. S. Pioro and I. L. Pioro, Industrial Two-Phase Thermosyphons, New York: Begell House Inc., 1997.

[10] E. W. Lemmon, M. L. Huber and M. O. McLinden, *NIST Standard Reference Database 23: Reference Fluid Thermodynamic and Transport Properties-REFPROP, Version 8.0, National Institute of Standards and Technology, Standard Reference Data Program,* Gaithersburg, 2007.

[11] Generation IV International Forum, "GIF Annual Report," 2013.

[12] M. Yetisir, M. Gaudet and D. Rhodes, "Development and integration of Canadian-SCWR concept with counter-flow fuel assembly," in *6th International Symposium on Supercritical Water-cooled Reactors*, Shenzhen, Guangdong, 2013.

[13] G. Naterer et al., "Recent Canadian advances in nuclear-based hydrogen production and the thermochemical Cu-Cl cycle," *International Journal of Hydrogen Energy,* vol. 34, no. 7, pp. 2901-2917, 2009.

[14] J. P. Bennet, "Chapter 1. Issues in hydrogen production using gasification," in *Materials for the Hydrogen Economy*, Boca Raton, FL, CRC Press, 2008, pp. 1-36.

[15] U.S. Department of Energy, "Hydrogen Production: Natural Gas Reforming," [Online]. Available: http://energy.gov/eere/fuelcells/hydrogen-production-natural-gas-reforming. [Accessed 30 April 2015].

[16] V. N. Balashov et al, "CuCl electrolysis for hydrogen production in the Cu-Cl thermochemical cycle," *Journal of The Electrochemical Society,* vol. 158, no. 3, pp. B266-B275, 2011.

[17] B. W. McQuillan et al, "High efficiency generation of hydrogen fuels using solar thermochemical spltting of water," General Atomics, San Diego, CA, 2002.

[18] M. Lewis and A. Taylor, "High temperature thermochemical processes," DOE Hydrogen Program, Washington D.C., pp. 182-185, 2006.

[19] G. F. Naterer et al, "Progress of international hydrogen production network for the thermochemical Cu-Cl cycle," *International Journal of Hydrogen Energy,* vol. 38, no. 2, pp. 740-759, 2013.

[20] M. Sakurai et al, "Experimental study on side-reaction occurance condition in the iodine-sulfur thermochemical hydrogen production process," *International Journal of Hydrogen Energy,* vol. 25, no. 7, pp. 613-619, 2000.

[21] K. Schultz, "Thermochemical production of hydrogen from solar and nuclear energy," General Atomics, San Diego, CA, 2003.

[22] M. A. Lewis et al, "Development of the low temperature Cu-Cl thermochemical cycle," in *International Congress on Advances in Nuclear Power Plants*, Seoul, Korea, 2005.

[23] Z. L. Wang et al, "Comparison of different copper-chlorine thermochemical cycles for hydrogen production," *International Journal of Hydrogen Energy,* vol. 34, no. 8, pp. 3267-3276, 2009.

[24] Z. L. Wang et al, "Comparison of sulfur-iodine and copper-chlorine thermochemical hydrogen production cycles," *International Journal of Hydrogen Energy,* vol. 35, no. 10, pp. 4820-4830, 2010.

[25] Z. Wang et al, "Thermal integration of SCWR nuclear and thermochemical hydrogen plants," in *Proc. Canada-China Joint Workshop on Supercritcal Water-cooled Reactors '10*, Toronto, ON, April 25-28, 2010.

[26] R. J. Ribando, G. W. O'Leary and S. Carlson-Skalak, "General numerical scheme for heat exchanger thermal analysis and design," *Computer Applications in Engineering Education,* vol. 5, no. 4, pp. 231-242, 1997.

[27] A. Lukomski, I. Pioro and K. Gabriel, "Hydrogen production using process heat from an SCW NPP via double-pipe heat exchanger," in *5th International Symposium on Supercritical Water-cooled Reactors*, Vancouver, BC, 2011.

[28] Generation IV International Forum, "A Technology Roadmap for Generation IV Nuclear Energy Systems," 2002.

[29] D. F. Wang and S. Wang, "A preliminary CATHENA thermalhydraulic model of the Canadian SCWR for safety analysis," *AECL Nuclear Review,* pp. 9-16, June 2014.

[30] Generation IV International Forum, "Technology Roadmap Update for Generation IV Nuclear Energy Systems," 2014.

[31] H. F. Khartabil et al., "The pressure-tube concept of generation IV supercritical water-cooled reactors (SCWRs): Overview and status," in *Proc. International Congress on Advances in Nuclear Power Plants `05*, Seoul, Korea, May, 2005.

[32] M. Naidin et al, "Thermodynamic analysis of SCW NPP cycles with thermo-chemical co-generation of hydrogen," in *Proc. International Conference on Hydrogen Production '09*, Oshawa, ON, Canada, 2009.

[33] I. Pioro et al, "Supercritical water-cooled nuclear reactors: NPP layouts and thermal design options of pressure channels," in *Proc. Pacific Basin Nuclear Conference '10*, Cancun, Mexico, October, 2010.

[34] I. Pioro and S. Mokry, "Thermophysical properties at critical and supercritical conditions," in *Heat Transfer - Theoretical Analysis, Experimental Investigations and Industrial Systems*, Shanghai, China, InTech, 2011, pp. 573-592.

[35] S. Gupta et al, "Developing empirical heat-transfer correlations for supercritical CO2 flowing in vertical bare tubes," *Nuclear Engineering and Design,* vol. 261, pp. 116-131, 2013.

[36] X. Cheng, X. J. Liu and H. Y. Gu, "Fluid-to-fluid scaling of heat transfer in circular tubes cooled with supercritical fluids," *Nuclear Engineering and Design,* vol. 241, no. 2, pp. 498-508, 2011.

[37] F. P. Incropera et al., Fundamentals of Heat and Mass Transfer, Hoboken, NJ: John Wiley & Sons, Inc., 2007.

[38] N. M. Schnurr, V. S. Sastry and A. B. Shapiro, "A numerical analysis of heat transfer to fluids near the thermodynamic critical point including thermal entrance region," *Journal of Heat Transfer,* vol. 98, no. 4, pp. 609-615, 1976.

[39] A. A. Bishop, R. O. Sandberg and L. S. Tong, "Forced convection heat transfer to water at near-critical temperatures and super-critical pressures," Atomic Power Division, Westinghouse Electric Corporation, Pittsburgh, PA, 1964.

[40] S. Mokry, "Development of a Heat-Transfer Correlation for Supercritical Water in Supercritical Water-cooled Reactor Applications," UOIT, Oshawa, ON, 2009.

[41] H. S. Swenson, J. R. Carver and C. R. Kakarala, "Heat transfer to supercritical water in smooth-bare tubes," *Journal of Heat Transfer,* vol. 87, no. 4, 1965.

[42] H. Zahlan, D. C. Groeneveld and S. Tavoularis, "Look-up for trans-critical heat transfer," in *Proc. Canada-China Joint Workshop on Supercritical Water-cooled Reactors '10*, Toronto, ON, April 25-28, 2010.

[43] S. Gupta et al., "Developing new heat-transfer correlation for supercritical-water flow," in *International Conference on Nuclear Engineering '10*, Xi'an, China, 2010.

[44] G. F. Hewitt, "Part 3: Thermal and Hydraulic Design of Heat Exchangers," in *Heat Exchanger Design Handbook 2008*, Redding, CT, Begell House Inc., 2008.

[45] H. Thind, "Heat-Transfer Analysis of Double-Pipe Heat Exchangers for Indirect-Cycle SCW NPP," UOIT, Oshawa, ON, 2012.

[46] R. B. Duffey and K. Hedges, "Future CANDU reactor development," in *Proc. International Conference on Nuclear Engineering '99*, Tokyo, Japan, 1999.

[47] "MatWeb: Material Property Data," [Online]. Available: http://www.matweb.com/index.aspx.. [Accessed 15 06 2015].

[48] British Stainless Steel Association, "Elevated temperature physical properties of stainless steels," [Online]. Available: http://www.bssa.org.uk/topics.php?article=139.. [Accessed 15 06 2015].

[49] M. Richards, A. Shenoy and K. Schultz et al., "Conceptual designs based on the sulphur-iodine process and high-temperature electrolysis," *International Journal of Nuclear Hydrogen Production and Applications,* vol. 1, no. 1, pp. 36-50, 2006.

[50] R. K. Shah and D. P. Sekulic, Fundamentals of Heat Exchanger Design, Hoboken, NJ: John Wiley & Sons, Inc., 2003.

Appendix A: MATLAB Script

```
%%%%%%%%%%%%%%%%%%%%%%%%%%%%%%%%%%%%%%%%%%%%%%%%%%%%%%%%%%%%%%%%%%%%%%%%%%%%%%%%
%
% MATLAB Script for Double-tube Counter Flow Heat Exchanger (HX) design
%
% HX Design used to link SCWR to Hydrogen Co-Generation Plant
%
% HX Design based on No-Reheat Cycle
%
% Inner Tube (Hot Side) = SCW Reactor Coolant
%
% Outer Tube (Cold Side) = SCW Working Fluid
%
%%%%%%%%%%%%%%%%%%%%%%%%%%%%%%%%%%%%%%%%%%%%%%%%%%%%%%%%%%%%%%%%%%%%%%%%%%%%%%%%
%

tic

clear all;
clc

%%%%%%%%%%%%%%%%%%%%%%%%%%%%%%%%%%%%%%%%%%%%%%%%%%%%%%%%%%%%%%%%%%%%%%%%%%%%%%%%
%
%%%%%%%%%%%%%%%%%%%%%%%%%%%%%%%%%%%%%%%%%%%%%%%%%%%%%%%%%%%%%%%%%%%%%%%%%%%%%%%%
%
%                               NIST PROPERTIES
%
%%%%%%%%%%%%%%%%%%%%%%%%%%%%%%%%%%%%%%%%%%%%%%%%%%%%%%%%%%%%%%%%%%%%%%%%%%%%%%%%
%
%%%%%%%%%%%%%%%%%%%%%%%%%%%%%%%%%%%%%%%%%%%%%%%%%%%%%%%%%%%%%%%%%%%%%%%%%%%%%%%%
%

% P   Pressure [kPa]
% T   Temperature [K]
% D   Density [kg/m3]
% H   Enthalpy [J/kg]
% S   Entropy [J/(kg/K)]
% U   Internal energy [J/kg]
% C   Cp [J/(kg K)]
% O   Cv [J/(kg K)]
% K   Ratio of specific heats (Cp/Cv) [-]
% A   Speed of sound [m/s]
% X   liquid phase and gas phase composition (mass fractions)
% V   Dynamic viscosity [Pa*s]
% L   Thermal conductivity [W/(m K)]
% Q   Quality (vapor fraction) (kg/kg)
% I   Surface tension [N/m]

% The Working Fluids Used in the HX
inner_tube_fluid = 'water';  % Hot Side fluid
outer_tube_fluid = 'water';  % Cold Side fluid
```

```
%%%%%%%%%%%%%%%%%%%%%%%%%%%%%%%%%%%%%%%%%%%%%%%%%%%%%%%%%%%%%%%%%%%%%%%%%%%%%%%%
%
%%%%%%%%%%%%%%%%%%%%%%%%%%%%%%%%%%%%%%%%%%%%%%%%%%%%%%%%%%%%%%%%%%%%%%%%%%%%%%%%
%
%                        ENERGY REQUIREMENTS FOR THE HX
%
%%%%%%%%%%%%%%%%%%%%%%%%%%%%%%%%%%%%%%%%%%%%%%%%%%%%%%%%%%%%%%%%%%%%%%%%%%%%%%%%
%
%%%%%%%%%%%%%%%%%%%%%%%%%%%%%%%%%%%%%%%%%%%%%%%%%%%%%%%%%%%%%%%%%%%%%%%%%%%%%%%%
%

% Net Thermal Energy Requirement for the 4-step Cu-Cl cycle
EnergyReq = 224 * 10^6;  % Energy Requirement (W)

%%%%%%%%%%%%%%%%%%%%%%%%%%%%%%%%%%%%%%%%%%%%%%%%%%%%%%%%%%%%%%%%%%%%%%%%%%%%%%%%
%
%%%%%%%%%%%%%%%%%%%%%%%%%%%%%%%%%%%%%%%%%%%%%%%%%%%%%%%%%%%%%%%%%%%%%%%%%%%%%%%%
%
%                   TUBE DIMENSIONS AND MATERIAL PROPERTIES
%
%%%%%%%%%%%%%%%%%%%%%%%%%%%%%%%%%%%%%%%%%%%%%%%%%%%%%%%%%%%%%%%%%%%%%%%%%%%%%%%%
%
%%%%%%%%%%%%%%%%%%%%%%%%%%%%%%%%%%%%%%%%%%%%%%%%%%%%%%%%%%%%%%%%%%%%%%%%%%%%%%%%
%

% Selected tube Material for Inner and Outer Tube is Stainless Steel 304
S = 305 * 1000;  % Tensile Strength of SS-304 at 650 degC (kPa)

% Inner Tube (Hot Side) Dimensions
d_o = 26.67 / 1000;  % Outer Diameter of the Inner Tube (m)
inner_tube_thick = 2.870 / 1000;  % Wall Thickness of Inner Tube (m)
d_i = d_o - (2 * inner_tube_thick);  % Inner Diameter of the Inner Tube
(m)

Ac_inner_tube = (pi/4) * (d_i^2);  % Cross-sectional Area of the Inner
Tube (m^2)

% Outer tube (Cold Side) Dimensions
D_o = 42.16 / 1000;  % Outer Diameter of the Outer Tube (m)
outer_tube_thick = 4.851 / 1000;  % Wall Thickness of Outer Tube (m)
D_i = D_o - (2 * outer_tube_thick);  % Inner Diameter of the Outer Tube
(m)

Ac_outer_tube = (pi / 4) *((D_i^2) - (d_o^2));  % Cross-sectional Area of
the Outer Tube (m^2)

D_h = D_i - d_o;  % Hydraulic Diamter of the Outer Tube (m)

%%%%%%%%%%%%%%%%%%%%%%%%%%%%%%%%%%%%%%%%%%%%%%%%%%%%%%%%%%%%%%%%%%%%%%%%%%%%%%%%
%
%%%%%%%%%%%%%%%%%%%%%%%%%%%%%%%%%%%%%%%%%%%%%%%%%%%%%%%%%%%%%%%%%%%%%%%%%%%%%%%%
%
%                               FLUID PARAMETERS
%
```

```
%%%%%%%%%%%%%%%%%%%%%%%%%%%%%%%%%%%%%%%%%%%%%%%%%%%%%%%%%%%%%%%%%%%%%%%%%%%%%%%%
%
%%%%%%%%%%%%%%%%%%%%%%%%%%%%%%%%%%%%%%%%%%%%%%%%%%%%%%%%%%%%%%%%%%%%%%%%%%%%%%%%
%

% Inner Tube (Hot Side) = SCW Reactor Coolant Parameters
P_hot_in = 25 * 1000;  % Pressure of the Hot Side Fluid (kPa)
T_hot_in = 625 + 273.15;  % Inlet Temperature of Hot Side (K)
mass_flux_tube_h = 1000;  % Mass Flux per Tube (Hot Side) (kg/(m^2*s))

% Mass Flow Rate (Hot Side) (kg/s)
mass_flow_rate_tube_h = mass_flux_tube_h * Ac_inner_tube;

% Outer Tube (Cold Side) = SCW Working Fluid Parameters
P_cold_in = 25.5 * 1000;  % Pressure of the Cold Side Fluid (kPa)
T_cold_in = 350 + 273.15;  % Inlet Temperature of Cold Side (K)
T_cold_out = 550 + 273.15;  % Outlet Temperature of Cold Side (K)
mass_flux_tube_c = 1000;  % Mass Flux per Tube (cold side) (kg/(m^2*s))

% Mass Flow Rate (Cold Side) (kg/s)
mass_flow_rate_tube_c = mass_flux_tube_c * Ac_outer_tube;

%%%%%%%%%%%%%%%%%%%%%%%%%%%%%%%%%%%%%%%%%%%%%%%%%%%%%%%%%%%%%%%%%%%%%%%%%%%%%%%%
%
%%%%%%%%%%%%%%%%%%%%%%%%%%%%%%%%%%%%%%%%%%%%%%%%%%%%%%%%%%%%%%%%%%%%%%%%%%%%%%%%
%
%                       APPROXIMATING THE SIZE OF THE HX
%
%%%%%%%%%%%%%%%%%%%%%%%%%%%%%%%%%%%%%%%%%%%%%%%%%%%%%%%%%%%%%%%%%%%%%%%%%%%%%%%%
%
%%%%%%%%%%%%%%%%%%%%%%%%%%%%%%%%%%%%%%%%%%%%%%%%%%%%%%%%%%%%%%%%%%%%%%%%%%%%%%%%
%

n = 5000;

% Change in Enthalpy Across the Length of the Tube (Cold Side)
temp_cold_b = linspace(T_cold_in, T_cold_out, n);

entha_cold_b = zeros(size(n));
entha_cold_b(1) =
refpropm('H','T',temp_cold_b(1),'P',P_cold_in,outer_tube_fluid);

delta_h_cold = zeros(size(n-1));

for i = 2:n

entha_cold_b(i) =
refpropm('H','T',temp_cold_b(i),'P',P_cold_in,outer_tube_fluid);
delta_h_cold(i) = entha_cold_b(i) - entha_cold_b(i-1);

end

% Total Rate of Heat Transfer in the Tube (Cold Side)
q_total_tube_c = mass_flow_rate_tube_c * sum(delta_h_cold);
```

```
% Outlet Temperature (Hot Side) Based on Rate of Heat Transfer in the Tube
en_hot_outlet = (-q_total_tube_c / mass_flow_rate_tube_h) +
(refpropm('H','T',T_hot_in,'P',P_hot_in,inner_tube_fluid));

T_hot_out = refpropm('T','H',en_hot_outlet,'P',P_hot_in,inner_tube_fluid);

% Change in Enthalpy Across the Length of the Tube (Hot Side)
temp_hot_b = linspace(T_hot_in, T_hot_out, n);

entha_hot_b = zeros(size(n));
entha_hot_b(1) =
refpropm('H','T',temp_hot_b(1),'P',P_hot_in,inner_tube_fluid);

delta_h_hot = zeros(size(n-1));

for i = 2:n

entha_hot_b(i) =
refpropm('H','T',temp_hot_b(i),'P',P_hot_in,inner_tube_fluid);
delta_h_hot(i) = entha_hot_b(i) - entha_hot_b(i-1);

end

% Total Rate of Heat Transfer in the Tube (Hot Side)
q_total_tube_h = mass_flow_rate_tube_h * sum(delta_h_hot);

% Number of tubes Required to Produce H2 at a Rate of 1 kg/s
No_tubes = ceil(EnergyReq / -q_total_tube_h);

% Total Mass Flow Rate in the HX (Hot Side)
mass_flow_rate_total_h = mass_flow_rate_tube_h * No_tubes;

% Total Mass Flow rate in the HX (Cold Side)
mass_flow_rate_total_c = mass_flow_rate_tube_c * No_tubes;

%%%%
%%%%

m = 5000;

temp_hot_b = linspace(T_hot_in, T_hot_out, m);
temp_cold_b = linspace(T_cold_out, T_cold_in, m);

temp_wall_initial = temp_hot_b - 5;

density_hot_b = zeros;
density_hot_w = zeros;

viscosity_hot_b = zeros;
viscosity_hot_w = zeros;

enthalpy_hot_b = zeros;
```

```
enthalpy_hot_w = zeros;

thermal_cond_hot_b = zeros;
thermal_cond_hot_w = zeros;

specific_heat_hot_b = zeros;
specific_heat_hot_w = zeros;

avg_specific_heat_hot = zeros;

re_number_hot = zeros;
re_number_hot_w = zeros;

prandtl_num_hot = zeros;
prandtl_num_hot_w = zeros;

nu_number_mokry_hot = zeros;
nu_number_swenson_hot = zeros;
nu_number_bishop_hot = zeros;
nu_number_dittus_hot = zeros;

htc_hot_mokry = zeros;
htc_hot_swenson = zeros;
htc_hot_bishop = zeros;
htc_hot_dittus = zeros;

thermal_cond_tube = zeros;

density_cold_b = zeros;
density_cold_w = zeros;

viscosity_cold_b = zeros;
viscosity_cold_w = zeros;

enthalpy_cold_b = zeros;
enthalpy_cold_w = zeros;

thermal_cond_cold_b = zeros;
thermal_cond_cold_w = zeros;

specific_heat_cold_b = zeros;
specific_heat_cold_w = zeros;

avg_specific_heat_cold = zeros;

re_number_cold = zeros;
re_number_cold_w = zeros;

prandtl_num_cold = zeros;
prandtl_num_cold_w = zeros;

nu_number_mokry_cold = zeros;
nu_number_swenson_cold = zeros;
```

```
nu_number_bishop_cold = zeros;
nu_number_dittus_cold = zeros;

htc_cold_mokry = zeros;
htc_cold_swenson = zeros;
htc_cold_bishop = zeros;
htc_cold_dittus = zeros;

thermal_resistance_hot = zeros;
thermal_resistance_cold = zeros;
thermal_resistance_tube = zeros;
t_wall_initial = zeros;

for j = 1:m

    delta_temp = 1;

    while abs(delta_temp) > 0.3

    % Fluid properties - Bulk (Hot Side)
    density_hot_b(j) =
refpropm('D','T',temp_hot_b(j),'P',P_hot_in,inner_tube_fluid);
    viscosity_hot_b(j) =
refpropm('V','T',temp_hot_b(j),'P',P_hot_in,inner_tube_fluid);
    enthalpy_hot_b(j) =
refpropm('H','T',temp_hot_b(j),'P',P_hot_in,inner_tube_fluid);
    thermal_cond_hot_b(j) =
refpropm('L','T',temp_hot_b(j),'P',P_hot_in,inner_tube_fluid);
    specific_heat_hot_b(j) =
refpropm('C','T',temp_hot_b(j),'P',P_hot_in,inner_tube_fluid);

    % Fluid properties - Wall (Hot Side)
    density_hot_w(j) =
refpropm('D','T',temp_wall_initial(j),'P',P_hot_in,inner_tube_fluid);
    viscosity_hot_w(j) =
refpropm('V','T',temp_wall_initial(j),'P',P_hot_in,inner_tube_fluid);
    enthalpy_hot_w(j) =
refpropm('H','T',temp_wall_initial(j),'P',P_hot_in,inner_tube_fluid);
    thermal_cond_hot_w(j) =
refpropm('L','T',temp_wall_initial(j),'P',P_hot_in,inner_tube_fluid);
    specific_heat_hot_w(j) =
refpropm('C','T',temp_wall_initial(j),'P',P_hot_in,inner_tube_fluid);

    % Calculations to Determine Heat Transfer Coefficient (Hot Side)
    avg_specific_heat_hot(j) = (enthalpy_hot_w(j) - enthalpy_hot_b(j)) /
(temp_wall_initial(j) - temp_hot_b(j));

    re_number_hot(j) = (d_i * mass_flux_tube_h) / viscosity_hot_b(j);
    re_number_hot_w(j) = (d_i * mass_flux_tube_h) / viscosity_hot_w(j);

    prandtl_num_hot(j) = (viscosity_hot_b(j) * avg_specific_heat_hot(j)) /
(thermal_cond_hot_b(j));
    prandtl_num_hot_w(j) = (viscosity_hot_w(j) * avg_specific_heat_hot(j))
/ (thermal_cond_hot_w(j));
```

```
    nu_number_mokry_hot(j) = 0.0061 * (re_number_hot(j)^0.904) *
(prandtl_num_hot(j)^0.684) * ((density_hot_w(j) /
density_hot_b(j))^0.564);
    nu_number_swenson_hot(j) = 0.00459 * (re_number_hot_w(j)^0.923) *
(prandtl_num_hot_w(j)^0.613) * ((density_hot_w(j) /
density_hot_b(j))^0.231);
    nu_number_bishop_hot(j) = 0.0069 * (re_number_hot(j)^0.9) *
(prandtl_num_hot(j)^0.66) * ((density_hot_w(j) / density_hot_b(j))^0.43);
    nu_number_dittus_hot(j) = 0.023 * (re_number_hot(j)^0.8) *
(prandtl_num_hot(j)^0.4);

    htc_hot_mokry(j) = (nu_number_mokry_hot(j) * thermal_cond_hot_b(j)) /
d_i;
    htc_hot_swenson(j) = (nu_number_swenson_hot(j) *
thermal_cond_hot_w(j)) / d_i;
    htc_hot_bishop(j) = (nu_number_bishop_hot(j) * thermal_cond_hot_b(j))
/ d_i;
    htc_hot_dittus(j) = (nu_number_dittus_hot(j) * thermal_cond_hot_b(j))
/ d_i;

    thermal_cond_tube(j) = 0.00000002 * (temp_wall_initial(j))^3 - 0.00004
* (temp_wall_initial(j))^2 + 0.0398 * (temp_wall_initial(j)) + 5.728;

    % Fluid properties - Bulk (Cold Side)
    density_cold_b(j) =
refpropm('D','T',temp_cold_b(j),'P',P_cold_in,outer_tube_fluid);
    viscosity_cold_b(j) =
refpropm('V','T',temp_cold_b(j),'P',P_cold_in,outer_tube_fluid);
    enthalpy_cold_b(j) =
refpropm('H','T',temp_cold_b(j),'P',P_cold_in,outer_tube_fluid);
    thermal_cond_cold_b(j) =
refpropm('L','T',temp_cold_b(j),'P',P_cold_in,outer_tube_fluid);
    specific_heat_cold_b(j) =
refpropm('C','T',temp_cold_b(j),'P',P_cold_in,outer_tube_fluid);

    % Fluid properties - Wall (Cold Side)
    density_cold_w(j) =
refpropm('D','T',temp_wall_initial(j),'P',P_cold_in,outer_tube_fluid);
    viscosity_cold_w(j) =
refpropm('V','T',temp_wall_initial(j),'P',P_cold_in,outer_tube_fluid);
    enthalpy_cold_w(j) =
refpropm('H','T',temp_wall_initial(j),'P',P_cold_in,outer_tube_fluid);
    thermal_cond_cold_w(j) =
refpropm('L','T',temp_wall_initial(j),'P',P_cold_in,outer_tube_fluid);
    specific_heat_cold_w(j) =
refpropm('C','T',temp_wall_initial(j),'P',P_cold_in,outer_tube_fluid);

    % Calculations to Determine Heat Transfer Coefficient (Cold Side)
    avg_specific_heat_cold(j) = (enthalpy_cold_w(j) - enthalpy_cold_b(j))
/ (temp_wall_initial(j) - temp_cold_b(j));

    re_number_cold(j) = (D_h * mass_flux_tube_c) / viscosity_cold_b(j);
    re_number_cold_w(j) = (D_h * mass_flux_tube_c) / viscosity_cold_w(j);
```

```
    prandtl_num_cold(j) = (viscosity_cold_b(j) *
avg_specific_heat_cold(j)) / (thermal_cond_cold_b(j));
    prandtl_num_cold_w(j) = (viscosity_cold_w(j) *
avg_specific_heat_cold(j)) / (thermal_cond_cold_w(j));

    nu_number_mokry_cold(j) = 0.0061 * (re_number_cold(j)^0.904) *
(prandtl_num_cold(j)^0.684) * ((density_cold_w(j) /
density_cold_b(j))^0.564);
    nu_number_swenson_cold(j) = 0.00459 * (re_number_cold_w(j)^0.923) *
(prandtl_num_cold_w(j)^0.613) * ((density_cold_w(j) /
density_cold_b(j))^0.231);
    nu_number_bishop_cold(j) = 0.0069 * (re_number_cold(j)^0.9) *
(prandtl_num_cold(j)^0.66) * ((density_cold_w(j) /
density_cold_b(j))^0.43);
    nu_number_dittus_cold(j) = 0.023 * (re_number_cold(j)^0.8) *
(prandtl_num_cold(j)^0.4);

    htc_cold_mokry(j) = (nu_number_mokry_cold(j) * thermal_cond_cold_b(j))
/ D_h;
    htc_cold_swenson(j) = (nu_number_swenson_cold(j) *
thermal_cond_cold_w(j)) / D_h;
    htc_cold_bishop(j) = (nu_number_bishop_cold(j) *
thermal_cond_cold_b(j)) / D_h;
    htc_cold_dittus(j) = (nu_number_dittus_cold(j) *
thermal_cond_cold_b(j)) / D_h;

    % Thermal Resistance Calculations
    thermal_resistance_hot(j) = (1/htc_hot_mokry(j));
    thermal_resistance_cold(j) = (d_i / (d_o * htc_cold_mokry(j)));
    thermal_resistance_tube(j) = (d_i * log(d_o / d_i)) / (2 *
thermal_cond_tube(j));

    % Calculating the Wall Temperature of the tube
    t_wall_initial(j) = (((temp_hot_b(j) / thermal_resistance_hot(j)) +
(temp_cold_b(j) / thermal_resistance_cold(j))) / ((1 /
thermal_resistance_hot(j)) + (1 / thermal_resistance_cold(j))));


    delta_temp = t_wall_initial(j) - temp_wall_initial(j);


    if delta_temp > 0.3
        temp_wall_initial(j) = temp_wall_initial(j) + abs(delta_temp)/2;
    end

    if delta_temp < -0.3
        temp_wall_initial(j) = temp_wall_initial(j) - abs(delta_temp)/2;
    end

    end
end

% Calculating the Overall Heat Transfer Coefficient (U)
U = mean(1 / (thermal_resistance_hot(j) + thermal_resistance_tube(j) +
thermal_resistance_cold(j)));
```

```
% Log Mean Temperature Difference (LMTD) Calculation
delta_T1 = T_hot_in - T_cold_out;
delta_T2 = T_hot_out - T_cold_in;

LMTD = ((delta_T1 - delta_T2) / (log(delta_T1/delta_T2)));

tube_surface_area = abs((q_total_tube_h) / (LMTD * (U)));

tube_length = tube_surface_area / (pi * d_o);

%%%%%%%%%%%%%%%%%%%%%%%%%%%%%%%%%%%%%%%%%%%%%%%%%%%%%%%%%%%%%%%%%%%%%%%%%%%%%%%
%
%%%%%%%%%%%%%%%%%%%%%%%%%%%%%%%%%%%%%%%%%%%%%%%%%%%%%%%%%%%%%%%%%%%%%%%%%%%%%%%
%
%                    DETERMINING THE TEMPERATURE PROFILES
%
%%%%%%%%%%%%%%%%%%%%%%%%%%%%%%%%%%%%%%%%%%%%%%%%%%%%%%%%%%%%%%%%%%%%%%%%%%%%%%%
%
%%%%%%%%%%%%%%%%%%%%%%%%%%%%%%%%%%%%%%%%%%%%%%%%%%%%%%%%%%%%%%%%%%%%%%%%%%%%%%%
%

node_length = 0.01;
check = true;

% Temperature Profiles for the Hot Side
TEMP_hot_in(1) = T_hot_in;

i = 1;
h_hot_b = zeros;
TEMP_hot_b = zeros;

x = 0;

enthalpy_drop_increment_h = (sum(delta_h_hot) / tube_length) *
node_length;

h_hot_b_in =
refpropm('H','T',TEMP_hot_in(i),'P',P_hot_in,inner_tube_fluid);
h_hot_b(i) =  enthalpy_drop_increment_h + h_hot_b_in;

TEMP_hot_b(i) =
refpropm('T','H',h_hot_b(i),'P',P_hot_in,inner_tube_fluid);

while (check == true)

    x = x + node_length;
    if x > tube_length
        h_hot_b_out = enthalpy_drop_increment_h + h_hot_b(i);
        TEMP_hot_out =
refpropm('T','H',h_hot_b_out,'P',P_hot_in,inner_tube_fluid);
        break;
    end
```

```
    i = i + 1;
    h_hot_b(i) = enthalpy_drop_increment_h + h_hot_b(i-1);
    TEMP_hot_b(i) =
refpropm('T','H',h_hot_b(i),'P',P_hot_in,inner_tube_fluid);

end

% Temperature Profiles for the Cold Side
TEMP_cold_in(1) = T_cold_out;

i = 1;
h_cold_b = zeros;
TEMP_cold_b = zeros;

x = 0;

enthalpy_rise_increment_c = ((-sum(delta_h_cold)) / tube_length) *
node_length;

h_cold_b_in =
refpropm('H','T',TEMP_cold_in(i),'P',P_cold_in,outer_tube_fluid);
h_cold_b(i) =  enthalpy_rise_increment_c + h_cold_b_in;

TEMP_cold_b(i) =
refpropm('T','H',h_cold_b(i),'P',P_cold_in,outer_tube_fluid);

while (check == true)

    x = x + node_length;
    if x > tube_length
        h_cold_b_out = enthalpy_rise_increment_c + h_cold_b(i);
        TEMP_cold_out =
refpropm('T','H',h_cold_b_out,'P',P_cold_in,outer_tube_fluid);
        break;
    end

    i = i + 1;
    h_cold_b(i) = enthalpy_rise_increment_c + h_cold_b(i-1);
    TEMP_cold_b(i) =
refpropm('T','H',h_cold_b(i),'P',P_cold_in,outer_tube_fluid);

end

%%%%%%%%%%%%%%%%%%%%%%%%%%%%%%%%%%%%%%%%%%%%%%%%%%%%%%%%%%%%%%%%%%%%%%%%%%%%%%%
%
%%%%%%%%%%%%%%%%%%%%%%%%%%%%%%%%%%%%%%%%%%%%%%%%%%%%%%%%%%%%%%%%%%%%%%%%%%%%%%%
%
%                   DETERMINING THE HEAT TRANSFER PROFILES
%
%%%%%%%%%%%%%%%%%%%%%%%%%%%%%%%%%%%%%%%%%%%%%%%%%%%%%%%%%%%%%%%%%%%%%%%%%%%%%%%
%
%%%%%%%%%%%%%%%%%%%%%%%%%%%%%%%%%%%%%%%%%%%%%%%%%%%%%%%%%%%%%%%%%%%%%%%%%%%%%%%
%
```

```
zapper_zoidberg = size(TEMP_hot_b);
m = zapper_zoidberg(1,2);

temp_wall = TEMP_hot_b - 5;

position = zeros;

density_hot_b = zeros;
density_hot_w = zeros;

viscosity_hot_b = zeros;
viscosity_hot_w = zeros;

enthalpy_hot_b = zeros;
enthalpy_hot_w = zeros;

thermal_cond_hot_b = zeros;
thermal_cond_hot_w = zeros;

specific_heat_hot_b = zeros;
specific_heat_hot_w = zeros;

avg_specific_heat_hot = zeros;

re_number_hot = zeros;
re_number_hot_w = zeros;

prandtl_num_hot = zeros;
prandtl_num_hot_w = zeros;

nu_number_mokry_hot = zeros;
nu_number_swenson_hot = zeros;
nu_number_bishop_hot = zeros;
nu_number_dittus_hot = zeros;

htc_hot_mokry = zeros;
htc_hot_swenson = zeros;
htc_hot_bishop = zeros;
htc_hot_dittus = zeros;

thermal_cond_tube = zeros;

heat_flux_hot = zeros;

density_cold_b = zeros;
density_cold_w = zeros;

viscosity_cold_b = zeros;
viscosity_cold_w = zeros;

enthalpy_cold_b = zeros;
enthalpy_cold_w = zeros;
```

```
thermal_cond_cold_b = zeros;
thermal_cond_cold_w = zeros;

specific_heat_cold_b = zeros;
specific_heat_cold_w = zeros;

avg_specific_heat_cold = zeros;

re_number_cold = zeros;
re_number_cold_w = zeros;

prandtl_num_cold = zeros;
prandtl_num_cold_w = zeros;

nu_number_mokry_cold = zeros;
nu_number_swenson_cold = zeros;
nu_number_bishop_cold = zeros;
nu_number_dittus_cold = zeros;

htc_cold_mokry = zeros;
htc_cold_swenson = zeros;
htc_cold_bishop = zeros;
htc_cold_dittus = zeros;

heat_flux_cold = zeros;

thermal_resistance_hot = zeros;
thermal_resistance_cold = zeros;
thermal_resistance_tube = zeros;
R = zeros;
U_trend = zeros;
t_wall = zeros;


for j = 2:m

    position(j) = node_length * j - node_length;

end


for j = 1:m

    delta_temp = 1;

    while abs(delta_temp) > 0.3

    % Fluid properties - Bulk (Hot Side)
    density_hot_b(j) =
refpropm('D','T',TEMP_hot_b(j),'P',P_hot_in,inner_tube_fluid);
    viscosity_hot_b(j) =
refpropm('V','T',TEMP_hot_b(j),'P',P_hot_in,inner_tube_fluid);
```

```
    enthalpy_hot_b(j) =
refpropm('H','T',TEMP_hot_b(j),'P',P_hot_in,inner_tube_fluid);
    thermal_cond_hot_b(j) =
refpropm('L','T',TEMP_hot_b(j),'P',P_hot_in,inner_tube_fluid);
    specific_heat_hot_b(j) =
refpropm('C','T',TEMP_hot_b(j),'P',P_hot_in,inner_tube_fluid);

    % Fluid properties - Wall (Hot Side)
    density_hot_w(j) =
refpropm('D','T',temp_wall(j),'P',P_hot_in,inner_tube_fluid);
    viscosity_hot_w(j) =
refpropm('V','T',temp_wall(j),'P',P_hot_in,inner_tube_fluid);
    enthalpy_hot_w(j) =
refpropm('H','T',temp_wall(j),'P',P_hot_in,inner_tube_fluid);
    thermal_cond_hot_w(j) =
refpropm('L','T',temp_wall(j),'P',P_hot_in,inner_tube_fluid);
    specific_heat_hot_w(j) =
refpropm('C','T',temp_wall(j),'P',P_hot_in,inner_tube_fluid);

    % Calculations to Determine Heat Transfer Coefficient (Hot Side)
    avg_specific_heat_hot(j) = (enthalpy_hot_w(j) - enthalpy_hot_b(j)) /
(temp_wall(j) - TEMP_hot_b(j));

    re_number_hot(j) = (d_i * mass_flux_tube_h) / viscosity_hot_b(j);
    re_number_hot_w(j) = (d_i * mass_flux_tube_h) / viscosity_hot_w(j);

    prandtl_num_hot(j) = (viscosity_hot_b(j) * avg_specific_heat_hot(j)) /
(thermal_cond_hot_b(j));
    prandtl_num_hot_w(j) = (viscosity_hot_w(j) * avg_specific_heat_hot(j))
/ (thermal_cond_hot_w(j));

    nu_number_mokry_hot(j) = 0.0061 * (re_number_hot(j)^0.904) *
(prandtl_num_hot(j)^0.684) * ((density_hot_w(j) /
density_hot_b(j))^0.564);
    nu_number_swenson_hot(j) = 0.00459 * (re_number_hot_w(j)^0.923) *
(prandtl_num_hot_w(j)^0.613) * ((density_hot_w(j) /
density_hot_b(j))^0.231);
    nu_number_bishop_hot(j) = 0.0069 * (re_number_hot(j)^0.9) *
(prandtl_num_hot(j)^0.66) * ((density_hot_w(j) / density_hot_b(j))^0.43);
    nu_number_dittus_hot(j) = 0.023 * (re_number_hot(j)^0.8) *
(prandtl_num_hot(j)^0.4);

    htc_hot_mokry(j) = (nu_number_mokry_hot(j) * thermal_cond_hot_b(j)) /
d_i;
    htc_hot_swenson(j) = (nu_number_swenson_hot(j) *
thermal_cond_hot_w(j)) / d_i;
    htc_hot_bishop(j) = (nu_number_bishop_hot(j) * thermal_cond_hot_b(j))
/ d_i;
    htc_hot_dittus(j) = (nu_number_dittus_hot(j) * thermal_cond_hot_b(j))
/ d_i;

    thermal_cond_tube(j) = 0.00000002 * (temp_wall(j))^3 - 0.00004 *
(temp_wall(j))^2 + 0.0398 * (temp_wall(j)) + 5.728;
```

```
    heat_flux_hot(j) = (htc_hot_mokry(j) * (temp_wall(j) -
TEMP_hot_b(j)));

    % Fluid properties - Bulk (Cold Side)
    density_cold_b(j) =
refpropm('D','T',TEMP_cold_b(j),'P',P_cold_in,outer_tube_fluid);
    viscosity_cold_b(j) =
refpropm('V','T',TEMP_cold_b(j),'P',P_cold_in,outer_tube_fluid);
    enthalpy_cold_b(j) =
refpropm('H','T',TEMP_cold_b(j),'P',P_cold_in,outer_tube_fluid);
    thermal_cond_cold_b(j) =
refpropm('L','T',TEMP_cold_b(j),'P',P_cold_in,outer_tube_fluid);
    specific_heat_cold_b(j) =
refpropm('C','T',TEMP_cold_b(j),'P',P_cold_in,outer_tube_fluid);

    % Fluid properties - Wall (Cold Side)
    density_cold_w(j) =
refpropm('D','T',temp_wall(j),'P',P_cold_in,outer_tube_fluid);
    viscosity_cold_w(j) =
refpropm('V','T',temp_wall(j),'P',P_cold_in,outer_tube_fluid);
    enthalpy_cold_w(j) =
refpropm('H','T',temp_wall(j),'P',P_cold_in,outer_tube_fluid);
    thermal_cond_cold_w(j) =
refpropm('L','T',temp_wall(j),'P',P_cold_in,outer_tube_fluid);
    specific_heat_cold_w(j) =
refpropm('C','T',temp_wall(j),'P',P_cold_in,outer_tube_fluid);

    % Calculations to Determine Heat Transfer Coefficient (Cold Side)
    avg_specific_heat_cold(j) = (enthalpy_cold_w(j) - enthalpy_cold_b(j))
/ (temp_wall(j) - TEMP_cold_b(j));

    re_number_cold(j) = (D_h * mass_flux_tube_c) / viscosity_cold_b(j);
    re_number_cold_w(j) = (D_h * mass_flux_tube_c) / viscosity_cold_w(j);

    prandtl_num_cold(j) = (viscosity_cold_b(j) *
avg_specific_heat_cold(j)) / (thermal_cond_cold_b(j));
    prandtl_num_cold_w(j) = (viscosity_cold_w(j) *
avg_specific_heat_cold(j)) / (thermal_cond_cold_w(j));

    nu_number_mokry_cold(j) = 0.0061 * (re_number_cold(j)^0.904) *
(prandtl_num_cold(j)^0.684) * ((density_cold_w(j) /
density_cold_b(j))^0.564);
    nu_number_swenson_cold(j) = 0.00459 * (re_number_cold_w(j)^0.923) *
(prandtl_num_cold_w(j)^0.613) * ((density_cold_w(j) /
density_cold_b(j))^0.231);
    nu_number_bishop_cold(j) = 0.0069 * (re_number_cold(j)^0.9) *
(prandtl_num_cold(j)^0.66) * ((density_cold_w(j) /
density_cold_b(j))^0.43);
    nu_number_dittus_cold(j) = 0.023 * (re_number_cold(j)^0.8) *
(prandtl_num_cold(j)^0.4);

    htc_cold_mokry(j) = (nu_number_mokry_cold(j) * thermal_cond_cold_b(j))
/ D_h;
    htc_cold_swenson(j) = (nu_number_swenson_cold(j) *
thermal_cond_cold_w(j)) / D_h;
```

```
    htc_cold_bishop(j) = (nu_number_bishop_cold(j) *
thermal_cond_cold_b(j)) / D_h;
    htc_cold_dittus(j) = (nu_number_dittus_cold(j) *
thermal_cond_cold_b(j)) / D_h;

    heat_flux_cold(j) = htc_cold_mokry(j) * (temp_wall(j) -
TEMP_cold_b(j));

    % Thermal Resistance Calculations
    thermal_resistance_hot(j) = (1/htc_hot_mokry(j));
    thermal_resistance_cold(j) = (d_i / (d_o * htc_cold_mokry(j)));
    thermal_resistance_tube(j) = (d_i * log(d_o / d_i)) / (2 *
thermal_cond_tube(j));

    % Calculating the Overall Heat Transfer Coefficient (U)
    R(j) = (thermal_resistance_hot(j) + thermal_resistance_tube(j) +
thermal_resistance_cold(j));
    U_trend(j) = (1 / R(j));

    % Calculating the Wall Temperature of the tube
    t_wall(j) = (((TEMP_hot_b(j) / thermal_resistance_hot(j)) +
(TEMP_cold_b(j) / thermal_resistance_cold(j))) / ((1 /
thermal_resistance_hot(j)) + (1 / thermal_resistance_cold(j))));

    delta_temp = t_wall(j) - temp_wall(j);

    if delta_temp > 0.3
        temp_wall(j) = temp_wall(j) + abs(delta_temp)/2;
    end

    if delta_temp < -0.3
        temp_wall(j) = temp_wall(j) - abs(delta_temp)/2;
    end

    end
end

z_h_mass_flow_per_tube = mass_flow_rate_tube_h;
z_h_total_mass_flow = z_h_mass_flow_per_tube * No_tubes;

z_c_mass_flow_per_tube = mass_flow_rate_tube_c;
z_c_total_mass_flow = z_c_mass_flow_per_tube * No_tubes;

z_surface_area_per_tube = tube_surface_area;
z_total_heat_transfer_surface_area = z_surface_area_per_tube * No_tubes;

%%%%%%%%%%%%%%%%%%%%%%%%%%%%%%%%%%%%%%%%%%%%%%%%%%%%%%%%%%%%%%%%%%%%%%%%%%%%
%
%%%%%%%%%%%%%%%%%%%%%%%%%%%%%%%%%%%%%%%%%%%%%%%%%%%%%%%%%%%%%%%%%%%%%%%%%%%%
%
%               MATRIX TRANSPOSE OF HEAT TRANSFER PROFILES
%
%%%%%%%%%%%%%%%%%%%%%%%%%%%%%%%%%%%%%%%%%%%%%%%%%%%%%%%%%%%%%%%%%%%%%%%%%%%%
%
```

```
%%%%%%%%%%%%%%%%%%%%%%%%%%%%%%%%%%%%%%%%%%%%%%%%%%%%%%%%%%%%%%%%%%%%%%%%%%%%%%%%
%

position = position';  % m

% Hot Side
TEMP_hot_b = TEMP_hot_b' - 273.15;  % degC
temp_wall = temp_wall' - 273.15;  % degC

density_hot_b = density_hot_b';  % kg/m^3
density_hot_w = density_hot_w';  % kg/m^3

viscosity_hot_b = viscosity_hot_b' * 1000000;  % uPa*s
viscosity_hot_w = viscosity_hot_w' * 1000000;  % uPa*s

enthalpy_hot_b = enthalpy_hot_b' / 1000;  % kJ/kg
enthalpy_hot_w = enthalpy_hot_w' / 1000;  % kJ/kg

thermal_cond_hot_b = thermal_cond_hot_b';  % W/(m*degC)
thermal_cond_hot_w = thermal_cond_hot_w';  % W/(m*degC)

specific_heat_hot_b = specific_heat_hot_b' / 1000;  % kJ/kg
specific_heat_hot_w = specific_heat_hot_w' / 1000;  % kJ/kg

avg_specific_heat_hot = avg_specific_heat_hot' / 1000;  % kJ/kg

re_number_hot = re_number_hot';
re_number_hot_w = re_number_hot_w';

prandtl_num_hot = prandtl_num_hot';
prandtl_num_hot_w = prandtl_num_hot_w';

nu_number_mokry_hot = nu_number_mokry_hot';
nu_number_swenson_hot = nu_number_swenson_hot';
nu_number_bishop_hot = nu_number_bishop_hot';
nu_number_dittus_hot = nu_number_dittus_hot';

htc_hot_mokry = htc_hot_mokry' / 1000;  % kW/(m^2*degC)
htc_hot_swenson = htc_hot_swenson' / 1000;  % kW/(m^2*degC)
htc_hot_bishop = htc_hot_bishop' / 1000;  % kW/(m^2*degC)
htc_hot_dittus = htc_hot_dittus' / 1000;  % kW/(m^2*degC)

thermal_cond_tube = thermal_cond_tube';  % % W/(m*degC)

heat_flux_hot = heat_flux_hot' / 1000;  % kW/m^2

% Cold Side
TEMP_cold_b = TEMP_cold_b' - 273.15;  % degC
t_wall = t_wall' - 273.15;  % degC

density_cold_b = density_cold_b';  % kg/m^3
density_cold_w = density_cold_w';  % kg/m^3
```

```
viscosity_cold_b = viscosity_cold_b' * 1000000;  % uPa*s
viscosity_cold_w = viscosity_cold_w' * 1000000;  % uPa*s

enthalpy_cold_b = enthalpy_cold_b' / 1000;  % kJ/kg
enthalpy_cold_w = enthalpy_cold_w' / 1000;  % kJ/kg

thermal_cond_cold_b = thermal_cond_cold_b';  % W/(m*degC)
thermal_cond_cold_w = thermal_cond_cold_w';  % W/(m*degC)

specific_heat_cold_b = specific_heat_cold_b' / 1000;  % kJ/kg
specific_heat_cold_w = specific_heat_cold_w' / 1000;  % kJ/kg

avg_specific_heat_cold = avg_specific_heat_cold' / 1000;  % kJ/kg

re_number_cold = re_number_cold';
re_number_cold_w = re_number_cold_w';

prandtl_num_cold = prandtl_num_cold';
prandtl_num_cold_w = prandtl_num_cold_w';

nu_number_mokry_cold = nu_number_mokry_cold';
nu_number_swenson_cold = nu_number_swenson_cold';
nu_number_bishop_cold = nu_number_bishop_cold';
nu_number_dittus_cold = nu_number_dittus_cold';

htc_cold_mokry = htc_cold_mokry' / 1000;  % kW/(m^2*degC)
htc_cold_swenson = htc_cold_swenson' / 1000;  % kW/(m^2*degC)
htc_cold_bishop = htc_cold_bishop' / 1000;  % kW/(m^2*degC)
htc_cold_dittus = htc_cold_dittus' / 1000;  % kW/(m^2*degC)

heat_flux_cold = heat_flux_cold' / 1000;  % kW/m^2

% Thermal Resistances and Overall HTC
thermal_resistance_hot = thermal_resistance_hot';
thermal_resistance_cold = thermal_resistance_cold';
thermal_resistance_tube = thermal_resistance_tube';

U_trend = U_trend' / 1000;


z_avg_k_hot = mean(thermal_cond_hot_b);
z_avg_k_cold = mean(thermal_cond_cold_b);

z_avg_cp_hot = mean(specific_heat_hot_b);
z_avg_cp_cold = mean(specific_heat_cold_b);

toc
```

Appendix B: Thermophysical Properties of Selected Test Cases

This appendix contains the profiles of selected thermophysical properties of the reference cases for HX-1 and HX-2. In addition, the profiles from Sections 4.1.3 and 4.2.3 are also presented. Fluid pressure has an impact on the severity with which thermophysical properties vary in the pseudocritical region. For this this reason, these profiles were selected as these are the test cases in which a sensitivity analysis on pressure was conducted.

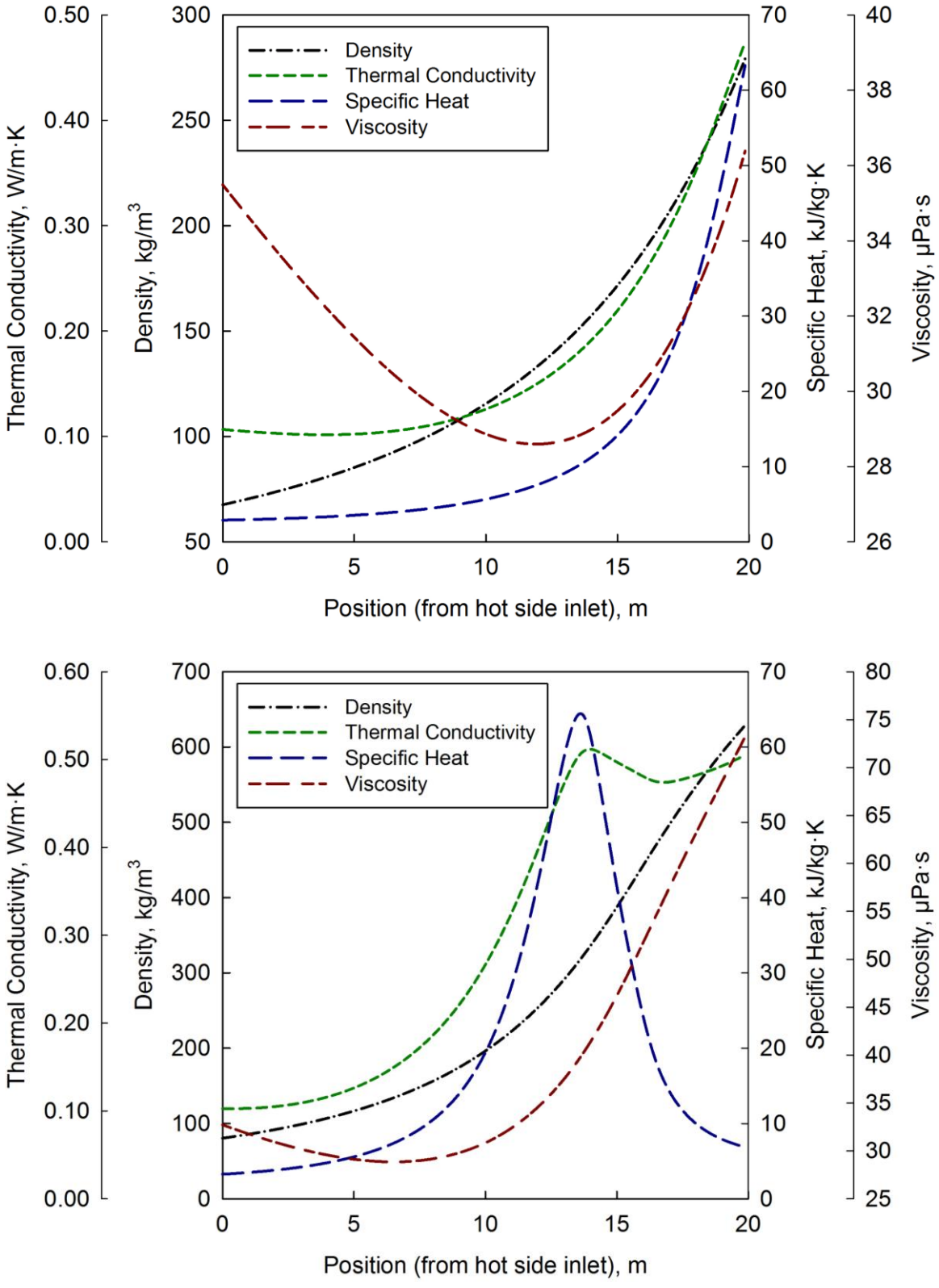

Figure B-1. Thermophysical properties for HX-1 reference case. Upper diagram = hot side, lower diagram = cold side.

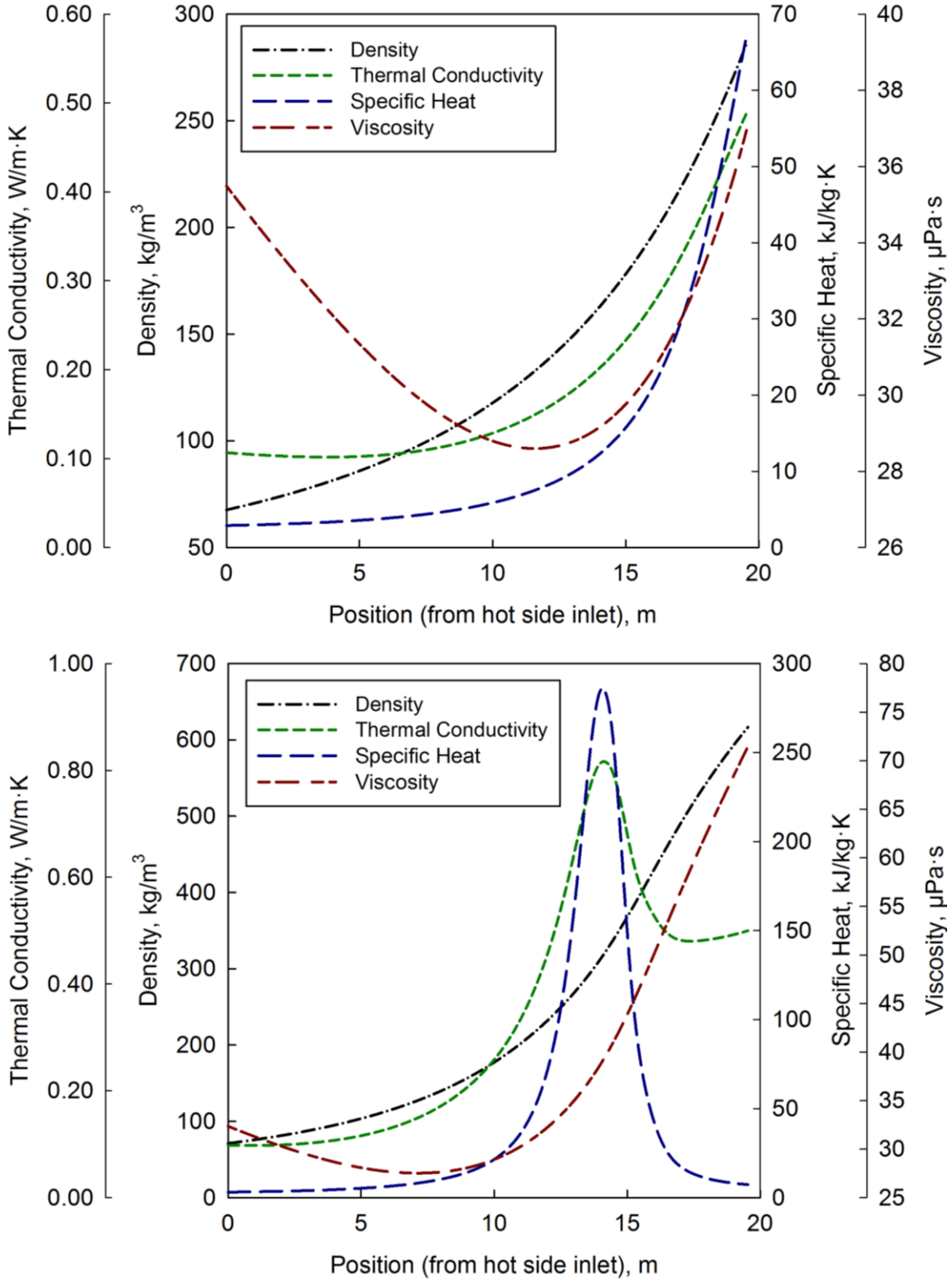

Figure B-2. Thermophysical properties for HX-1 test case #6. Upper diagram = hot side, lower diagram = cold side.

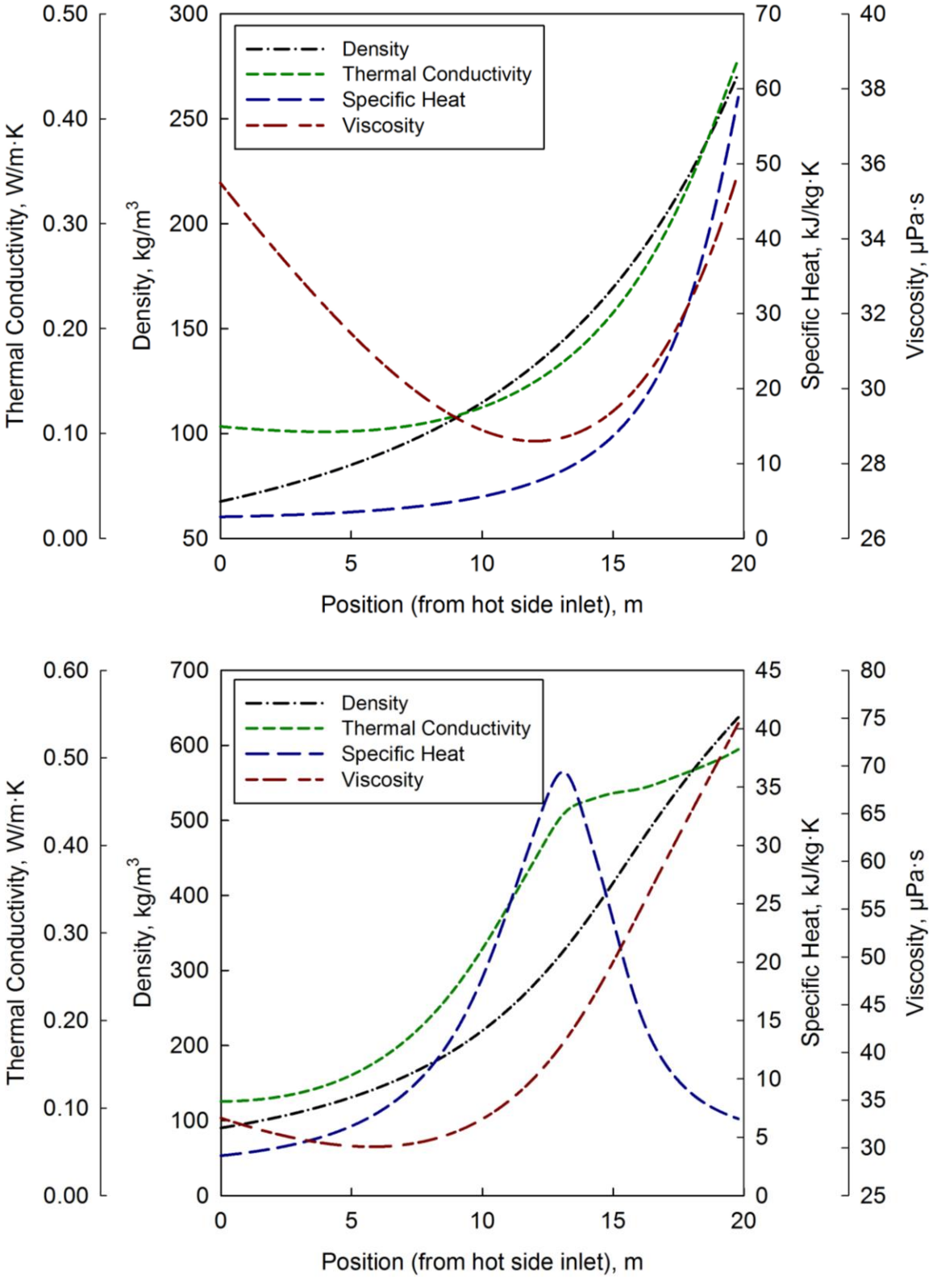

Figure B-3. Thermophysical properties for HX-1 test case #7. Upper diagram = hot side, lower diagram = cold side.

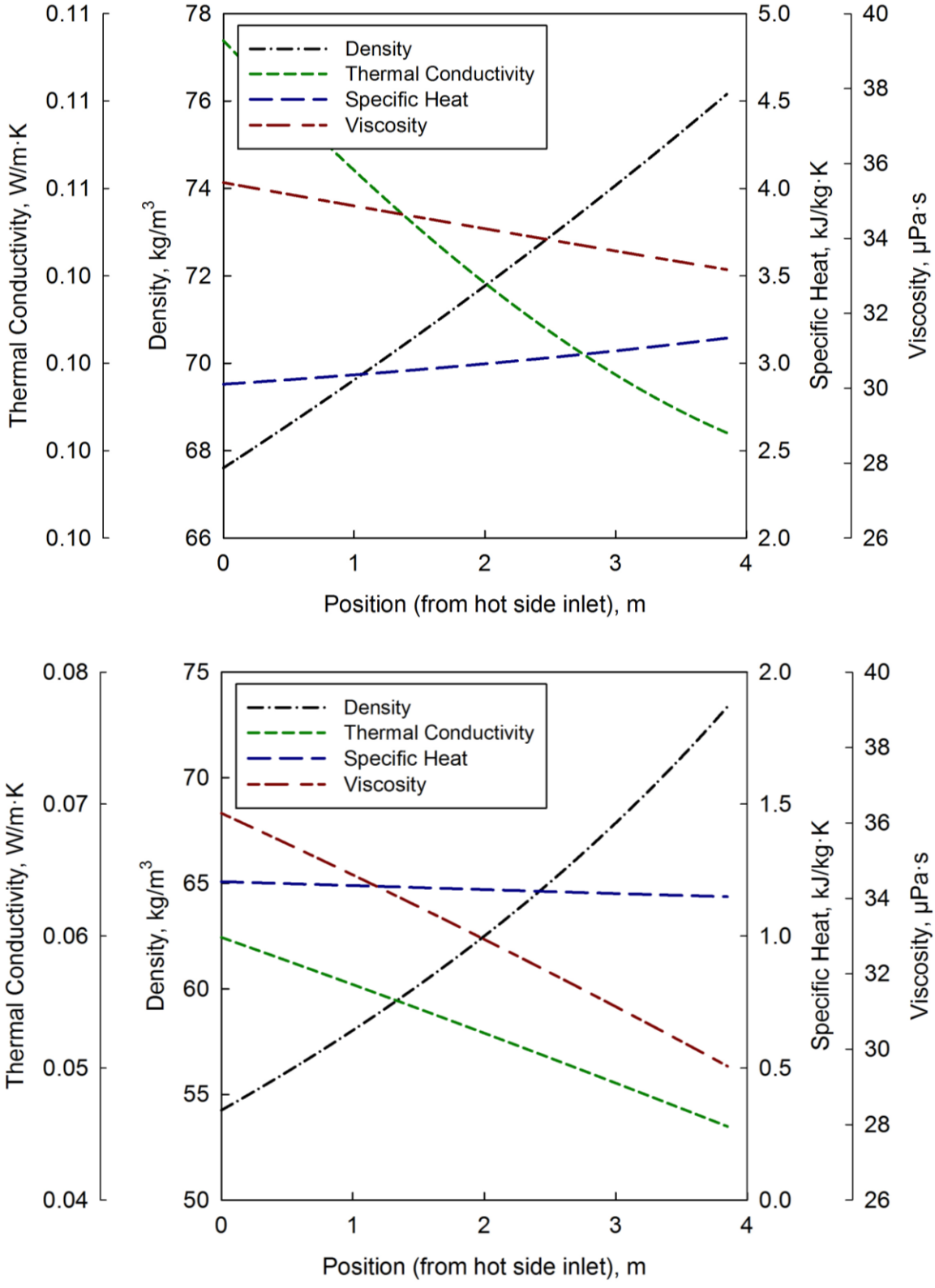

Figure B-4. Thermophysical properties for HX-2 reference case. Upper diagram = hot side, lower diagram = cold side.

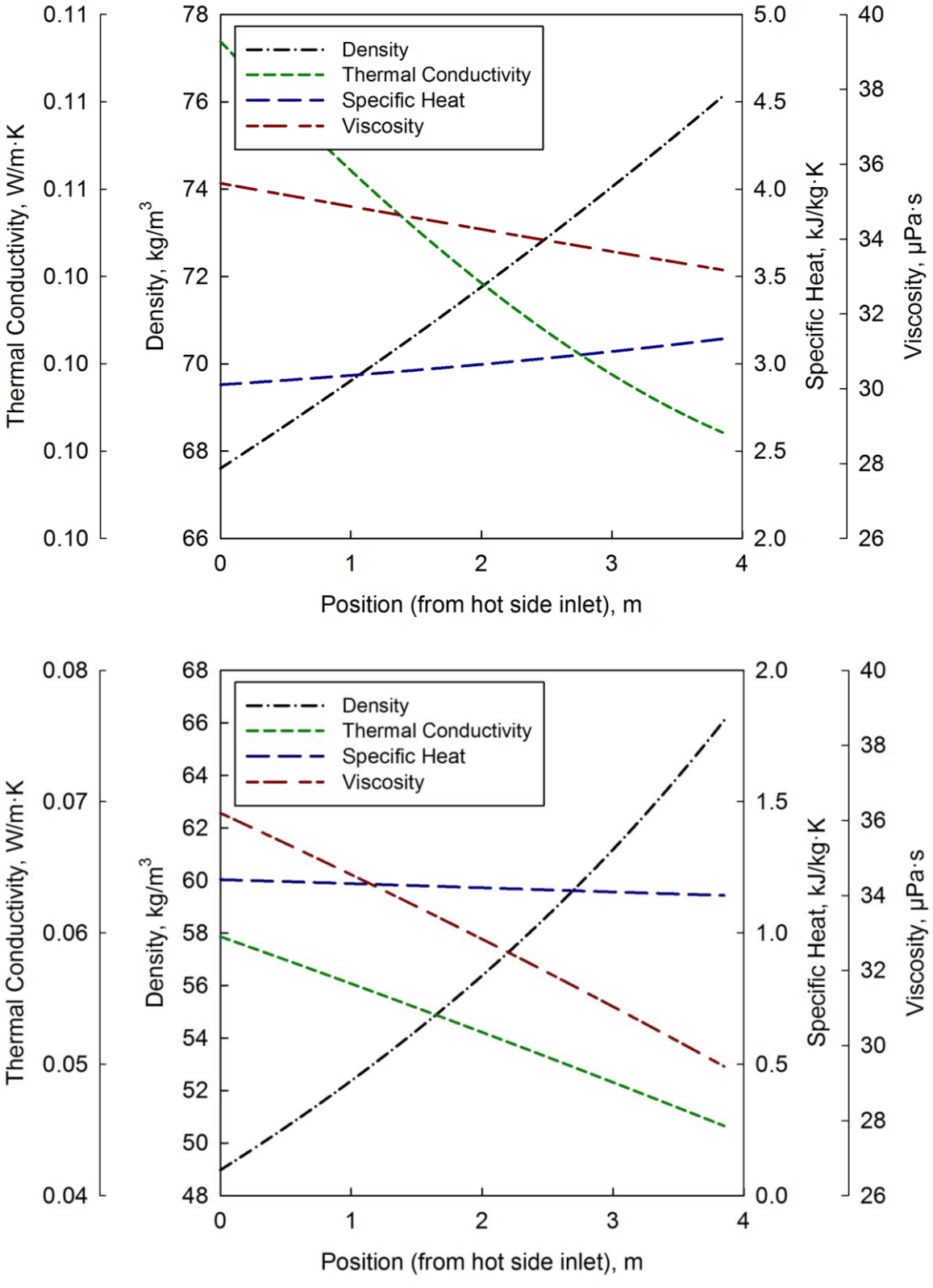

Figure B-5. Thermophysical properties for HX-2 test case #16. Upper diagram = hot side, lower diagram = cold side.

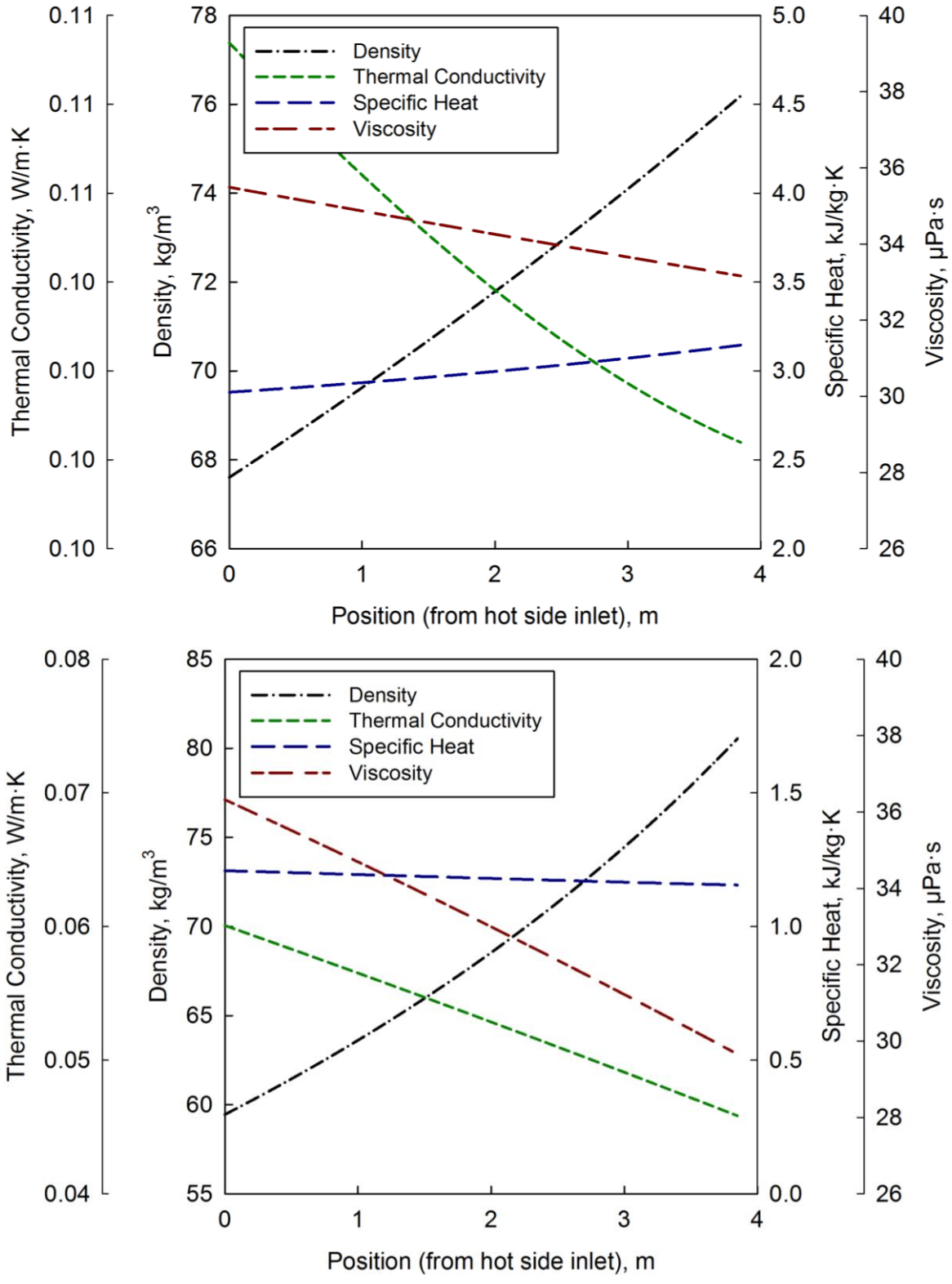

Figure B-6. Thermophysical properties for HX-2 test case #17. Upper diagram = hot side, lower diagram = cold side.

Appendix C: Comparison of Supercritical Water HTC Profiles

In Section 2.4.1, several correlations used to calculate the Nu number for SCW were presented. A comparison of the HTC values obtained using these correlations is shown in Figure C-1. This figure is developed using the reference case for HX-1 from Section 4.1.1. It is evident that each of these correlations follow a similar trend with major difference between the results is in pseudocritical region, where the magnitude of the peaks in HTC are different for each correlation. The only correlation to directly stand out is the Dittus-Boelter correlation. This correlation does not use the average Prandtl number and therefore does not account for wall temperatures. This is evidenced by the shift in the location of the peak when compared to the profiles of the other correlations. As the Bishop et al., Mokry et al. and Swenson et al. correlations are calculated using average Prandtl number, the location of the peak in HTC along the length of the HX is at the position as the peak in average specific heat. For this reason, the peaks for all of these correlations are in a similar position.

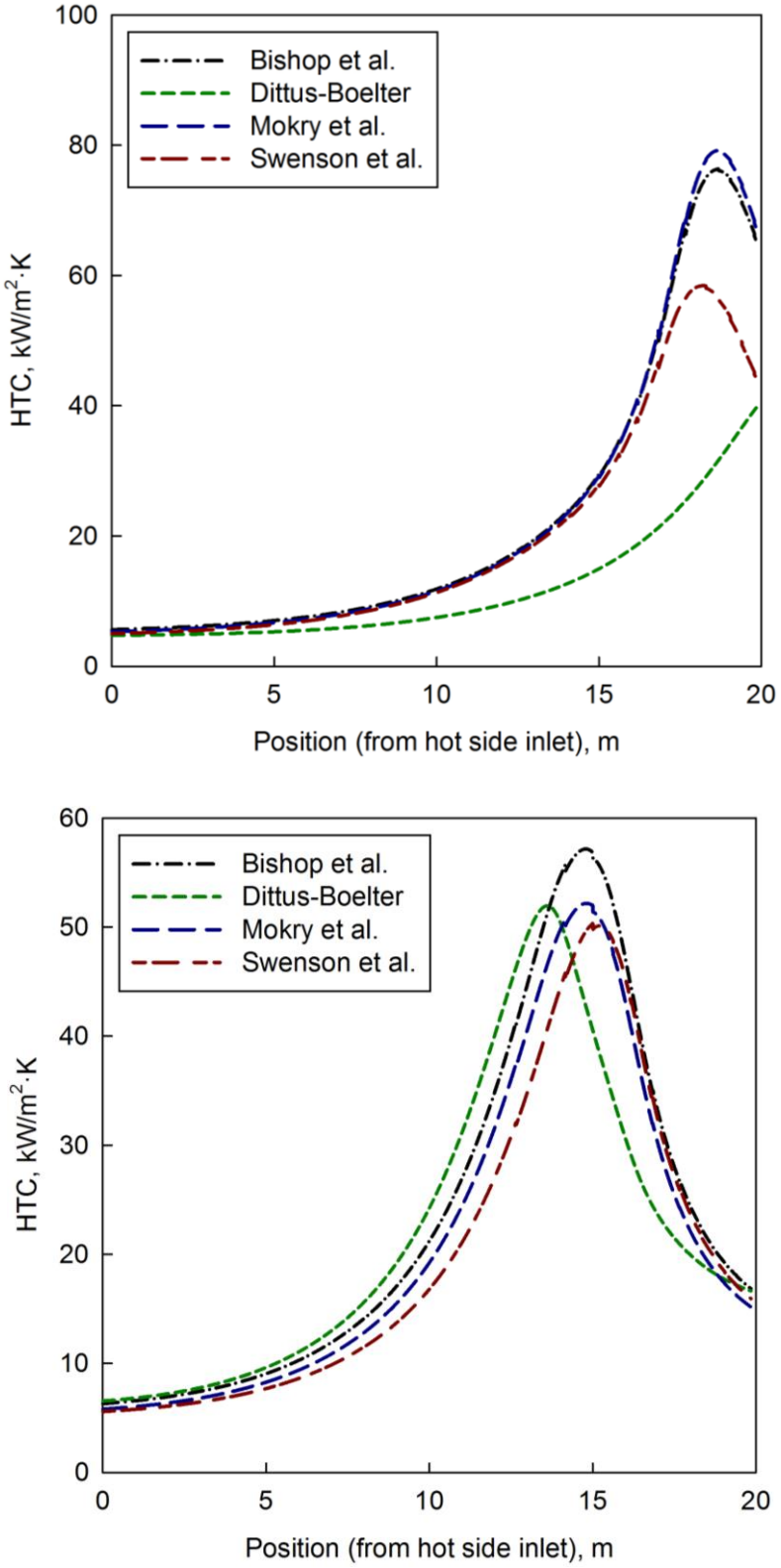

Figure C-1. Comparison of HTC obtained from various correlations. Upper diagram = hot side, lower diagram = cold side.

Appendix D: List of Publications, Conferences Attended and Awards

Publications in International Conference Proceedings

1. Jouvin, J.C., Samuel J., and Pioro, I., 2014. Analysis of thermophysical properties for selected supercritical fluids, Proceedings of the 22nd International Conference on Nuclear Engineering (ICONE-22), Prague, Czech Republic, July 7-11, Paper No. 30146. 10 pages.
2. Jouvin, J.C. and Pioro, I., 2014. Investigation of R-134a as a modeling fluid for supercritical water, Proceedings of the 38th Annual Student Conference of the Canadian Nuclear Society and Canadian Nuclear Association at the 19th Annual Pacific Basin Nuclear Conference (PBNC-2014), Vancouver, Canada, August 24-28, Paper No. 18. 5 pages.
3. Jouvin, J.C. and Pioro, I., 2015. Supercritical working fluids for hydrogen production via intermediate heat exchanger, Proceedings of the 6th International Conference on Hydrogen Production (ICH2P-2015), Oshawa, Canada, May 3-6, 2015. 12 pages.
4. Jouvin, J.C. and Pioro, I., 2015. Heat transfer analysis of an intermediate heat exchanger for an SCWR hydrogen cogeneration plant, Proceedings of the 23rd International Conference on Nuclear Engineering (ICONE-23), Chiba, Japan, May 17-21, Paper No. 1747. 9 pages.
5. Jouvin, J.C. and Pioro, I., 2015. Heat transfer analysis for the application of SCWR process heat for the thermochemical production of hydrogen, Proceedings of the 39th Annual Student Conference of the Canadian Nuclear Society and Canadian Nuclear Association (CNS/CNA-2015), Saint John, Canada, May 31 - June 3, Paper No. 13. 5 pages.

Conferences Attended with Presentations

1. 22nd International Conference on Nuclear Engineering (ICONE-22). July 7-11, 2014. Prague, Czech Republic.
2. 38th Annual Student Conference of the Canadian Nuclear Society and Canadian Nuclear Association at the 19th Annual Pacific Basin Nuclear Conference (PBNC-2014). August 24-28, 2014. Vancouver, Canada.
3. 6th International Conference on Hydrogen Production (ICH2P-2015). May 3-6, 2015. Oshawa, Canada.
4. 23rd International Conference on Nuclear Engineering (ICONE-23). May 17-21, 2015. Chiba, Japan.
5. 39th Annual Student Conference of the Canadian Nuclear Society and Canadian Nuclear Association (CNS/CNA-2015). May 31 - June 3, 2015. Saint John, Canada.

Awards and Honours

1. ICONE 22 Student Best Poster Competition – North America
2. ICONE 23 Student Best Poster Competition – North America
3. ICONE 23 Certificate of Appreciation